3D Reconstruction of 138 KV Power-lines from Airborne LiDAR Data

by

Qing Xiang

A thesis

presented to the University of Waterloo

in fulfillment of the

thesis requirement for the degree of

Master of Science

in

Geography

Waterloo, Ontario, Canada, 2014

Author's Declaration

I hereby declare that I am the sole author of this thesis. This is a true copy of the thesis, including any required final revisions, as accepted by my examiners.

I understand that my thesis may be made electronically available to the public.

Abstract

Due to infrequent and imprecise maintenance inspection in power-line corridors, accidents can be caused by interferences, for instance, surrounding trees. Transmission power-line inspection conventionally relies on the participation of ground personnel and airborne camera to patrol power-lines, and is limited by intensive labour, and difficult working conditions and management. Airborne light detection and ranging (LiDAR) has proven a powerful tool to overcome these limitations to enable more efficient inspection. Active airborne LiDAR systems directly capture the 3D information of power infrastructure and surrounding objects. This study aims at building a semi-automatic 3D reconstruction workflow for power-lines extracted from airborne LiDAR data of 138 kV transmission line corridors (500 m by 340 m) in Nanaimo, BC, Canada.

The proposed workflow consists of three components: detection, extraction, and fitting. The power-lines are automatically detected with regular geometric shape using a set of algorithms, including density-based filtering, Hough transform and concatenating algorithm. The complete power-lines are then extracted using a rectangular searching technique. Finally, the 3D power-lines are reconstructed through fitting by a hyperbolic cosine function and least-squares fitting. A case study is carried out to evaluate the proposed workflow for hazard tree detection in the corridor.

The results obtained demonstrate that power-lines can be reconstructed in 3D, which are useful in detection of hazard trees to support power-line corridor management.

Acknowledgements

During my study at the University of Waterloo, and living in Canada these two and a half years, I have been helped and inspired by a lot of people.

I would like to express my gratitude to my supervisor, Prof. Dr. Jonathan Li, from whom I have learnt not only the professional knowledge on remote sensing, but also guidance on career. Thank my committee members, Dr. Su-Yin Tan, Prof. Dr. Richard Kelly and Dr. Joe Qian, to review my thesis and provide me their constructive comments. Thank Dr. Yongjun Zhou, a visiting scholar here, for his kind help and consultant on the problems about modeling.

I would like to thank the City of Nanaimo (website) for providing the airborne LiDAR data and orthophoto in this study. Thank Mark Willoughby, Senior GIS Specialist at the City of Nanaimo, for providing the LiDAR metadata; and Andrea Caza, Reference Officer at the National Energy Board Library, for answering my consultant kindly.

Thank all my friends and colleagues: Mike Lackner, for sharing the experience on ArcGIS software; Haiyan Guan, for giving suggestions on thesis wiring; Paula Aguayo and Roberto Tapia, for our IDL group studying together; Anqi Fu, for helping me a lot in life; Mrs. Fran PS, and Mr. Andrew Fung, for the proof reading of my thesis; and all other friends in China and here.

There is no possible way to express adequately my gratitude to my family: my dear parents, without whom I will not gain the coverage to keep going on these years. Special thanks to my dear boyfriend, Ke Yang, who was in China but accompanied me and helped me sincerely during my stay in Canada.

献给我亲爱的家人

Table of Contents

Glossary of Terms and Abbreviations

2D: Two-dimensional.

2.5D: 2D representation of 3D data. It refers to a raster representation of the airborne LiDAR data.

3D: Three-dimensional.

ALS: Airborne laser scanning.

Conductor: Wire strung between poles or towers, used for transmitting electricity.

Crown Land: Property owned or under the jurisdiction of the Provincial or Federal Government.

Echo: The number of received pulses from one emits pulse.

FOV:Field of view.

GIS: Geographic information system.

GNSS: Global navigation satellite system.

GPS: Global positioning system.

IMU: Inertial measurement unit.

LiDAR: Light detection and ranging.

Hazard Tree: A tree which is defective or over-grown, has a “target” (where it is likely to hit or damage a person or object when it fails), and has the imminent potential to fail.

Laser footprint: It is related to range and beam divergence.

MLS: Mobile laser scanning.

Outliers: Usually refer to the values lie outside the other values. In this study, the outliers mainly refer to the points in the point cloud do not represent any objects; it should not be in the point cloud.

Pylon: Transmission tower, used to support an overhead power-line.

Raster image: An image that made up of grid of pixels; commonly is referring to as a bitmap.

RMSE: Root mean square error.

ROW: Right-of-Way, a term to describe limited interests in land which provide the right to utilize the property, for specific purposes, without having full ownership. Limited interests are defined by statutory rights-of-way, lease, licence, permit or letter agreements.

Scan rate: Number of scan/second.

Span: A section between two pylons.

TIN: Triangular irregular network.

TLS: Terrestrial laser scanning.

List of Figures

List of Tables

Chapter 1 Introduction

1.1 Motivation

The rapidly developing global power grid urgently requires security maintenance of electricity grids and other infrastructure facilities. In order to alleviate the increasingly prominent disparity between supply and demand of electricity, especially during blackouts, and adapt to the rapid development of the national economy, almost all the countries in the world are accelerating the development of their power-line networks.

As the 2nd largest exporter and the 5th largest producer of electricity in the world, Canada has a bulk transmission network of over 160,000 km of high voltage power-lines (Industry Canada, 2008). Key corridor objects like power-lines, towers, as well as terrain, buildings and trees require precise, effective frequent inspection, a fact made clearer by the blackout in August 14, 2003 that affected parts of the Northeastern and Midwestern United States and Ontario, Canada. This was the largest power outage in that region in decades (Federal Energy Regulatory Commission, 2004). The 2003 blackout affected 10 million people in Ontario, Canada and 45 million people in eight U.S. states. According to the blackout investigation, during the hour before the cascading blackout occurred, three First Energy 345kV transmission lines failed because a power company did not prune trees in the summer peak season (U.S.-Canada Power System Outage Task Force, 2004). As a result of contact between the lines and overgrown vegetation that encroached into the required clearance zone for the lines, the high voltage power-line sagged, touched the branches and resulted in a short circuit. During the Christmas holiday in 2013, tens of thousands of people in Ontario, Quebec and New Brunswick experienced a large power outage caused by an ice storm (Campbell, 2013). The Environment Canada stated that the

wind led to new power outages as ice and snow-laden limbs could snap onto power-lines (Coorsh, 2013).

The dramatic blackouts in Canada demonstrate that there is a major security problem on the power-line corridors in vegetation growth. The power-line has features like long distance, large coverage, and high security and reliability. It is an important part of the national grid. However, due to infrequent maintenance inspection, sometimes accidents are caused by interferences, such as surrounding trees. The transmission lines contact air directly without the insulation layer. When a tree comes into contact with or close to the wire, there is a risk of flashover discharge, easy to produce sparks. The tree becomes an electrified body, resulting in the power-line single-phase grounding; even short trips can cause power outages and even serious fire. On average, trees are involved in approximately 30 percent of all power outages (Consumers Energy, 2013). In British Columbia, trees cause more than half of all outages in the power-line corridors (BC Hydro, 2013).

In order to prevent and eliminate network security incidents, power operation and maintenance companies have regular power-line inspection work. The risk management of transmission line corridors is necessary and it is a problem on the table. The transmission lines in corridors of remote areas may be especially threatened by high trees. They are required to do regular and timely inspection and removal.

Typically, the primary power-line inspection methods are aerial and ground inspections (Federal Energy Regulatory Commission, 2004). For a long time, Canada's power-line construction, maintenance and overhaul work mainly relied on a combination of aerial and ground inspections. Ground inspections are performed by walking or driving the length of

transmission lines to inspect the corridor features. Aerial inspections are conducted using aircraft, such as a small plane, a helicopter or an unmanned aerial vehicle (UAV), to visually inspect the corridor conditions.

The conventional way of ground inspection is accurate as it enables an inspector to view vegetation conditions and relationships between power-lines and vegetation thoroughly. However, it has limits of being time consuming, intensive labour, difficult working conditions, low labor efficiency, and hard management. In Canada, most of the high voltage transmission line corridors are in remote areas with forests and mountains. It's hard to conduct the inspection by walking and driving, especially in the period with bad weather conditions.

The aerial inspections can obtain different products: aerial colour imagery, infrared imagery and video. Through the acquired aerial photo, the damage condition of power-line facilities can be detected. UAV is currently a new method in power-line inspection. The advantages of the UAV are low weight, high speed data acquisition, flexible flight, and low cost (Yan *et al*., 2007; Li *et al.*, 2008; Li *et al.*, 2010). A fusion of color and infrared images is conducted to generate a virtually enhanced method to detect the power-lines (Yamamoto and Yamada, 1997; Sun *et al.*, 2006). However, based on the low accuracy of spatial orientation, it's hard to determine the spatial relationship between power-lines and corridor features, especially corridors' vegetation. Aerial inspection of overhead power-lines using video taken on an aircraft is also used for the electricity companies to inspect the overhead power-lines routinely (Candamo *et al.*, 2009; Whitworth *et al.*, 2001). One difficulty is the degradation of the image due to rotation of the camera and translational motion of the helicopter. And the weather condition is also a problem when using helicopters and UAVs to get aerial imagery and video.

As the improvement of the remote sensing image processing technology, the application of remote sensing is promoted, and the remote sensing information extraction and analysis of automatic level has increased dramatically. Because the long-range detection on the target is without direct contact, remote sensing earth observation technology must be one of the means to assist or replace the traditional manual transmission line patrol. Using active light detection and ranging (LiDAR) data to assist with the power-line corridor patrol is a state-of-the-art method. Based on the directly achieved elevation information of features within the power-line corridor, power-lines extraction and 3D reconstruction from LiDAR data is an increasingly developed approach to deal with the spatial orientation problems compared with the optical remote sensing imagery. As the traditional ground-based patrol or airborne visual inspection is difficult to reliably estimate the distance between a tree and a power-line, LiDAR technology can be helpful in dealing with low-efficiency and time consuming problems. LiDAR technology can also obtain data even at night or during bad weather conditions, as it is active and does not need the condition of light.

In this context, using the state-of-the-art and efficient active airborne LiDAR data for power-line corridor inspection and facilities to provide safe, reliable, economical inspection and maintenance means of production become the urgent needs of the grid. Better predictions of possible interaction with the 3D environment, such as the extreme wind or ice loads, or increased electricity load, can be obtained, once the after-built positions of power-lines under normal conditions are known (Vosselman *et.al*., 2010).

1.2 Objectives

The main purpose of this study is to build a semi-automatic 3D power-line reconstruction platform using airborne LiDAR data in order to better maintain the power-lines and other corridor features. By modeling the existing power-lines automatically, the vegetation management in the corridor can be useful for the decision-makers to deal with the power-line upgrading and hazard tree treatment. When the power-line models are reconstructed, the hazard trees, which are close by the power-lines, can be detected and removed; the power-line spans can be monitored. As the format of LiDAR data cannot be used directly for the power companies, the product in this study can be provided to them directly. In this study, the power-lines mostly refer to the 138kV transmission lines in a corridor of the City of Nanaimo. The research objectives are listed below:

- To detect the power-lines automatically and accurately;
- To extract the power-lines from airborne LiDAR data;
- To reconstruct 3D power-line models;
- To detect the hazard trees in the power-line corridors.

Through exploring different methodologies, presenting the proposed method of this study, evaluating the accuracy and discussing the feasibility in the later chapters, some suggestions can be proposed for the power companies to use the method in power-line corridor patrol and management.

1.3 Thesis Structure

The thesis is organized by five chapters with this being the first.

Chapter 1 introduces the research background and motivations followed by addressing the research objectives and questions. Finally the organization of the thesis is given.

Chapter 2 reviews literature on different LiDAR data on the power-line inspection, the principles and data structures of LiDAR data, and an overview of the power-line extraction and 3D reconstruction method.

Chapter 3 describes the data and study area in the thesis. The state-of-the-art automatic methodology on power-lines detection and extraction is introduced. The power-line curve fitting and 3D reconstruction methodology is also introduced in this chapter. An idea on hazard tree detection is investigated.

Chapter 4 presents the output of the workflow and discusses the accuracy of the results. The extracted power-line points, the power-line curve fitting results, 3D model of three groups of 138 kV power-lines, and results of hazard tree detection are presented and discussed. A case study result on hazard tree detection is also discussed.

Chapter 5 concludes the experimental results and findings in this study, limitations at this stage, and summarizes the recommendations for further studies.

Chapter 2 Power-line Corridor Mapping: An Overview

This chapter first reviews different kinds of LiDAR technology in power-line inspection. Second, the characteristics of LiDAR data format and structure are introduced. Then the state-of-the-art power-line corridor reconstruction workflow with airborne laser scanning (ALS) data is presented. Finally, background knowledge about power-line corridor management regulations is reviewed to give a reference to the hazard tree detection. This chapter will provide an appropriate theoretical background critical to understanding the whole procedure of power-lines extraction, and the fitting and reconstruction of the corridor. Historical work in related areas such as power-line extraction, reconstruction and hazard tree detection are reviewed.

2.1 Airborne Laser Scanning

2.1.1 Principles

LiDAR is an active remote sensing technology that can measure the distance to, or other properties of a target by illuminating the target with light, often using pulses from a laser (NOAA, 2013). LiDAR is a technique based on an active laser system and a GPS/IMU combination (Vosselman *et al*., 2010).

Laser is an abbreviation of the Light Amplification by Simulated Emission of Radiation. A laser can emit light through a process of optical amplification (Gould, 1959). Natural light is emitted in random directions in variable wavelengths and variable amplitudes with no phase correspondence. Laser light is emitted in single direction in constant wavelengths and constant amplitudes with total phase correspondence (Heritage and Large, 2009). As shown in Figure 2.1, a laser system measures the distance to a target on the ground illuminated by the laser. A GPS/IMU measures the exact position and orientation of the system. GPS is an abbreviation for

Global Positioning System which provides the position (x, y, z) of the sensor, and IMU is an abbreviation of the Inertial Measurement Unit providing the rotation angles (pitch, roll, and yaw) of the sensor. Airborne laser scanning is done from either a fixed wing aircraft or a helicopter, and completed with a GPS ground station for off-line differential GPS (DGPS) calculation. A digital camera is often complemented with a laser scanner.

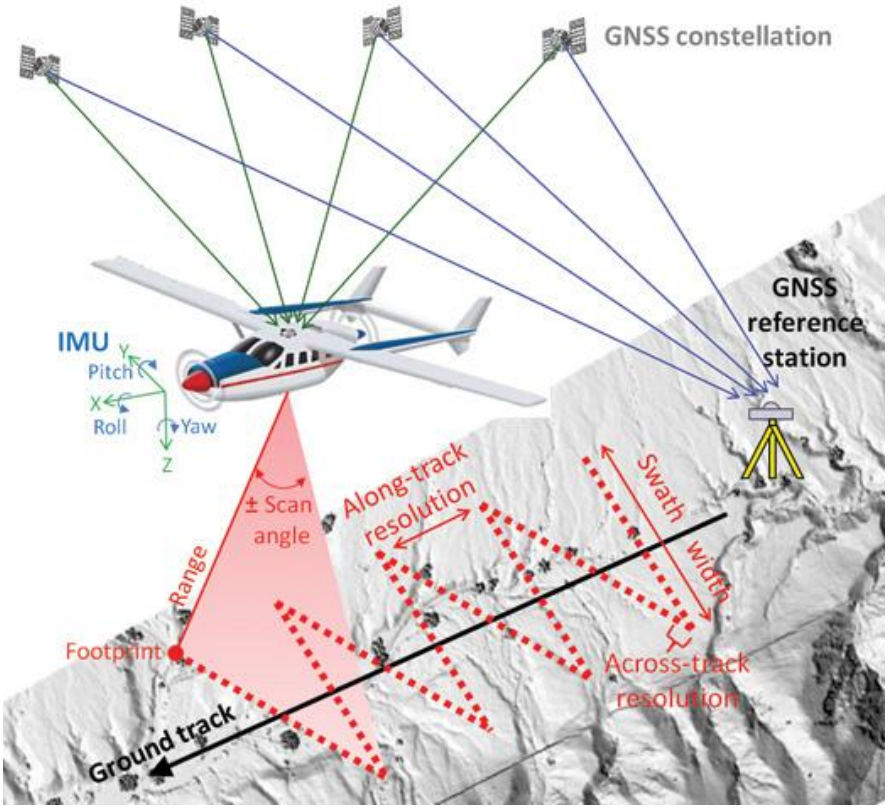

Figure 2.1 Basic principles of an airborne LiDAR mapping system

(Source: Fernandez, 2011)

Basic principles of an airborne LiDAR mapping system are shown in Figure 2.1. Some important parameters are introduced below (Vosselman *et al.*, 2010, Chapter 1; Wehr and Lohr,

1999). For a given flying height above ground h, and the full scan angle θ, the swath width, which is also called the field of view (FOV) on the scan angle θ, can be calculated.

$$sw = 2h \tan \frac{\theta}{2} \tag{2.1}$$

Assuming the spot shape to be a circle, as the same relationship, for the full angle of beam divergence is γ, the diameter D of the illuminated laser footprint on the ground is :

$$D = 2h \tan \frac{\gamma}{2} \tag{2.2}$$

The most direct ranging measurement from the laser scanner to a ground spot is measuring the traveling time between the emitted and received pulse, which is called the time-of-flight. The traveling time of a light pulse is:

$$t = 2\frac{R}{c} \tag{2.3}$$

where R is the distance between the ranging unit and the ground spot, and c is the speed of light.

Some unique properties of LiDAR data can help with the detection and extraction of power-lines from other surface features: laser points are random and not selective; there might be more than one echo of the laser; and the airborne LiDAR systems deliver the intensity of the returned laser beam (Clode and Rottensteiner, 2005). A single laser pulse can have multiple echoes and each echo represents a reflection from a target. When the laser illuminates an object, a time-of-flight receiver usually can capture up to four echoes per pulse: first, second, third and last (Vosselman *et al*., 2010). Different echo signals return from different taget situations. The multiple echoes allow us to capture the tree tops, intermediate vegetation and the ground. For the

power-lines, as there are generally no other surface features above the power-line area, they are mainly concentrated in the first echo.

2.1.2 ALS Corridor Mapping Systems

Currently, the international mainstream commercial LiDAR companies are Leica Geosystems Ltd, Optech Inc., and Riegl Inc. The ALS systems in these companies have different advantages in corridor mapping. Here the primary equipment will be introduced.

1) Leica ALS Corridor Mapper

Leica offers a system of the Leica ALS Corridor Mapper, which is targeted to both lower altitude and corridor mapping markets (Leica, 2013b). The ALS Corridor Mapper system consists of the following standard components: LS60 scanner assembly, system electronics (LC60 laser controller + SC60 system controller), interconnecting cables, OC52 operator interface, vibration isolated interface plate assemblies for both scanner and electronics, and GNSS + GLONASS antenna (Leica, 2013a).

The ALS60-series are no longer in production, and have been replaced by the ALS70 now. The advantages of the ALS Corridor Mapper are productivity (true 200 kHz performance without sacrificing accuracy), accuracy and flexibility (peak performance over the entire operating envelope). The system produces data after post processing with a lateral placement accuracy of 8 - 9 cm and vertical placement accuracy of 6 - 18 cm (one standard deviation) from full-field-filling targets of 10 percent diffuse reflectivity or greater with atmospheric visibility of 23.5 km or better for flying heights up to 1000 m AGL and nominal FOV of 40 °. Accuracy estimates for particular mission profiles (i.e., flying height above terrain and position within FOV) are shown

below and can be provided in detail by using the AeroPlan mission planning template. Estimates below are made assuming a 40 °FOV and a nominal 5 cm GNSS error (Leica, 2013a).

2) Optech Airborne Laser Terrain Mapper (ALTM)

Optech offers three series of ALS terrain mappers: ALTM Orion for ultra-compact mapping, ALTM Pegasus and ALTM Gemini for wide area mapping. The Orion-C is a low- altitude system for corridor applications where maximum object details are required. Here is an application of Orion-C in corridor mapping as it is the lightest and smallest complete LiDAR solution in the marketplace at 57 pounds and a 1-cubic foot volume (Optech OR-001, 2013). The advantages of Orion-C in corridor mapping are high data collection rate and ground point density (up to 200,000 points/second (200 kHz)); the roll compensation feature enables the Orion-C to track the corridor accurately; dynamic range of intensity (12-bit) ensures data accuracy in surveys where strong variations in return signals are expected, which is precisely the case in power-line survey; the 1.5 micron laser which delivers eye-safe operation at altitudes as low as 35 meters in densely populated areas (a low-altitude surveying); with an internal 256-GB solid state drive (SSD) provides a cost-effective, commercial solution when compared to a traditional embedded HDD system; and high data accuracy in millimeters range instead of the centimeter range for a 3D point cloud of a power-line conductor (Optech, 2013).

ALTM Gemini is a wide-area, high-altitude LiDAR mapping system incorporating the industry's only fully-automated continuous multi-pulse (CMP) technology system (Optech Gemini, 2013). It has the features of dual beam divergence, integrated video capture, CMP technology, GPS, GLONASS and L-band capable, waveform digitization option, and fully integrated imaging sensor options. It has advantages of rapid coverage and data output capability

(167 kHz effective laser repetition rate); unrestricted bank-angle capability while maintaining high data accuracy and integrity; intensity capture with large dynamic range resulting in exceptional LiDAR image quality; and ability to operate efficiently in all application areas and altitudes with maximum data density (Optech Gemini, 2013). Taking all the ALS systems into account, when it flies at a low altitude like 1000 m, the captured data from ALTM Gemini can be used to do power-line corridor surveys for lower cost-effectiveness.

3) Riegl Fully Integrated Airborne Mapping System

Riegl offers a rapid, highly accurate and efficient method of capturing 3D data of large areas, such as agricultural or forestry sites, urban areas, industrial plants, power-line or railway corridors, etc. Riegl LMS-Q 1560 fully integrated cutting-edge airborne scanning system is a new high performance, long-range ALS system that can be used in corridor mapping (Riegl USA, 2013).

The main features of the Riegl LMS-Q 1560 are: up to 530,000 meas. /sec on the ground around 15,500 ft; multiple time around processing up to 10 pulses; full waveform analysis for unlimited number of target echoes; high laser pulse repetition rate up to 400 kHz; high ranging accuracy 20 mm; wide scan field of view up to 60°; and suited for measuring snowy and icy terrain ((Riegl USA, 2013).

2.1.3 LiDAR for Power-line Mapping

LiDAR has experienced explosive growth over the past decades and is more popular. Classified by platforms, there are ground-based, airborne and space-borne LiDAR, while ground-based LiDAR includes static terrestrial laser scanning (TLS) and mobile laser scanning (MLS). For power-line inspection, all of these three methods can be employed. Airborne and terrestrial laser

scanners capture and record the geometry and sometimes textural information of visible surfaces of objects and sites (Vosselman *et al*., 2010).

1) Ground-based LiDAR for Power-line Mapping

TLS is usually used in a small-area measurement as it is from a laser scanning system mounted on a tripod. TLS has the fixed position, scanning in vertical and horizontal directions.

MLS is a modification of ALS with GPS/IMU, but operated from the top of a ground mobile laser scanning system like a vehicle or ship (El-Sheimy, 2003; Holopainen *et al.*, 2013; and Vosselman *et al.*, 2010). MLS is a rapidly evolving technology that provides improvements in efficiency and safety over static TLS, while still providing a similar level of accuracy and resolution.

As the MLS data is relatively cheaper and easier to capture, it can be used to detect and extract the power-lines in urban areas. 3D street-scene modeling developed rapidly with emerging expansion of location-based services, pedestrian and vehicle navigation, traffic accident, or crime case investigation (Kutterer, 2010; Yang *et al.*, 2012). However, rarely do specific papers present the extraction of power-lines using MLS data. In recent years, the methods for power-line extraction are still mostly focused on ALS data and the method of ALS data processing becomes relatively more mature than that of MLS data processing.

2) Airborne LiDAR for Power-line Mapping

Airborne laser scanning (ALS) is a method based on LiDAR range measurements from an aircraft. The 3D position (x, y, z) of the reflecting object is defined by the precise orientation of the measurements between the object and a sensor which has a known position using a DGPS and IMU techniques.

As the sensor technique has improved, by using the ALS data, objects with small diameters like power-line cables can get dense, fast and accurate measurements (Melzer and Briese, 2004). The application of ALS data on power-line corridor mapping has already been taken into commercial basis since 1995, and thousands of kilometers of power-lines have already been mapped by FLI-MAP system in recent years (FLI-MAP, 2007; Reed *et al.*, 1996; Vosselman *et al.*, 2010).

For the ALS data, three categories of proposed techniques to model power-lines are divided as 3D point-based approaches (Melzer and Briese, 2004; Clode and Rottensteiner, 2005; McLaughlin, 2006; Jwa *et al*., 2009; Jwa and Sohn, 2010; and Jwa and Sohn, 2012), two-dimensional (2D) image-based approaches (Yan *et al.*, 2007 and Li *et al*., 2010) and fusion of laser scanning data and aerial imagery which is mainly used in the building extraction.

Classification is a common way to separate the power-lines and other surrounding features. McLaughlin (2006) developed a way to classify the point cloud into three categories: power-lines, vegetation and surface. The classification is done in ellipsoidal neighborhoods along the direction of flight. Ensure that each ellipsoid contains points that belong to one same power-line, and then calculate the covariance matrix. Finally, the three classes are modeled with a Gaussian mixture model using the expectation maximization algorithm. However, this method will generate many noises when detecting the power-line points, and the extracted power-lines are intermittent and not continuous (McLaughlin, 2006). Later, McLaughlin's method has been modified so that the points are separated by voxel (voxel-based) and sphere (point-based), and the classification is done with eigenvalues (Jwa *et al.*, 2009) and using Random Forest (Kim and Sohn, 2010). Noises are reduced after the use of Eigen ratio and point density in the improved method, but also some points belonging to the power-lines are lost.

As a state-of-the-art data acquisition method, a whole workflow of power-line point data processing, analysis, and corridor clearance can be completed within 72 hours for providing rapid mapping service uninterrupted in an airborne LiDAR data processing platform (Neal, 2009).

As airborne LiDAR can acquire a large area of power-line corridors to keep the consistency effectively in a long distance, especially for the corridors which are built on the mountains where the MLS and TLS systems are hard to deliver, the airborne LiDAR data are usually used widely in the power-line extraction and reconstruction study.

2.2 LAS Data Formats and Structures

2.2.1 LAS Data Formats

ASPRS developed the LAS format for airborne sensors (ASPRS Standards Committee, 2010) which has been successfully integrated into several software platforms and has become the standard in the ALS industry. The LAS format is a public format for the interchange of 3D point cloud data between data users. As listed in Figure 2.2, the LAS format contains binary data consisting of a Header Block, Variable Length Records, and Point Data. The Public Header Block contains generic data such as point numbers and coordinate bounds. The Variable Length Records contain variable types of data including projection information, metadata, and user application data. The Point Data records the X, Y, and Z 3D coordinates, intensity, returns and other attribute information (ASPRS Standards Committee, 2003). These three parts are interconnected and closely linked. For example, the Public Header Block records the starting position and the total number of points for the Point Data, and regulates the length and format for every point data. Public Header Block has the number of Variable Length Records; meanwhile the Variable Length

Records keeps the records of the auxiliary information in the Point Data like the metadata information, geographic reference information and projection information.

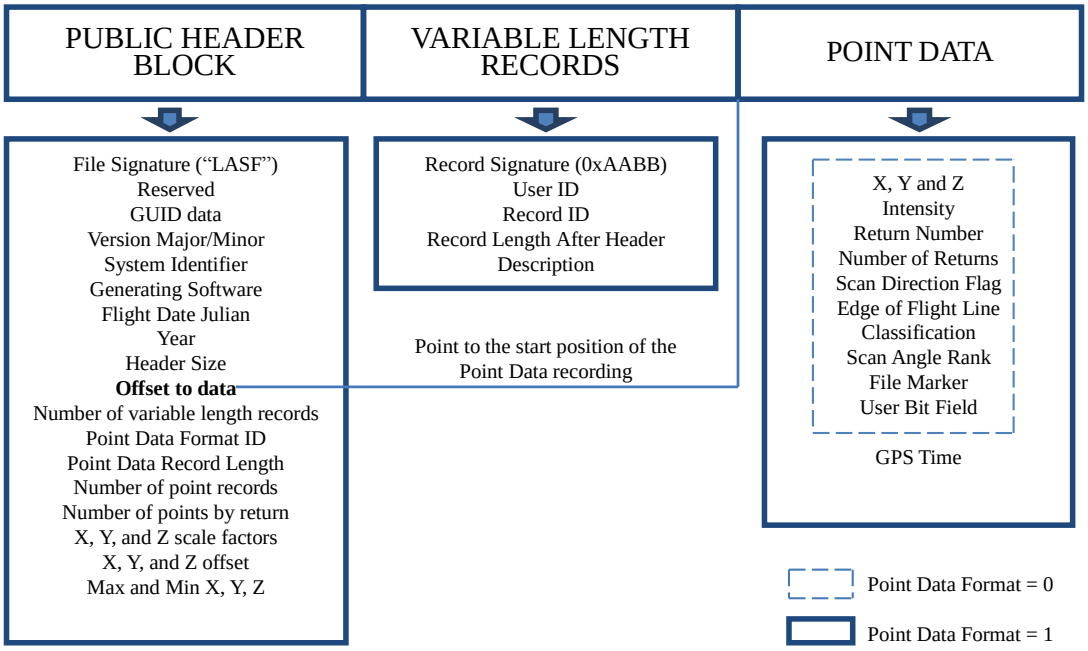

Figure 2.2 ASPRS LAS 1.0 Format

As listed in Figure 2.2, we can find the contents of every of the three category in the LAS 1.0 Format. In the Point Data, there is a lot of LiDAR point information. In the LAS 1.0 Format, a total of 100 kinds of point record formats from 0 to 99 can be defined, but in the same LAS file only one LAS point format can be used, and it should be the same as the Public Header Block. Format 0, which is the most basic point record format, is defined by the ASPRS Standards Committee. Other point formats are based on the format 0 for extension. For example, the usual format 1 is adding the double floating point time tag value based on the format 0.

The LAS 1.4 Specification was approved by the ASPRS Board on November 14, 2011 and is the most recent approved version of the document. The airborne LiDAR data collected in this study is in LAS 1.1 Format. In Section 3.4 of power-line extraction studies, the LAS data is transformed into LAS 1.0 Format for processing.

2.2.2 LAS Data Structures

As the original laser points are irregularly distributed, using data structure to organize them is important during the LAS data processing and the further feature extraction. Some data structures, which are usually used in practice, are reviewed before the experiments: regularization image, Delaunay triangulation, octree and k-D tree (Vosselman *et al*., 2010).

The regularization image is a basic but useful data structure for 2.5D data. The original laser points are gridded and rasterized to make them regular. 4- or 8- connected neighbors of a pixel can be defined by the image raster. In this way, it requires relatively little memory and more efficiency.

The Delaunay triangulation is also a popular data structure. The convex hull of laser points are divided into a set of triangles and a circle through the three points of any triangle does not contain any other point of the point set (Okabe *et al.*, 1992; Vosselman *et al*., 2010). A triangulation is usually defined within the XY plane; it is also a kind of 2D raster data structure, but more time consuming than the regularization image.

An Octree is the 3D analogue of a quadtree. An octree structure organizes LiDAR point cloud into clusters of 3D planes. The point cloud set is split hierarchically on the octree structure until the points contained in each sub-node are coplanar, or are distributed in a 3D plane or less than 3

points (Wang and Tseng, 2004). The octree is useful as a 3D data structure but less efficient than the k-D tree.

A k-D tree of data index is a k-dimensional binary tree, which is more balanced hierarchically split LiDAR point sets than an octree. As for the k-dimensional data, more than one key word (which is usually a number with a certain attribute, e.g., the coordinate on the x axis) is needed. A k-D tree defines key word based on each node, and the coordinate on each axis will act as the key word in turn (Hu, 2003; Liu *et al*., 2008). The k-D tree is better in avoiding empty cells and distributing points. However, for a large quantity of point cloud, it is too time consuming.

2.3 Power-line Detection and Extraction from Airborne LiDAR Data

The power-line system is an interconnected network of generating plants, transmission lines, and distribution facilities (CFE, 2008). Vegetation and power-lines are the main objects in power-line corridors, especially for the high voltage transmission lines in rural areas. Power-line corridor mapping requires the information of power-line status and surrounding trees. With the development of remote sensing technology, the resolution of aerial digital cameras is higher, and the airborne laser scanning systems are improved.

The ALS technique is useful for the monitoring of outdoor engineering constructions, like railways, dikes, pipelines and overhead transmission lines (Tao and Hu, 2002; Vosselman *et al.*, 2010). After the detection and extraction of power-lines, the parameters describing the geometry of individual span lines are required to build power-line models. These can be applied both to access the quality of the spans themselves and to determine the distance of the surrounding vegetation from the spans.

For the power-lines, the reconstruction needs to be done after line feature detection and extraction. In computer vision and image processing, feature detection is a method that can compute abstractions of image information and making local decisions at every image point whether it is a feature point or not. Feature extraction is a method to represent the feature points detected. The extracted feature can be represented in a simple way especially for the task using only the relevant information from the input data set.

Power-lines are hanging several meters above the ground in parallel linear structures. Due to the fact that power-lines are often coated with a black plastic cover and it is usually a thin linear feature of the target area, the reflection of a power-line is low. When scanned by an ALS system, the power-lines are usually in the first echo. If a pixel size smaller than 0.5 m is used, the individual cables will often be separated by at least one pixel in the gridded image.

2.3.1 Filtering of Airborne LiDAR Point Clouds

The point cloud is usually filtered to eliminate unnecessary points, such as clouds and birds, or in the case of this study, the ground under the power-lines and unwanted vegetation. Filtering is also commonly done to reduce the file size of the deliverable point cloud since the full dataset can require intense computational power and data storage. Usually, the filtering is considered as the extraction of the DTM from the DSM, and the classification is regarded as distinguishing different objects such as vegetation, buildings, roads, power-lines, etc. from the laser point cloud data. Besides the determination of terrain, the extraction of buildings, vegetation and other important features above the ground are also worth considering.

The features of power-lines are listed below:

1) Power-lines are linear objects with small curvatures on the aerial imagery (Yan *et al.*, 2007);

2) They hang above ground and have certain distance from the ground surface: the height substantially equal in the local small area;

3) The intensity differs between power-lines and vegetation in Airborne LiDAR data;

4) The power-line points are linearly distributed throughout the entire data area with strong extension;

5) Between the two adjacent poles, the power-lines projection in the horizontal direction are parallel straight lines;

6) Power-lines belong to the natural catenary, and its data model generally conforms to the hyperbolic cosine function (McLaughlin, 2006);

7) There are generally no other surface features above the power-line area, so the power-line information is mainly concentrated in the first echo for the Airborne LiDAR data;

8) A power-line cable diameter is typically between 8 and 25 mm (Vosselman *et al.*, 2010).

Based on the power-line properties, here are some of the usually used filtering techniques: filtering based on returns (first, second, third, and last); filtering based on the selection of every ith point; filtering based on height; and also filtering based on octree, k-D tree, elevation, range, and intensity (see Vosselman *et al.*, 2010, for examples of filtering algorithms). Note that octree and k-D tree structures are also generally used as data organization schemes to improve interactivity of the dataset.

An iterative algorithm based on linear prediction (Kraus and Mikhail, 1972) with an individual accuracy for each measurement using linear least squares is proposed by Kraus and Pfeifer (Kraus and Pfeifer, 1998). The algorithm based on triangular irregular network (TIN) densification proposed by Axelsson is also a classic one. First, go through some low elevation seed points in each grid to generate an initial sparse DEM; then calculate the distance between each point and DEM and triangulation vertex angle, and densify iteratively layer by layer (Axelsson, 1999; Axelsson, 2000). A culling mechanism is proposed to do further filtering in the power-line pre-processing (Melzer and Briese, 2004). First a digital terrain model (DTM) is extracted using the iteratively reweighted least squares M-estimation (Kraus and Pfeifer, 1998); after removing the DTM, in a 1 m by 1 m gridded XY plane, 1 is assigned to all non-empty cells (1-cells), and 0 to others (0-cells); then for the 1-cells, the cells having no or more than 3 1-cells in 8-neighbours are removed. This method is an efficient filter for the following power-line extraction.

2.3.2 Power-line Detection and Extraction

Hough transform is a common and efficient method in power-line extraction (Melzer and Briese, 2004; Liu *et al.*, 2009). It is a classic method of image recognition, which is a commonly used linear detection algorithm. Hough transform is a type of voting scheme, which lets each feature vote for all the models that are compatible with it. A line in the image XY plane is defined as

$$y = mx + b \tag{2.4}$$

where parameter m is the slope and parameter b is the y-intercept of the line. A line in the XY plane is defined by

$$b = -xm + y \tag{2.5}$$

corresponding to point (m, b) in the m-b space. Since a 2D line has a total of two degrees of freedom, it can be described by a two-parametric model or a model with more than two parameters and additional constraints (Kappa and Gröll, 2006). Lines in the image space can also be described in polar form (Hessian normal form):

$$\rho = x\cos\theta + y\sin\theta \tag{2.6}$$

where ρ is the distance between (0, 0) point and the line, and θ is the angle of the normal to the line with the x axis. If the polar equation of lines is used, for each point in an image, a sinusoidal curve rather than a line are drawn in the accumulator array. The process of line detection by classic Hough transform can be depicted in Figure 2.3.

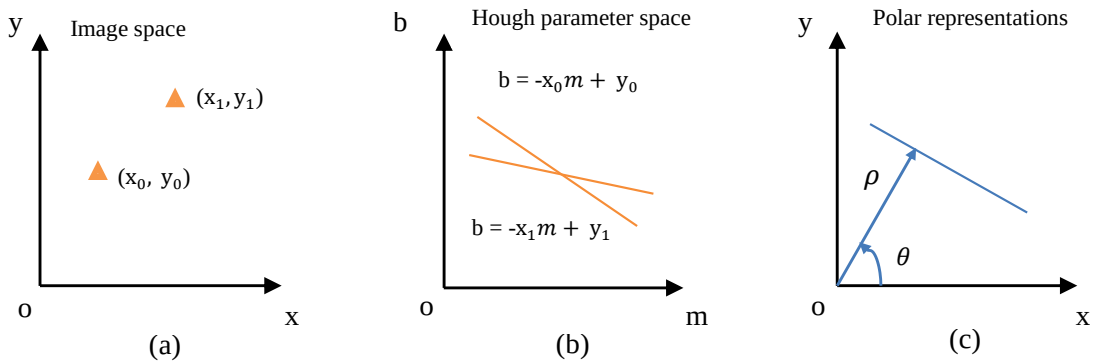

Figure 2.3 Different presentations of lines in Hough transform

To avoid noise, only local peak counts that are larger than a pre-specified threshold value may be considered (Goshtasby, 2005). The advantages of Hough transform are:

- capable of dealing with non-local and occlusion;
- capable of detecting multiple instances of a model in a single pass;

- Sensitive to noise: noisy points will not affect the outcome of the Hough transform if the majority of given points are not noisy (Goshtasby, 2005).

The main advantage is the ability to detect the geometry less affected by the interference of intermittent points and does not require pre-combination or connected edge points. The disadvantages of Hough transform in the power-line detection are that, a good grid size is hard to decide; the searching time increases exponentially with the number of model parameters; high computational cost and some spurious lines.

RANdom SAmple Consensus (RANSAC) algorithm is an iterative model-fitting method proposed by Fischler and Bolles (1981). RANSAC generates candidate solutions by using the minimum number of data points to estimate model parameters, which means that the smallest set possible with consistent data points to enlarge the set is conducted (Derpanis, 2010). The advantage is that it can cope with the input data with a large amount of outliners efficiently. However, it can only detect and extract one line in a single pass, and the line can often be a spurious line. The algorithm parameters must be carefully chosen to estimate a high level model.

2.4 3D Power-line Reconstruction and Management

2.4.1 3D Power-line Reconstruction

Currently the 3D power-line reconstruction algorithms are usually based on data filtering followed by the detection and extraction of power-line candidates in Chapter 2.

Least-squares line fitting can be conducted when the coordinates of a number of points on a line are known. In this study, it can be used after the extraction of power-lines, following the process of Hough transform. Least-squares is a mathematical tool to determine the unknown

parameters of an analytic function in which a set of noisy samples are available (Goshtasby, 2005; Rivlin, 2003).

The polar equation of a line can be represented as

$$Ax + By + C = 0 \tag{2.7}$$

where $A = \cos\theta$, $B = \sin\theta$, and $C = -\rho$. For the given point data set, the distance of any point $(x_i,\ y_i)$ to the line is given by

$$d_i = | Ax_i + By_i + C | \tag{2.8}$$

The line where the sum of squared distances from the points to the line is minimum

$$E = \sum_{i=1}^{n} (Ax_i + By_i + C)^2 \tag{2.9}$$

$$A = \pm \frac{d\bar{x} - b\bar{y}}{\sqrt{(a\bar{y} - b\bar{x})^2 + (d\bar{y} - b\bar{x})^2}} \tag{2.10}$$

$$B = A\frac{a\bar{y} - b\bar{x}}{d\bar{x} - b\bar{y}} \tag{2.11}$$

$$C = -(A\bar{x} + B\bar{y}) \tag{2.12}$$

From Equations (2.9) – (2.12), the value can be set to $A = B = C = 0$, $a = \sum_{i=1}^{n} x_i^2$, $b = \sum_{i=1}^{n} x_i y_i$, $d = \sum_{i=1}^{n} y_i^2$, $\bar{x} = \frac{1}{n}\sum_{i=1}^{n} x_i$, and $\bar{y} = \frac{1}{n}\sum_{i=1}^{n} y_i$. Then the θ and ρ can also be calculated as

$$\theta = \tan^{-1}(B / A) \tag{2.13}$$

$$\rho = -C \tag{2.14}$$

The line will be represented by choosing a smaller E from the parameters selected to minimizing or maximizing the sum of squared distances (Goshtasby, 2005). After finding the line, and adding the height value, the 3D power-lines can be modeled.

Except for the classic method mentioned above, some research has been done. Not many automatic algorithms for a whole procedure of power-line reconstruction have been introduced, only about the extraction and corridor vegetation management.

Jwa *et al.* (2010) conducted a consistent study on automatic reconstruction of 3D power-lines using airborne LiDAR data. A voxel-based piece-wise line detector (VPLD), which was developed based on a well-known perceptual grouping framework by grouping similar features at different levels of information, is introduced. Then, a single power-line model was reconstructed by applying a non-linear adjustment for estimating catenary line parameters to a piece-wisely segmented voxel space (Jwa *et al.*, 2009). The method was improved by correcting incompletely reconstructed power-line models using a multi-level span analysis including inter-span and across-span (Jwa and Sohn, 2010). The manual classification output was regarded as the ground truth. The results showed that the incomplete detected lines in the test data were corrected 100%. Another method they proposed was using a catenary curve model to represent a power-line by first extracting power-line candidate points (Jwa and Sohn, 2012).

A catenary curve, which is defined by a hyperbolic cosine function, can be used to model a power-line (McLaughlin, 2006). A 3D power-line model can be represented with a 2D line, L (θ, ρ) in XY plane, and catenary curve C (a, b, c) in XZ plane:

$$L(\theta, \rho):\ \rho = x\cos\theta + y\sin\theta \tag{2.15}$$

$$C\ (a,b,c): z = a + \mathrm{c}\ \cosh\left(\frac{x-b}{c}\right) \tag{2.16}$$

where θ is the angle of a line's normal vector and X-axis, and ρ is the distance between the line and the origin; a and b are parameters for translation of the origin, c is a scaling factor denoted as the ratio between the tension and the weight of the hanging flexible wire per unit of length; and x, y, and z are the coordinates of the points in 3D space (Jwa and Sohn, 2012).

The appropriate power-line model is chosen from the hypothetical growing models. However, the proposed methods in Jwa's group are using high-density airborne LiDAR data and limited to their test data. The robustness of the algorithm is uncertain to other voltage types and structures. The evaluation of efficiency and accuracy compared to the ground truth are also not fulfilled.

Eigenvector streamlines of the point distribution tensor field are applied to reconstruct the power cable from airborne LiDAR data (Ritter and Benger, 2012). The point distribution tensor is the local geometric properties of a neighborhood distribution within a power cloud by direct visualizing of the covariance matrix (Ritter *et al*., 2012). First, a covariance matrix of neighborhoods in a point cloud is computed, and second streamlines are used to reconstruct lines of points which are linearly distributed. Different weighing functions for the tensor computation are compared and the results show that a smoother weighing and more local interpolation weight are a good combination for linear structure reconstruction. However, as it is a new-proposed algorithm, this method is not automatic in the determination of appropriate combination of weighing functions and their parameters. From visual inspection, the reconstructed power-line curves are not fitting very well. The algorithm still needs to be improved by testing different dataset with ground truth.

2.4.2 Power-line Corridor Management

A transmission grid is comprised of power stations, transmission circuits, and substations. Circuits categorized by 60 kV and above are referred to as transmission lines (e.g. 138 kV, 230 kV, 360 kV, and 500 kV). Energy is usually transmitted with three-phase alternating current (AC). Overhead lines are usually built on steel towers or steel poles, although wood poles are common in rural areas.

A Right-of-Way (ROW) is a corridor of land over which electric transmission lines are located. The ROW width, which is affected by the transmission tower height, distance between towers, line security and many other factors, is an important factor in the corridor designing and management.

Prior to the 2003 blackout (Chapter 1), the North American utility companies were not bound by North America-wide regulations when it came to supplying electricity to customers. The standards issued by the North American Electric Reliability Council (NERC) were, for the most part, followed voluntarily by the utilities. There was no power of enforcement granted to this regulatory body and so NERC could not force utility firms to comply with its standards. Following the recommendations of the investigations into the blackout, NERC became North America's Electric Reliability Organization and now its standards have become mandatory for North American Transmission companies. A NERC official asserted that the 2003 blackout also drove the development of new regulations, such as the Vegetation Management Regulation FAC-003-1. Such regulations will help prevent the disasters associated with power-lines from becoming a reality (Ituen *et al.*, 2008).

As shown in Figure 2.4, at the substations, transformers are used to step the voltage down to a lower voltage for distribution to commercial and residential users. At the point of use, the energy is transformed to low voltage. Large electrical motors switching on and off can cause widely varying sags and surges in electrical AC load. Both sags and surges are the most commonly experienced power quality problem among electronic and computer equipment users (Warkentin-Glenn, 2006).

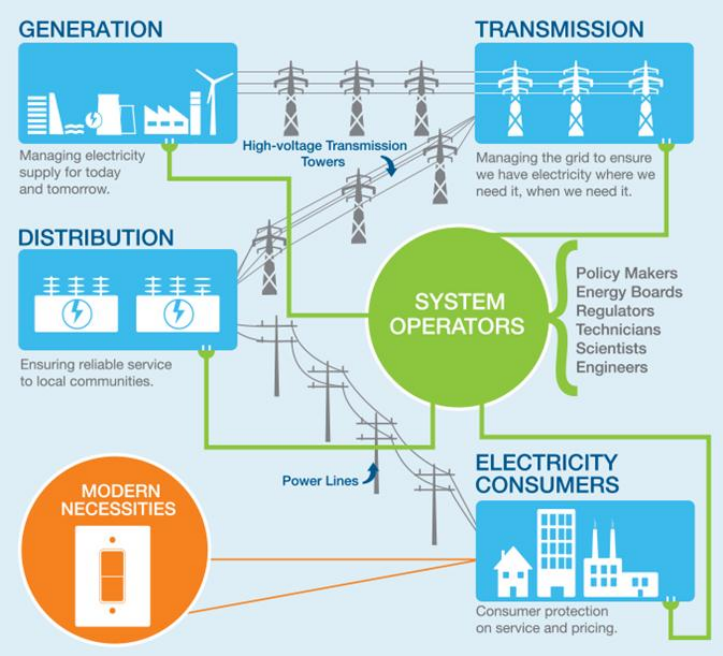

Figure 2.4 A Power Transmission System

(Source: http://powerforthefuture.ca/the-value-of-electricity/how-the-system-works/)

The study area in this paper is within British Columbia, Canada. Regulations for power-lines in Canada fall under the jurisdiction of each province, and the British Columbia Utilities Commission (BCUC) is the provincial authority. The crown-owned electric utility is BC Hydro and Power Authority. Most of the transmission lines in BC are owned by it. So regulations

published both in NERC and BC Hydro are referred to in our study area. BC Transmission Corporation (BCTC) was established in 2003 as the provincial Crown power corporation. The electricity that BCTC's transmission system delivered crosses over 75,000 hectares of land through an interconnected system of more than 18,000 km of transmission lines (nearly enough to travel two and a half times across Canada), which includes the management of 20,500 steel towers, 100,00 wood poles and 287 substations (Guidelines for Development Near Overhead Transmission Lines in BC, 2013). The different transmission towers are shown in Figure 2.5.

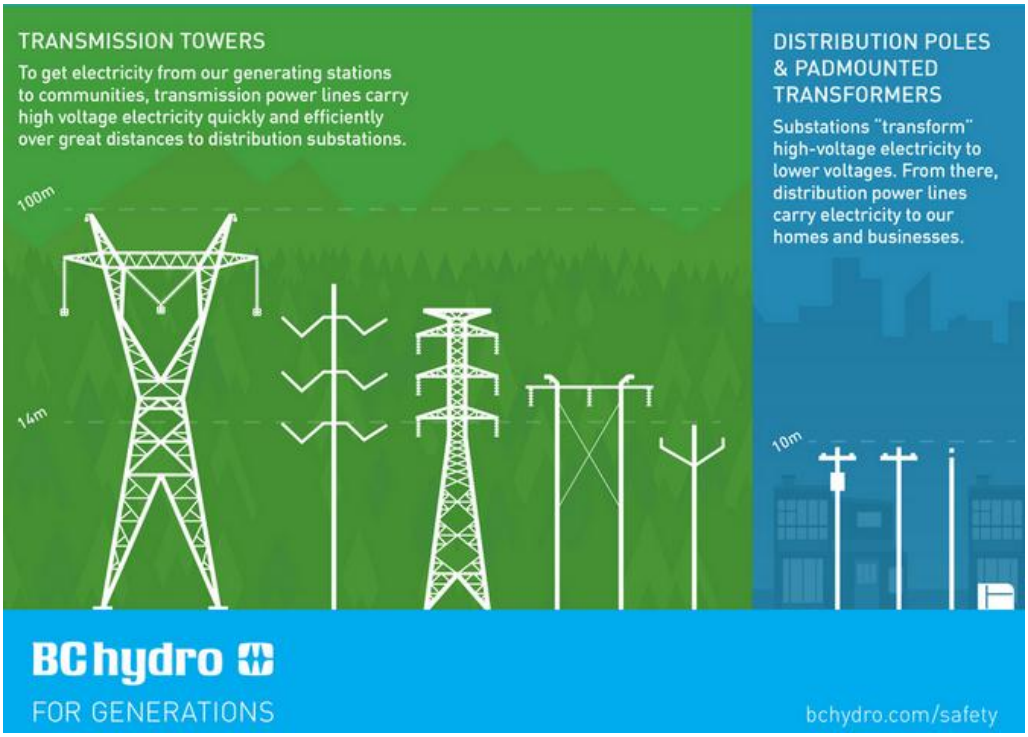

Figure 2.5 Types of different transmission towers in BC, Canada

(Source: http://www.bchydro.com/content/dam/BCHydro/customer-portal/graphics/info-charts-graphs/types-of-lines-infographic.jpg)

One important regulation in BC Hydro is the “Integrated Vegetation Management Plan –For Transmission Rights-of-Way # 105-977-2010/2015”, which was issued on July 2010, lasting to 2015. From the regulation, we know clearly that the major cause of power failure is the contacting of trees to power-lines, as BC has some of the tallest and fastest-growing trees in North America, according to the above-mentioned plan.

Conifer species such as Douglas fir, spruce, and pine, and deciduous species such as alder, birch, aspen, and maple, can grow into power-lines or fall onto them and even start forest fires. In addition, thick vegetation can prevent line workers from getting to a downed line in an emergency or for routine maintenance.

In a direct quote from the plan mentioned above, “BC Hydro’s vegetation management program must:

- minimize public and worker safety hazards,
- reduce the number of outages due to vegetation sources,
- reduce the risk of fires caused by trees contacting the lines, and
- allow access and lines of sight for maintenance. ”

As a utility in North America, BC Hydro is required to ensure that there are no outages on the transmission system caused by trees growing into the lines, under the NERC standard FAC003, Vegetation Management. A project that collects, records, analyzes, and monitors the vegetation in the ROW has been established in BC Hydro.

The current monitoring method of BC Hydro mainly consists of aerial or ground patrols. ROW patrols gather information within each administrative management unit, which is a defined area

within a ROW that has relatively uniform characteristics and can be managed with the same long-term site objectives on a transmission line. From the airborne LiDAR data, we can easily get most information for each AMU. Based on the NERC standard 003, *Vegetation Management*, which requires that a patrol be conducted at least once a year,

BC Hydro has designated the frequency of patrol for those lines joined in BC Hydro system to other utilities and for the specific monitoring requirements based on the knowledge for each area. As the tall growing trees have the potential to reach the overhead power-lines, BC Hydro has set some rules for the limits of approach to a person, machine or conductive material such as a tree, on the ROW, from the Integrated Vegetation Management Plan, as listed in Table 2.1.

Table 2.1 Limits of approach to different power-lines

	Limits of Approach					
Nominal Voltage	69kv	138kv	230kv	287kv	345kv	500kv
Limits of approach for: 1) unqualified workers; 2) all uninsulated equipment	3.0m	4.5m	4.5m	6.0m	6.0m	6.0m

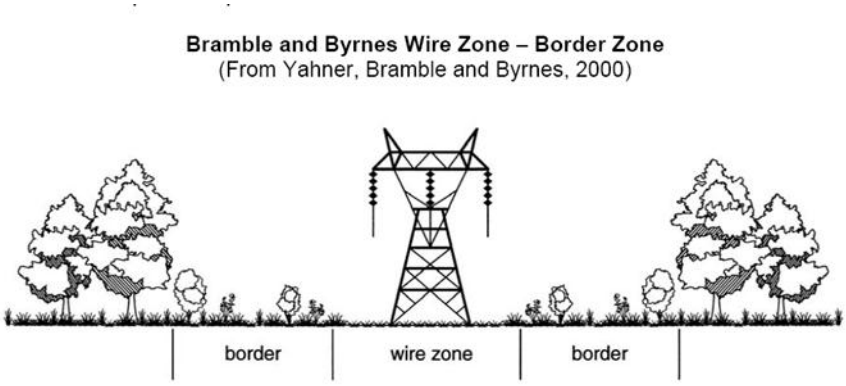

Figure 2.6 An example of ROW design

(Source: Novembri and Cieslewicz, 2004)

An ideal transmission ROW requires managing vegetation to make sure that the surrounding vegetation cannot interfere with overhead power-lines. Figure 2.6 presents a brief idea about the concept (CN Utility Consulting, 2004).

When monitoring overhead transmission lines, two main issues can be taken into account: first the location of the surrounding vegetation, second the condition of the power poles and notably the power-lines themselves (Vosselman *et al.*, 2010).

2.5 Chapter Summary

In this chapter, the background knowledge about different kinds of LiDAR data in power-line corridor mapping, ALS principles and data format, and common commercial ALS corridor mapping systems are introduced. Literature on power-lines detection, extraction, and power-line modeling from airborne LiDAR data are reviewed. data is a feasible and effective tool to fulfill the 3D power-line reconstruction. Hough transform and least-squares line fitting method will be applied in the experiments of this study.

Chapter 3 Power-line Reconstruction from LiDAR

This chapter describes the methodology of a workflow for 3D power-line reconstruction. First of all, the study area, test datasets, software and programming platforms are introduced. Second, a successive workflow is presented for semi-automatic 3D reconstruction of power-lines, including feature detection, extraction and fitting. Then, the accuracy assessment is conducted. Finally, it describes the estimation method for three groups of representative power-line models in the study area and the detection method for hazard trees.

3.1 Study Area and Datasets

3.1.1 Study Area

The City of Nanaimo, located on the east coast of Vancouver Island, British Columbia, Canada (Figure 3.1), has a population of 83,810 people in an area of 91.30 km^2 (Statistics Canada, 2011).

The study area is within a 138 kV power-line corridor in the suburb of Nanaimo, bounded by Westwood Lake, roads, and dense vegetation. Three groups of power-lines run through the corridor. This area is ideal for the research on power-line reconstruction and management because dense vegetation surrounds all three configurations of pylons for 138 kV power-lines found in BC (Figure 3.2).

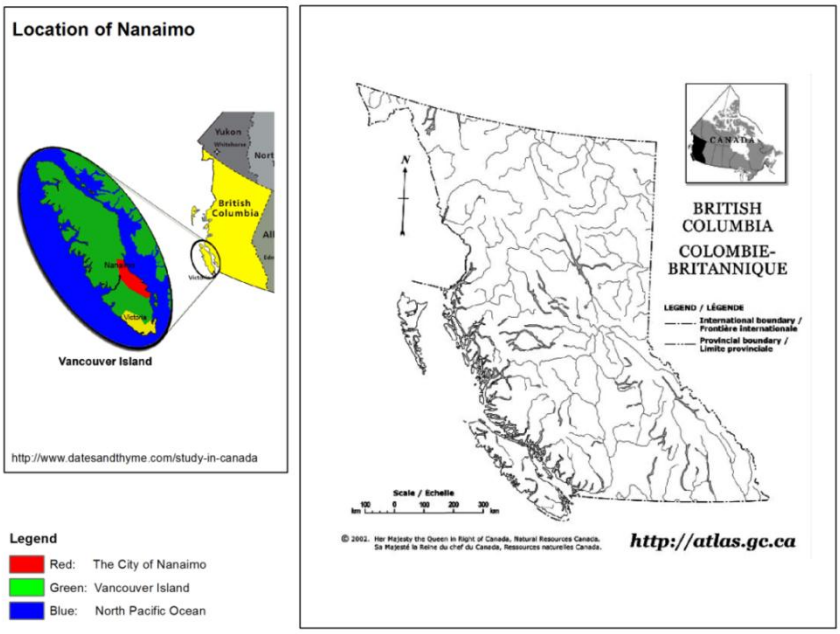

Figure 3.1 Location of the City of Nanaimo

(a) Southeast suburb of Nanaimo, BC, the red rectangular indicates the study area (Google map, 2013)

(b) Three groups of power-lines in the study area

Figure 3.2 Location of the study area, Nanaimo, BC

3.1.2 Datasets

The data used in this study were provided by the City of Nanaimo, including an ALS point cloud dataset and an aerial orthophoto as a reference data. The aerial photographs were captured between March 29 and April 5, 2009, at a spatial resolution of 10 cm and orthorectified to a positional accuracy of 10cm RMSE at a 90% confidence level.

The airborne LiDAR dataset was acquired in 2009 by the Hauts-Monts Inc., a subsidiary of Groupe Alta. The Optech ALTM Gemini (Figure 3.3) was mounted in a fixed wing aircraft. The average flying height was 1000 m giving a swath width of 574 m and a scan angle of 32°. According to the metadata provided by the GIS specialist from the City of Nanaimo, 50 ground control stations were established, and a test site operated by the British Columbia Institute of

Technology (BCIT) was flown over at the beginning and end of each flight for calibration purposes.

Figure 3.3 Optech ALTM Gemini Equipment

(Source: http://www.optech.ca/gemini.htm)

Table 3.1 summarizes the flight parameters utilized in the capturing of airborne LiDAR data. The raw data was converted from GPS/IMU to ground coordinates using Optech DASHMAP software. Secondary processing into final classification was completed using TerraSolid software. The geodetic position of the study area is 49°9′18″ N, -124°W. The projection is UTM/WGS84, Zone 10N.

Table 3.1 Flight parameters of the airborne LiDAR data

Field of view (FOV)	36°
Points density	5.0 points/m²
Swath overlap	30%
Expected final Horizontal accuracy	±0.25 m
Expected final Vertical accuracy	±0.15 m
Maximal distance from GPS Base Stations	40 km

The raw LiDAR data offered by the city of Nanaimo was in LAS Format 1.1 with a total of 16,434,242 points covering a land area of 2,000 m by 2,000 m, including not only a part of power-line corridors, but also a large area of forest, half of a lake, parts of the urban infrastructures, and residential area. In the preprocessing, a smaller piece of test data containing most of the power-line corridor is clipped for the latter process.

3.1.3 Workflow

A successive workflow is conducted to the test data by filtering, detection, and extraction, fitting and 3D reconstruction. The platform of Visual Studio C++ 2010 and Matlab 2013 are used to conduct automated detection, extraction, fitting and reconstruction of the power-lines, with the algorithms proposed in the study aided with the remote sensing software ENVI, GIS softeware ArcGIS 10.1, and lastools from the rapidlasso ((c) 2007-2013). The lastools is used to preprocess the raw LiDAR data. The ArcGIS and Quick Terrain Reader are used to display the point cloud.

The workflow is proposed to reconstruct power-lines in the 138 kV corridors and offers the hazard trees information for the corridor management (Figure 3.4). It starts with the preprocessing of raw LiDAR data. In the filtering stage, first, regularizing of the x and y coordinates of the point cloud in 1 m by 1 m grids; then automatically detecting and extracting the power-lines with regular geometric shape from implementation of algorithms including a density-based filtering algorithm, Hough transform and a concatenating algorithm, which build and distinguish the complete power-lines with a rectangular searching technique. After the fitting of power-lines by a hyperbolic cosine function and least-squares fitting, the 3D reconstruction is completed. Then a case study on the corridor management is conducted by using the extracted power-line corridor information. Finally, hazard trees in the test data are detected, which is important information for the corridor management.

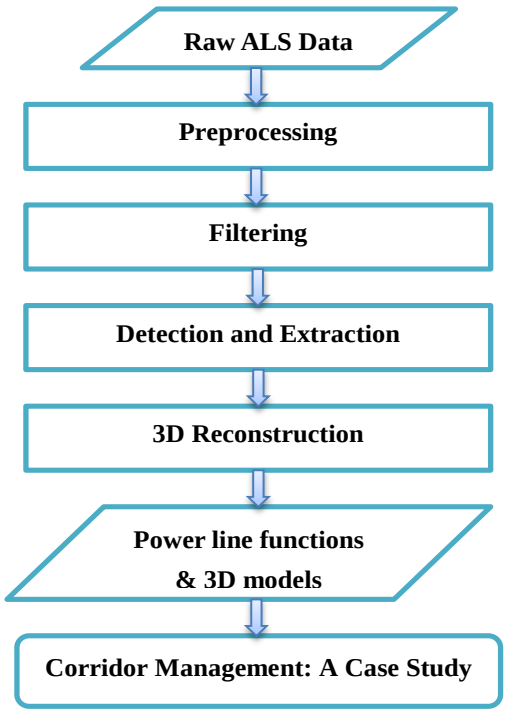

Figure 3.4 Workflow of 3D power-line reconstruction

3.2 Preprocessing of Airborne LiDAR Data

The raw airborne LiDAR data is preprocessed with the lastools. First, the raw airborne LiDAR data is cut with dimension 500 m by 340 m, which contains all three types of power-lines. Then the commands “las2las” and “lastile” in lastools are used to clip the raw airborne LiDAR data in the LAS Format 1.0 (Figure 3.5).

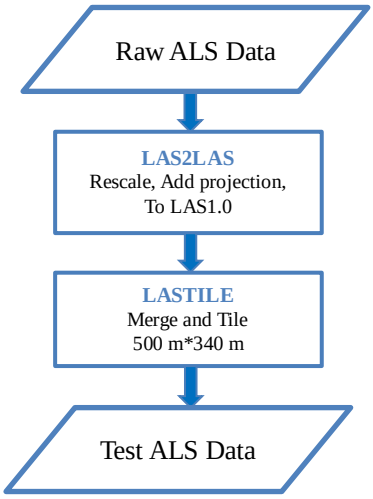

Figure 3.5 Pre-processing of the raw airborne LiDAR dataset

After the preprocessing of raw data, the extents of the test data for the part of 138 kV power-line corridor in the study area are Xmin = 427,000.00 m, Xmax = 427,499.99 m, Ymin = 5,445,180.00 m, Ymax = 5,445,519.99 m, Zmin = 162.01 m, Zmax = 307.45 m. There are 850,117 points all inclusive. The average point density is 5 points/m². By measuring with QT Reader randomly, the average distance between two points is 0.5 m (Figure 3.6).

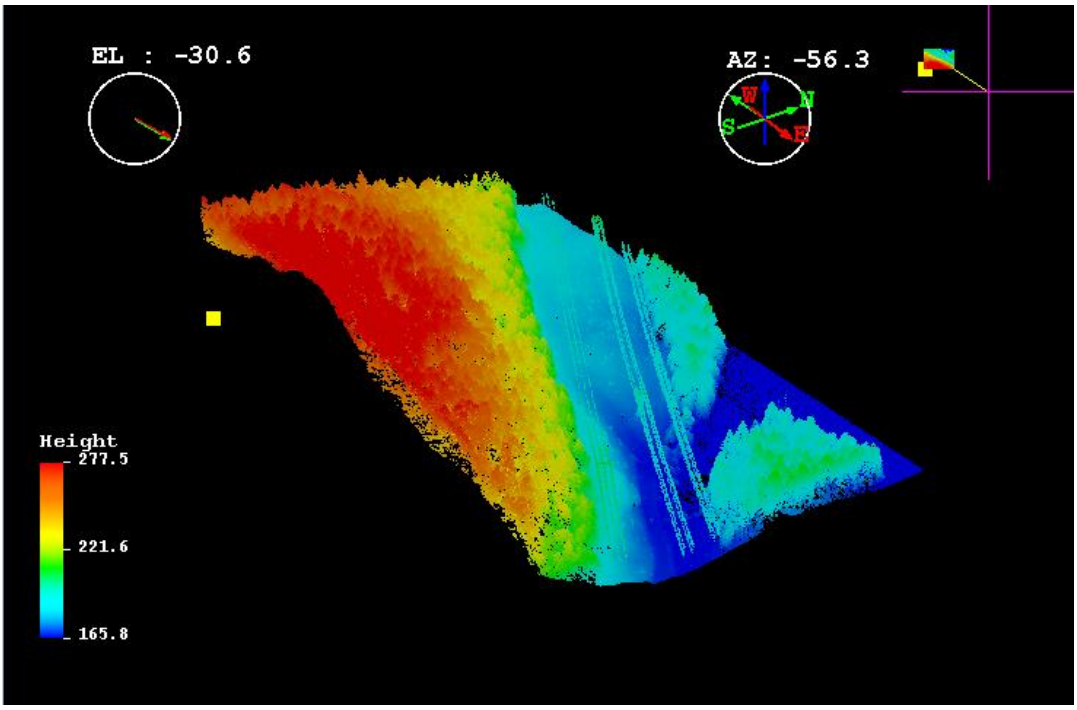

Figure 3.6 LiDAR point cloud of three groups of power-lines (QT Reader)

Table 3.2 lists the three different types of 138 kV power-lines in the study area, which are Power-line Group1 (PLG1), Power-line Group2 (PLG2) and Power-line Group3 (PLG3), respectively. Through the airborne LiDAR data, for PLG1, PLG2 and PLG3, there are three, two, and four pylons, respectively. In conclusion, there are 15 power-lines in the study area, with 60 spans. However, for PLG2, as there is a span that only contains less than 10 points per wire in the 3D point cloud, these six wires are not considered.

Table 3.2 Power-line descriptions in the study area

Number	PLG1	PLG2	PLG3	Total
Wires	3	6	6	15
Pylons	3	2	4	9
Spans	12	12	30	54

Figure 3.7 shows (a) PLG1-typed power-line consisting of three wires and the wishbone wood-pole structure pylons, and (b) PLG2- and PLG3-typed power-lines both including six wires, but with steel lattice pylons, and steel pole structure pylons, respectively.

(a) Wood-pole Structure (b) Steel Lattice & Aesthetic Steel Pole Structure

Figure 3.7 Three 138 kV Pylon types in the study area

(Source: (a) is from the orthophoto, (b) comes from the google earth imagery of the study area)

PLG3 can be divided into two columns of power-lines; each consists of 3 power-lines located in a vertical place, which makes PLG3 different from PLG2. PLG2 and PLG3 both have two columns power-lines with each column consisting of 3 power-lines located in a vertical plane. However, in the projected XY plane, the projection of PLG2 contains 4 lines, while PLG3

contains 2 lines, which makes the PLG3 different from PLG2. The difference among three PLGs makes the detection and extraction method variable for the three PLGs.

3.3 Filtering

Filtering is a key step of the entire process. The subsequent power-lines extraction and fitting are based on this procedure. Filtering and classification are usually conducted in the same procedure, as the classification will be done during the filtering. Before applying the filtering algorithm, the x and y coordinates of point cloud are designated as a 2D rectangle with 1 m by 1 m grids. In each grid, the points keep their own elevations.

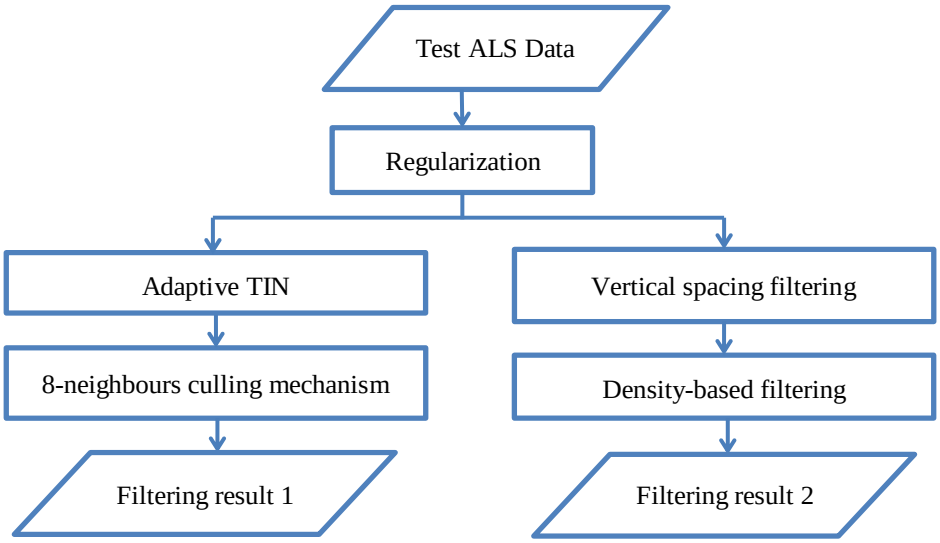

Figure 3.8 Filtering procedure

The filtering procedure is designed by two separate experiments, 8-neighbours culling mechanism and density-based filtering (Figure 3.8). The current filtering algorithm, 8-neighbours culling mechanism (Melzer and Briese, 2004), is applied as a comparing algorithm. As the power-

line corridor is surrounded mostly by the vegetation in the study area, a new filter named “vertical spacing filter” and an improved density-based filter are proposed in this study. Density-based filtering is designed to deal with the power-line corridor filtering, especially with low vegetation under the power-lines.

3.3.1 8-neighbours Culling Mechanism

The first filtering experiment is conducted by trying the 8-neighbours culling mechanism on the airborne LiDAR point cloud without ground points.

First, the “lasground” tool is used to classify LiDAR points into the ground points and non-ground points. The “lasground” tool is based on the Adaptive TIN (TIN densification) algorithm (Axelsson, 1999; 2000). By setting the parameters of “lasground”, the height above the ground for each point can be computed with “-compute_height”, and a height-normalized LAS file can be generated with option “-replace_z”. Then, the points with height below m meters and above n meters can be removed with “-drop_below *m*-drop_above *n*” using option “lasheight”.

Thirdly, after removing the ground points, the grids with points in either 0 or more than 3 8-neighbours are filtered out. In this way, the culling points are prepared for the Hough transform.

More than conducting the 8-neighbours culling mechanism which removed ground points by calculating TIN, the vertical spacing filtering followed by the density-based filtering is also conducted for the experiment to improve the filtering.

3.3.2 Vertical Spacing Filtering

To conduct the density-based filtering, the first step is conducting the vertical spacing filtering algorithm, which is a kind of height clustering. The purpose of the so-called vertical spacing

filtering is to eliminate ground points under the power-lines. As the regularization has divided the points into grids, there are some 3D points with their *x* and *y* coordinates located within the grid. Then sort the points based on their elevations.

According to the power-line features (2) and (7) listed in Chapter 2 (see pp. 44), power-lines are hanging above ground with certain distance and the power-line information is mainly concentrated in the first echo for the airborne LiDAR data. For 138 kV transmission lines, the limits of approach is 4.5 m, the power-lines are regarded as at least 5 m higher than the ground below (Table 2.1). 5 m has been chosen to be the threshold for the height clustering in this study. As the power-lines are the highest objects in the corridor, the ground points and low vegetation grown right under the power-lines can be shown in Figure 3.9.

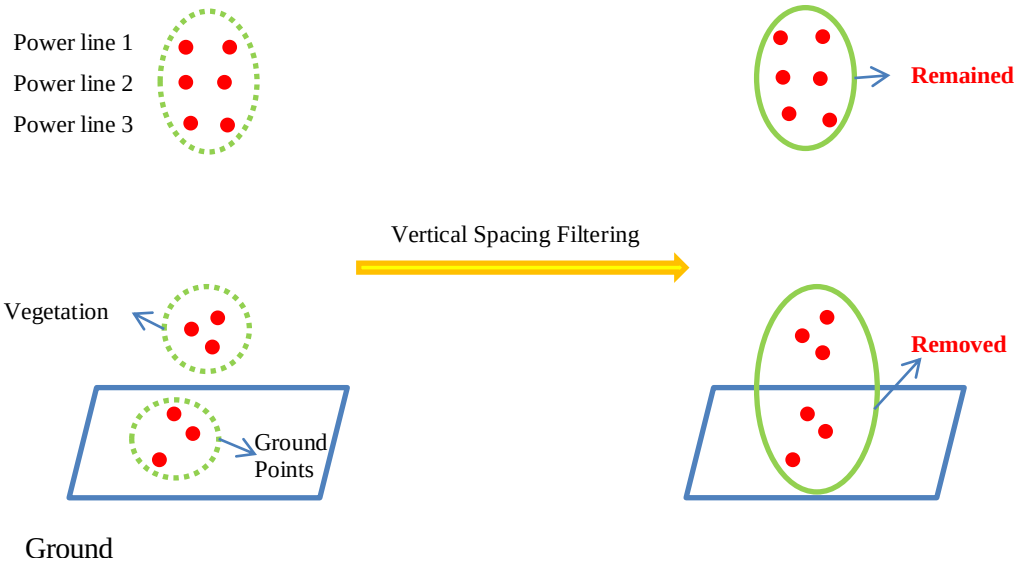

Figure 3.9 Vertical spacing filtering with a grid of power-line points

Specifically, the vertical spacing filtering algorithm designed in this study includes two steps. First, the searching procedure is conducted grid by grid, from the first line, left to right, then to the second line, until the last line of grids. Within each grid, comparing the vertical spacing between each two point starting from the lowest one, if the second lowest one has a vertical distance less than 5 m, then these two points are kept. Second, compare the second lowest one and the third lowest one, until the distance between two points is equal or more than 5 m. The two points and points before are removed. Then start from the next one, until the highest.

In this way, for the grids that contain power-line points, the lowest power-line point should be 5 m higher than surrounding trees, so the trees and ground points under power-lines can be removed in principle. In case there are still outliers which are higher than even the power-line points, in the algorithm, if the highest point in the grid is equal to or over 20 m than the second highest point, the highest point will be removed. This step of vertical spacing filtering is a preparation for the density-based filtering.

3.3.3 Density-based Filtering

The density-based filtering is inspired by Melzer and Briese's culling mechanism (2004). After the vertical spacing filtering and before the detection of power-lines using Hough transform, there is still a large region of vegetation-covered area. Based on the characteristics of the study area, the vegetation areas are with high point density. The density-based filter is designed by using 24-neighbors (5 * 5 grids) in the grid-topology rather than 8-neighors (3 * 3 grids), which enlarges the comparing area to make less power-line points loss. Actually, the outside layer of grids is not directly the neighbors of the middle grid, but they are called as 24-neighbors for better understanding in this study.

For each grid *G*, there are two situations of its 24-neighbors: with points in 24 surrounding grids and without any point in 24 surrounding grids. The two lines of grids respectively located at the up and bottom, left and right, will not participate in the procession as they cannot be the centre points of a 5 * 5 grids. So the first point in the processing is located in row 3, column 3.

For the grid without any point in 24-neighbors, it will be regarded as non-power-line points, and the points within the grid will be removed. For the gird *G* with points in 24-neighbors, compare the maximum elevation $Zmax_1$ with the maximum elevation $Zmax_n$ (where n = (2, 3, ⋯, 23, 24)), in each of the 24-neighbors in the 5 * 5 grids (Figure 3.10). If the value of ($Zmax_1$ – $Zmax_2$) is less than 5 m, then the counter records for one; if it is not less than 5 m, then move to $Zmax_3$, and so on. If the number of records of the counter is greater than 11, then it can prove that the grid *G* does not belong to the power-line points, and will be removed. It's important to note that 11 is an appropriate threshold chosen after many trials to keep the power-line points and remove the vegetation points furthest.

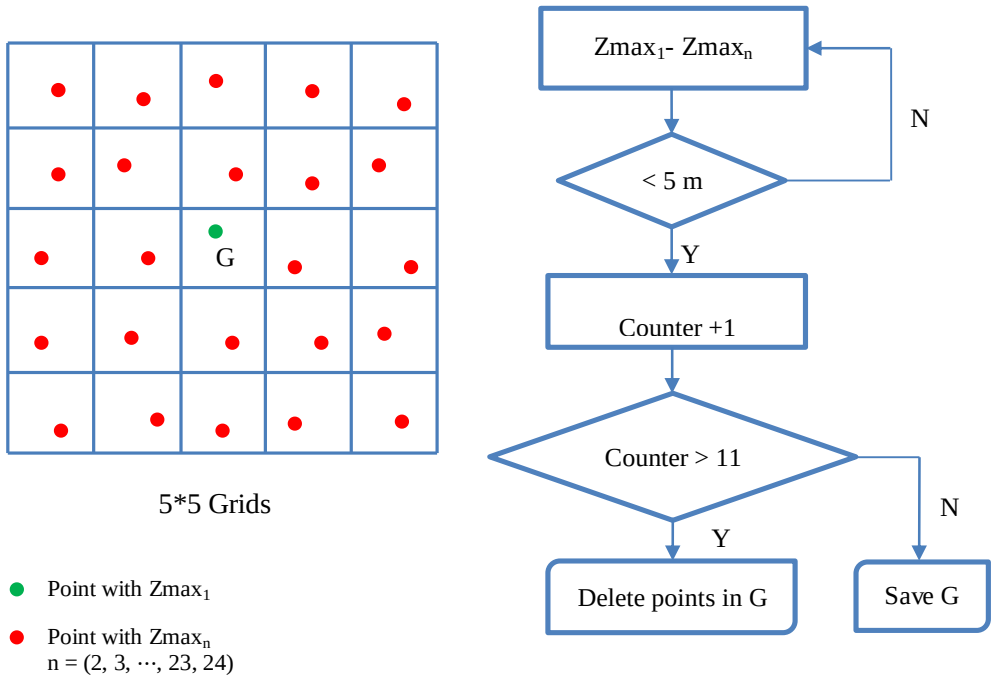

Figure 3.10 Density-based filtering in 24-neighbors with points

3.4 Line Feature Detection and Extraction

3.4.1 Rasterization

After filtering, the remaining points are well prepared for detection. For the reason that there would still be some vegetation points in the point cloud, Hough transform is conducted to detect power-lines in this study.

The filtered LiDAR point cloud is projected onto the ground from 3D to 2D for straight line detection as the trees will be shown as a cluster of points irregular-distributed in the XY plane, but the power-line points will be linear-distributed. Then the projected points are resampled into regular grids. Each grid is a 0.2 m by 0.2 m area. The grids range from (*xmin*, *ymin*) in the lower

left to (*xmax*, *ymax*) in the upper right in XY plane. If there are points (one or more) in a grid, the grey value will be set to 255.

When conducting the projection with the above method, for example, a 3D point (x_0, y_0, z_0) can be projected into a grid in row (i) and column (j), then the points with the same x_0 and y_0 will also be projected into the same grid.

3.4.2 Probabilistic Hough Line Transform

According to the characteristics of the power-line distribution in the airborne LiDAR data, a classic linear feature extraction, Hough transform with the best point chosen in the grid is applied in this experiment.

The polar form of lines mentioned in Figure 2.3 (c), Chapter 2, is $\rho = x\cos\theta + y\sin\theta$ (2.6). In the standard Hough transform, for each point (x_0, y_0), the family of lines that goes through this point can be defined as:

$$\rho_\theta = x_0 \cos\theta + y_0 \sin\theta \tag{3.1}$$

which means that each pair of (ρ_θ, θ) represents each line that passes by (x_0, y_0). In the $\theta - \rho$ plane, it is represented in a sinusoid curve form. The same situation goes for all the points in an image. If the curves of two different points intersect, that means that both points belong to a same line. A line can be detected by finding the number of intersections between curves. An appropriate threshold of the minimum number of intersections to detect a line can be defined.

The Hough transform in this study is conducted on the platform of Visual Studio 2010 with Open Source Computer Vision (OpenCV) Library 2.4.7.0 with the probabilistic Hough line transform algorithm. The probabilistic Hough line transform is a more efficient implementation

than the standard one in the case that the image contains a few long linear segments (Matas *et al.*, 2000), with the output of extremes of the detected lines (x_0, y_0, x_1, y_1).

Then conduct the Hough transform to the 2D edge image to find the straight lines.

Table 3.3 The parameters in the probabilistic Hough transform

cvHoughLines2	CvSeq* cvHoughLines2 (CvArr* image, void*line_storage, int method, double rho, double theta, int threshold, double param1, double param2);
Method	CV_HOUGH_PROBABILISTIC
Rho	1
Theta	0.2
Threshold	50
Param1	20
Param2	110

In Table 3.3, the rho is the distance resolution of the accumulator in pixels, and the theta is the angle resolution of the accumulator in radians. Threshold is the accumulator threshold parameter (only those lines are returned that get enough votes > threshold). In this experiment, the rho is set to 1 and the theta is set to 0.2. The probabilistic Hough transform is more efficient if the image contains some longer linear segmentation.

For the probabilistic Hough transform, Param1 is the minimum length of the line. For Param2, this parameter represents the maximum interval value (gap) when connecting the broken lines in the same straight line (i.e., when the interval between the two broken line segments on the same

straight line is less than Param2, they will be combined on the same straight line). If the cumulative value is greater than the threshold, then the function returns to the segment.

3.4.3 Power-line Concatenating

As Hough transform can detect multiple lines in a single pass and is limited to the intervals between points during the laser scan, there must be many short line segments instead of a whole line for a long power-line. In this study, in order to concatenate the short power-line segments, a rectangular buffer searching method is proposed, which is conducted by calling the Computational Geometry Algorithms Library (CGAL) in Visual Studio 2010.

At the end of each line segment, extend a rectangular buffer with 4 pixels by 30 pixels to determine whether other segments fall within these two small rectangular areas. If so, it is considered that these segments should be concatenated to be one line. If there is no concatenating relationship among the lines around, then these lines do not belong to a same long line. In this way, the line segments will eventually be classified into their belonging power-line, respectively. The “PointInPolygon” function is used to determine whether or not the point is in the rectangle.

An example of using rectangular buffer searching to concatenate two line segments (Line1 and Line2) is introduced in Figure 3.11. At the end of Line1 and Line2, a rectangle with 4 pixels by 30 pixels is applied, respectively. As the two line segments are close to each other, the rectangular buffers cover both line segments. This is to say that Line1 and Line2 should be classified into the same long line.

In this way, all the short line segments will be classified into 15 power-lines without changing the geometry of short line segments.

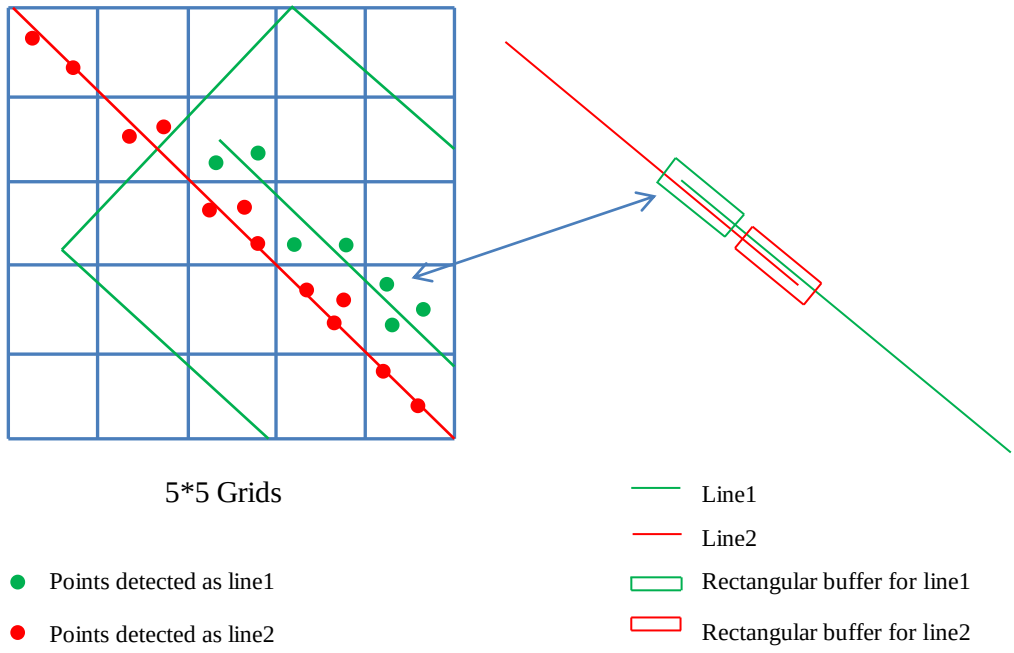

Figure 3.11 An example of rectangular buffer searching in 5 * 5 grids in the raster image

3.4.4 Power-line Points Extraction and Clustering

Based on the row and column numbers of the detected power-lines on the image after detection and concatenating, the corresponding coordinates (x, y) can be calculated. In this way, the XY plane position of the power-lines can be determined, each line in the plane corresponding to one or more power-lines. As for power-lines in different layers in PLG3 and PLG2, when projected to the XY plane, their positions might be overlapped. The 3D coordinates of points on the extracted lines can be determined by searching their x and y coordinates in the point cloud after filtering.

An example of the same points classified into a same line and projected to a grid of 3D point cloud is shown in Figure 3.12. The green points are the points not detected by Hough transform,

so they will not be extracted. In this way, the 3D coordinates will be obtained to the extracted power-line candidate points.

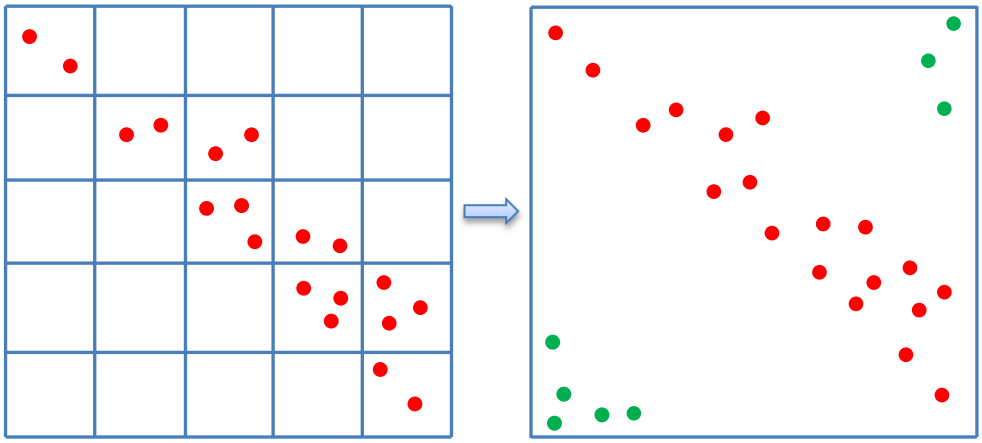

Figure 3.12 Points extraction by projecting to the 3D point cloud after filtering

Then the single power-line clustering is conducted aided with the vertical spacing filtering principle but searching from top to down of the 1 m by 1 m grids in the point cloud and the threshold is 1 m instead of 5 m (Figure 3.13).

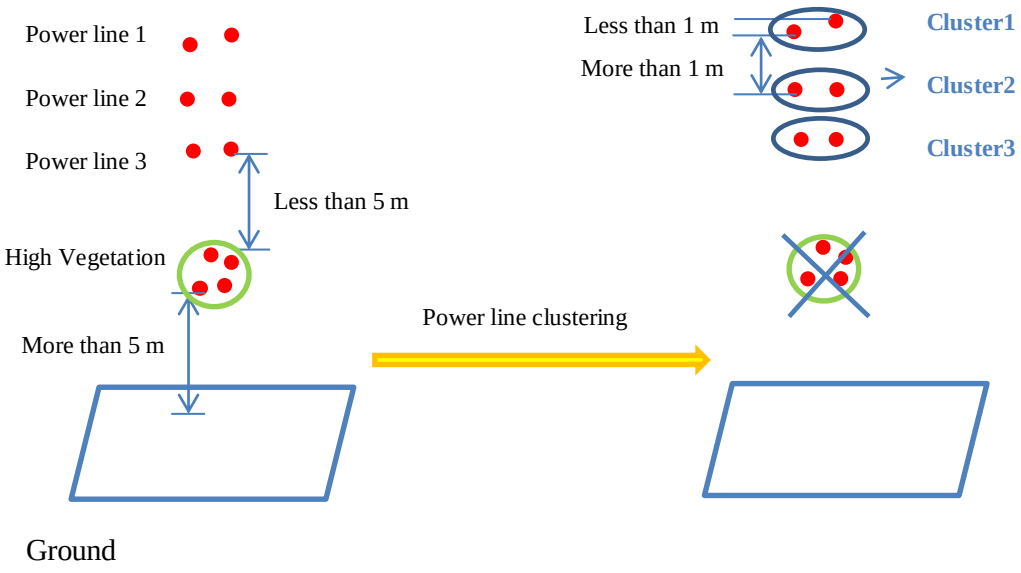

Figure 3.13 Single lines clustering for three-layer power-lines

For the points that belong to the same wire, the height difference is less than 1 m, but more than 1 m with the nearby wires, so these points can be clustered. For the PLG that has three layers like in Figure 3.13, the first three clusters will be kept and the rest of the layers removed; for the one-layer PLG, only the first cluster will be kept. This method can also delete the high vegetation points, which are also detected and extracted by the Hough transform as they are right under the power-lines.

The setting of threshold follows the principle that the power-line points in the same layer will not be clustered into 2 or more layers, but the power-line points not belonging to the same layer will be separated. By measuring the distance between two lines in the vertical direction, 1 m threshold is chosen as it can perfectly separate different layers of power-lines and keep points in the same layer.

3.5 Power-line Curve Fitting and Reconstruction

A 3D power-line can be modeled as a horizontal straight line in XY plane and a vertical catenary curve defined by a hyperbolic cosine function in XZ plane (McLaughlin, 2006; Jwa and Sohn, 2010). In this section, a fitting methodology based on projecting the 3D power-line into the horizontal plane and the vertical plane successively is described.

Before the power-line curve fitting, the wire-connecting point for each span needs to be determined. For a single power-line after clustering, the pylon position should be the highest between two spans. In this study, for a span in a power-line, along the line direction, from one end to the other end, the point with the maximum elevation before and following ten grids (that is, 10 m before and after) will be considered as a wire-connecting point on a pylon.

3.5.1 Fitting in the Horizontal Plane

Referring to the Equation (2.6) in Section 2.3.2, a line can be described in a format of $\rho = x\cos\theta + y\sin\theta$ (2.6) in the XY plane. If (x_i, y_i) is a randomly selected point, then the distance from the point to a line parameterized by

$$\rho_i = \frac{\left| x_i \cos\theta + y_i \sin\theta - \rho \right|}{\sqrt{\cos^2\theta + \sin^2\theta}} = \left| x_i \cos\theta + y_i \sin\theta - \rho \right| \tag{3.2}$$

Assuming there are n ($n \geq 2$) points in total, we aim at minimizing the sum of squares of the orthogonal distances from the points to the estimated line (the residual), the cost function yields

$$J(\theta, \rho) = \sum_{i=1}^{n} (x_i \cos\theta + y_i \sin\theta - \rho)^2 \tag{3.3}$$

A traditional least-squares method by linearizing Equation (3.3) was used when the approximate values of the parameters are given (Jwa and Sohn, 2010). In this study, a total least-squares method is used and solved by a direct method without linearizing, which makes it simpler. By ignoring the correlation of the parameters, Equation (2.6) in a general form

$$x_i\xi_1 + y_i\xi_2 + \xi_3 = 0 \tag{3.4}$$

where $\boldsymbol{\xi}$ is a new 3*1 parameter vector. Consequently, Equation (3.3) gives

$$\min : J(\boldsymbol{\xi}) = \boldsymbol{\xi}^{\mathrm{T}}\boldsymbol{A}^{\mathrm{T}}\boldsymbol{A}\boldsymbol{\xi} \tag{3.5}$$

where $\boldsymbol{A} = \begin{pmatrix} x_1 & y_1 & 1 \\ \vdots & \vdots & \vdots \\ x_n & y_n & 1 \end{pmatrix}$.

Equation (3.5) is a homogeneous optimization problem. A constraint must be exerted to get the solution. A unitary vector is assumed as $\boldsymbol{\xi}^{\mathrm{T}}\boldsymbol{\xi} = 1$. By introducing the Lagrange multiplier λ, the necessary Euler–Lagrange conditions yield

$$2\boldsymbol{A}^{\mathrm{T}}\boldsymbol{A}\boldsymbol{\xi} - 2\lambda\boldsymbol{\xi} = 0 \tag{3.6}$$

It is equal to

$$\boldsymbol{S}\boldsymbol{\xi} = \lambda\boldsymbol{\xi} \tag{3.7}$$

where $\boldsymbol{S} = \boldsymbol{A}^{\mathrm{T}}\boldsymbol{A}$ is called scatter matrix. Equation (3.6) indicates that $\boldsymbol{\xi}$ is the eigenvector of matrix $\boldsymbol{S}$.

To achieve the minimum of Equation (3.5), $\boldsymbol{\xi}$ is the eigenvector corresponding to the smallest eigenvalue. Once $\boldsymbol{\xi}$ is achieved, by investigating Equations (2.6) and (3.4), θ and ρ can be achieved:

$$\begin{aligned} \theta &= \arccos\left(\frac{\xi_1}{\sqrt{\xi_1^2+\xi_2^2}}\right) \\ \rho &= -\frac{\xi_3}{\sqrt{\xi_1^2+\xi_2^2}} \end{aligned} \tag{3.8}$$

When θ and ρ calculated, the line in XY plane can be fitted. The RMSE of the residuals is used to evaluate the accuracy of line fitting in this study. It can be calculated by

$$\mathrm{RMSE} = \sqrt{\frac{\sum_{i=1}^{n}(x_i\cos\theta + y_i\sin\theta - \rho)^2}{n}} \tag{3.9}$$

3.5.2 Fitting in the Vertical Plane

After fitting a power-line in XY plane, a catenary curve in vertical plane will be fitted. Thus, a 2D coordinate transformation has to be transformed in XY plane. Figure 3.14(b) shows the principles of the 2D transformation, in which XOY is the ground plane coordinate system of the point cloud, and $X_sO_sY_s$ is a local coordinate system in a randomly chosen span. The origin of the $X_sO_sY_s$ is located at the start point (usually the wire-connecting point on a pylon) of the span, and the X axis is consistent with the fitted line. Then 2D coordinate system transformation gives

$$\begin{pmatrix} x_s \\ y_s \end{pmatrix} = \begin{pmatrix} \cos\alpha & -\sin\alpha \\ \sin\alpha & \cos\alpha \end{pmatrix} \begin{pmatrix} x - x_0 \\ y - x_0 \end{pmatrix} \tag{3.10}$$

where (x_0, y_0) is the coordinate of the origin of the $X_sO_sY_s$ in the XOY system, and α is the slant angle of the span. Figure 3.12 (a) presents the relationship as follows,

$$\alpha = \frac{\pi}{2} + \theta \tag{3.11}$$

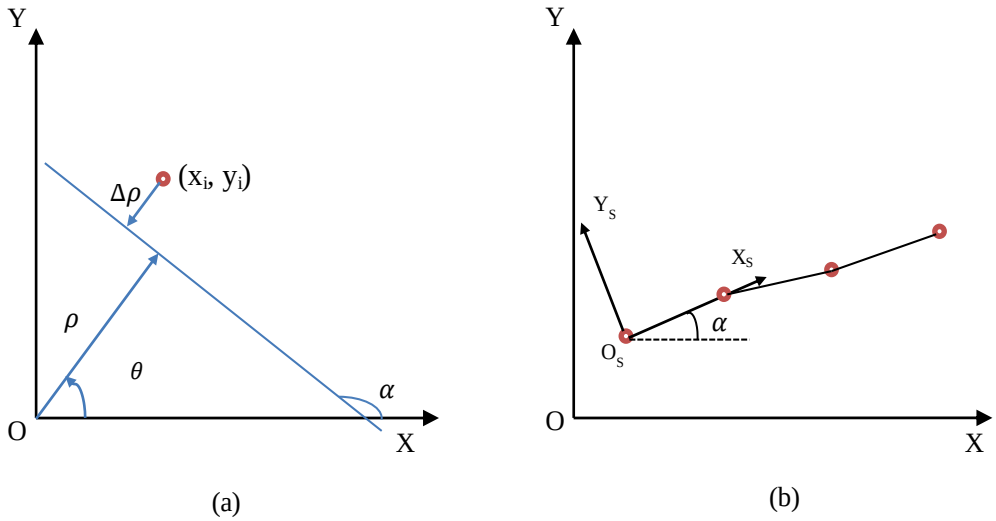

Figure 3.14 2D transformation between ground coordinates (X, Y) and local coordinates (X_s, Y_s) system of each span

A catenary curve *C* (*a*, *b*, *c*) in XZ plane is given by Equation (3.12), where *a* and *b* are the parameters for translation of the origin, and *c* is a scaling factor denoted as the ratio between the tension and the weight of the hanging flexible wire per unit of length (Jwa and Sohn, 2012) (Figure 3.15).

$$z = a + c\cosh(\frac{x-b}{c}) \tag{3.12}$$

The aim of catenary curve reconstruction is to find appropriate parameters *a*, *b*, *c* by giving a group of points. If Equation (3.12) is linearized with respect to the parameters when the initial values of the parameters a_0, b_0, c_0 are given, it leads

$$g_a \delta a + g_b \delta a + g_c \delta c + f = 0 \tag{3.13}$$

where $g_a = \left.\frac{\partial C}{\partial a}\right|_0 = 1; \quad g_b = \left.\frac{\partial C}{\partial b}\right|_0 = -\sinh(\frac{x - b_0}{c_0});$

$$g_c = \left.\frac{\partial C}{\partial c}\right|_0 = \cosh(\frac{x - b_0}{c_0}) - \frac{1}{c_0}\sinh(\frac{x - b_0}{c_0}); \quad f = a_0 + c_0 \cosh(\frac{x - b_0}{c_0}) - z$$

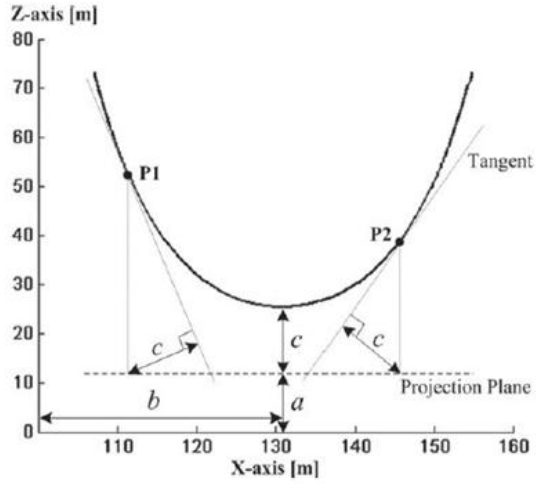

Figure 3.15 An example of catenary curve in the vertical projection

(Source: McLaughlin, 2006)

If there are *m* points ($m \geq 3$), then the parameters can be achieved by minimizing the sum of the squares of the residuals. The corrections of the parameter are the following formulations:

$$\boldsymbol{\delta} = -\left(\boldsymbol{G}^{\mathrm{T}}\boldsymbol{G}\right)\boldsymbol{G}^{\mathrm{T}}\boldsymbol{f} \tag{3.14}$$

where $\boldsymbol{G} = \begin{pmatrix} g_a^{(1)} & g_b^{(1)} & g_c^{(1)} \\ \vdots & \vdots & \vdots \\ g_a^{(m)} & g_b^{(m)} & g_c^{(m)} \end{pmatrix}; \boldsymbol{f} = \begin{pmatrix} f^{(1)} \\ \vdots \\ f^{(m)} \end{pmatrix}; \boldsymbol{\delta} = \begin{pmatrix} \delta a \\ \delta b \\ \delta c \end{pmatrix}$ (the super script $^{(i)}$ denotes the corresponding values of point i).

The best estimates can be acquired by updating the parameters iteratively until the corrections are small enough. To guarantee the convergence, the initial values must be correctly chosen. The first point, the end point and the middle point of each span can be chosen to get the proper initial approximations. And the RMSE of the residuals can be used to evaluate the accuracy according to Equations (3.9) and (3.12).

3.5.3 Accuracy Assessment

Positional accuracy and thematic accuracy are commonly used in the accuracy assessment. Positional accuracy reflects the accuracy of the location and measures the spatial feature from its true or reference location on the ground (Bolstad, 2005). Thematic accuracy reflects the attribute of features of the results (Congalton and Green, 2008).

In this study, power-line fitting and 3D modeling results are assessed by both the thematic and positional accuracy assessment, quantitatively and qualitatively. The thematic accuracy assessment is most commonly used to check the power-line extraction quality. Reference data is the power-line points manually selected from the raw airborne LiDAR data using ArcGIS. Two criteria are used to measure the accuracy in this study: completeness and correctness (Jwa and Sohn, 2012). True positives (TP), true negatives (TN), false negatives (FN) and false positives (FP) are counted. The TP and TN is the number of power-line points and non-power-line points

that are commonly found in both the reference and the result, respectively. The FN and FP is the number of power-line points that are found only in the reference and the result, respectively.

Completeness (omission error, producer's accuracy) is obtained by

$$\text{Completeness} = \frac{TP}{TP+FN} \tag{3.15}$$

Correctness (commission error, user's accuracy) is obtained by

$$\text{Correctness} = \frac{TP}{TP+FP} \tag{3.16}$$

In addition, the positional accuracy relies on the RMSE, which is the square root of the average squared differences between the fitted lines and the extracted points. For thematic accuracy assessment, a qualitative visual check is being applied for the extracted power-line point.

3.5.4 A Case Study on Hazard Tree Detection

Hazard tree detection is an application of the 3D reconstruction in this study, which can be conducted along with the workflow. The purpose of hazard tree detection is to find the minimum distance between the power-line point and non-power-line point in one grid.

When doing the vertical spacing filtering, the maximum elevations of the removed points need to be recorded for each grid, as do the maximum elevations of the non-power-line points. For those girds remaining, record the maximum elevations of all the points in the grid.

For the surrounding trees, which belong to the girds having both power-line points and non-power-line points, not only calculate the distance between power-line point and maximum non-power-line point in a grid, but also calculate the distance among power-line point in that grid and the maximum non-power-line points in the 8-neighbours.

3.6 Chapter Summary

This chapter introduces a successive 3D power-line reconstruction workflow. An improved filtering method “density-based filtering” is proposed, focusing on the situation of point cloud with dense vegetation around the power-line corridor. Probabilistic Hough transform is conducted to detect and extract power-lines. The clustered power-lines are fitted in horizontal and vertical planes. Finally, the workflow offers a hazard tree detection approach in the management of corridor.

Chapter 4 Results and Discussion

This chapter is divided into five main sections. Section 4.1 offers the results and discussion of filtering processes carried out through vertical spacing filtering and density-based filtering. Section 4.2 presents the results and discussion of the power-line detection and extraction. Section 4.3 shows the results and discussion of power-line fitting and 3D modeling. Section 4.4 presents the results and discussion of accuracy assessment. Finally, Section 4.5 presents a case study on the corridor management about hazard tree detection.

4.1 Filtering

In this study, the proposed filtering method has been divided into two steps: vertical spacing filtering followed by density-based filtering. Figure 4.1 shows different angles of views of the raw airborne LiDAR point cloud with 850,117 points in the area of 170,000 m^2. This image represents, in dark blue, the lower elevation values that usually correspond to the Westwood Lake at the Northeast of the study area according to the compass on the upper right corner; and in light blue, low vegetation and power-lines. The image represents, from green to red, the higher elevation values that represent higher vegetation.

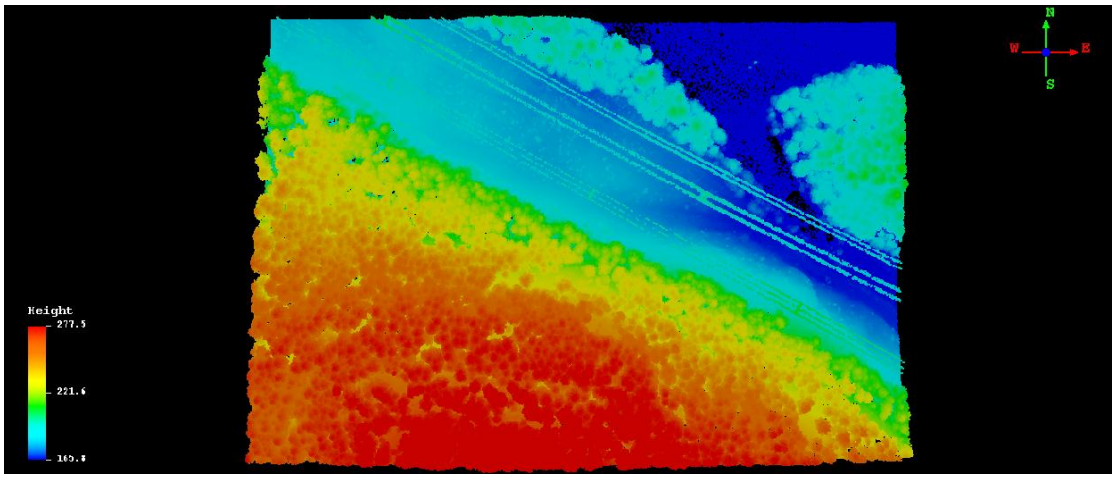

(a) Top view

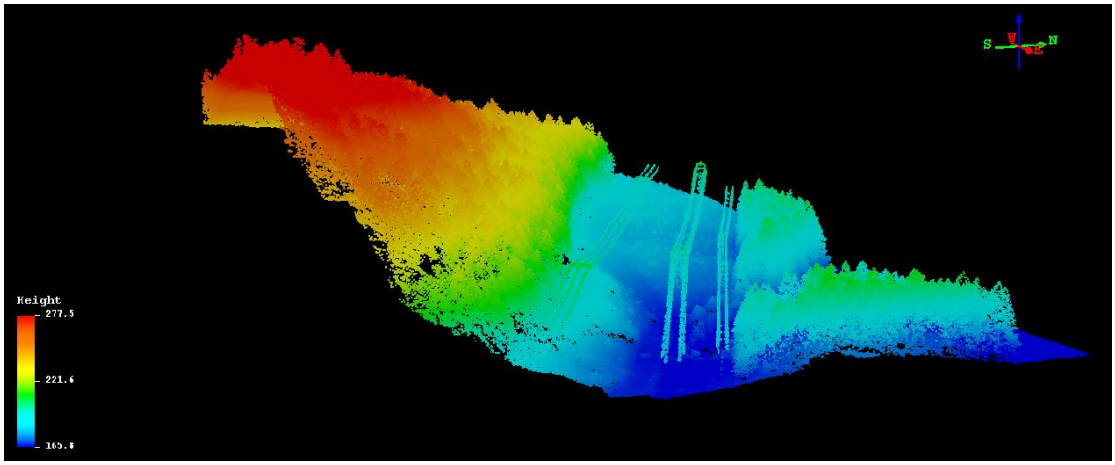

(b) Oblique view from one end of the dataset

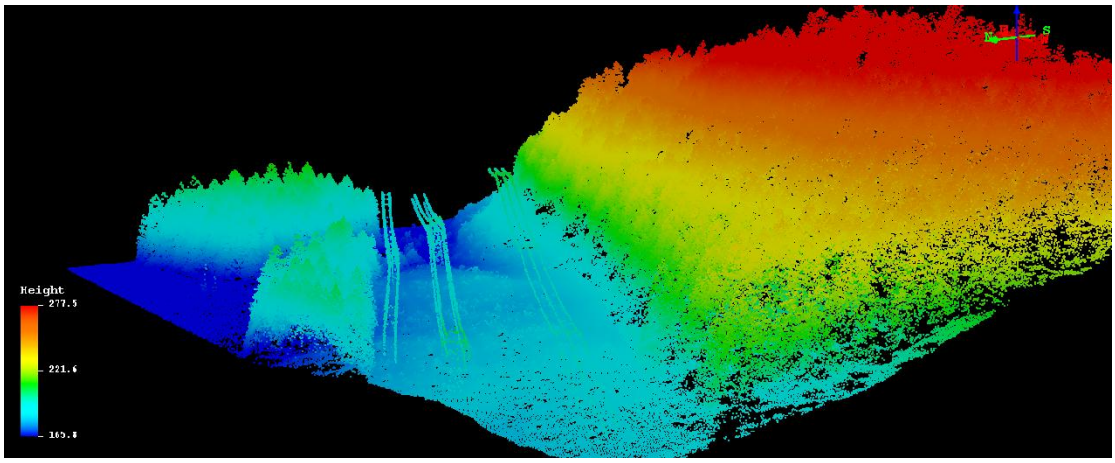

(c) Oblique view from the other end of the dataset

Figure 4.1 Raw airborne LiDAR point cloud

4.1.1 8-neighbours Culling Mechanism

Before using the 8-neighbours culling mechanism, the ground points are extracted in this study by lastools. In this study, the 8-neighbours culling mechanism is first used after removing the ground points. The result shows that most of the points are removed after filtering, even the majority of points belonging to power-lines (Figure 4.2).

The reason for the poor result is that the power corridor is surrounded by low bushes. Echoes received within the regarded “power-line grid” of 8-neighbours came from not only the ground, but also from the low bushes. In this way, the 8-neighbours culling mechanism is designed to work with different thresholds to remove the points above ground (Figure 4.3).

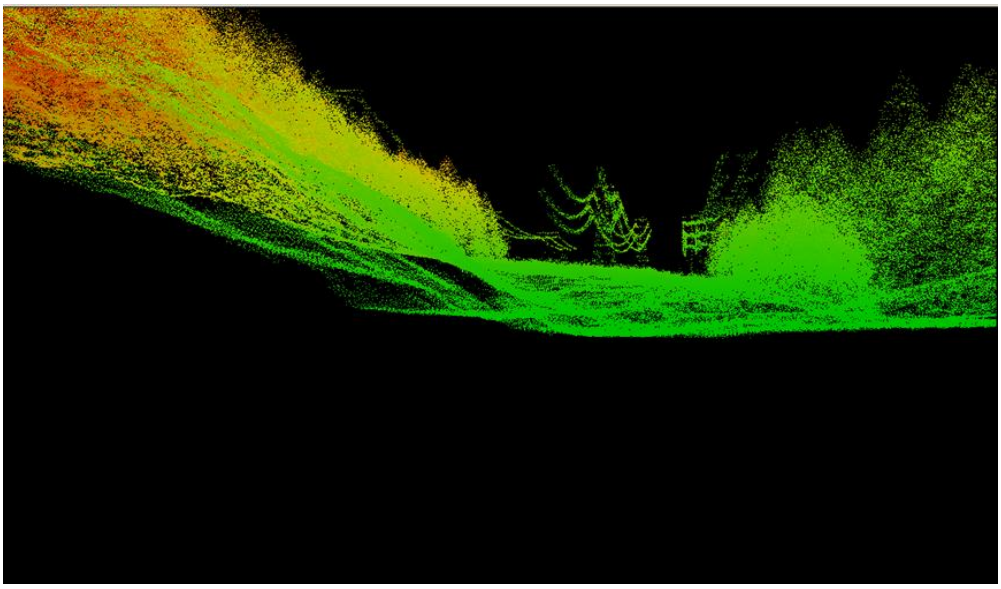

(a) Before 8-neighbours Culling mechanism

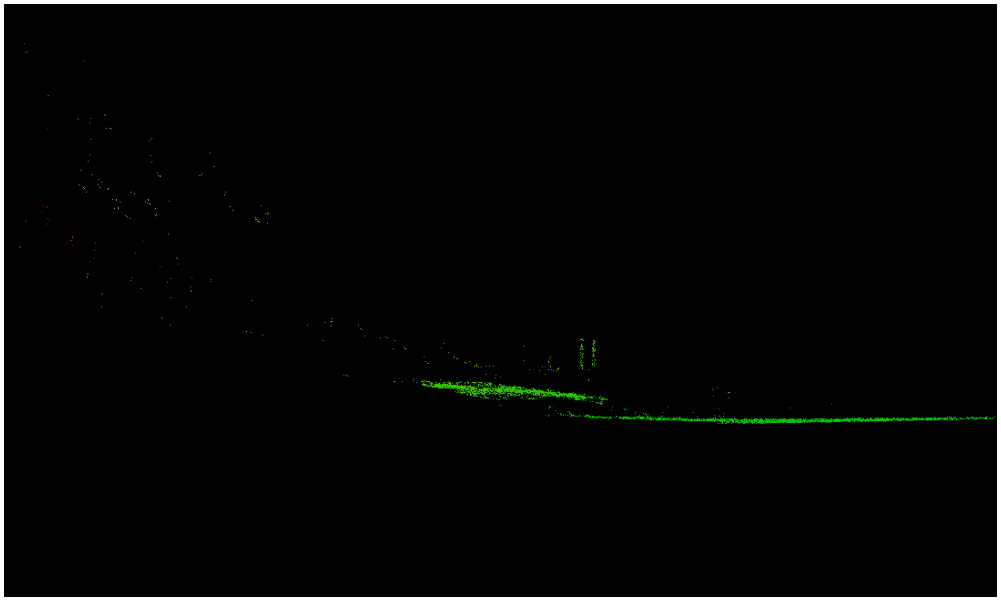

(b) After 8-neighbours Culling Mechanism

Figure 4.2 Front view of the result using 8-neighbours culling mechanism after removing ground points

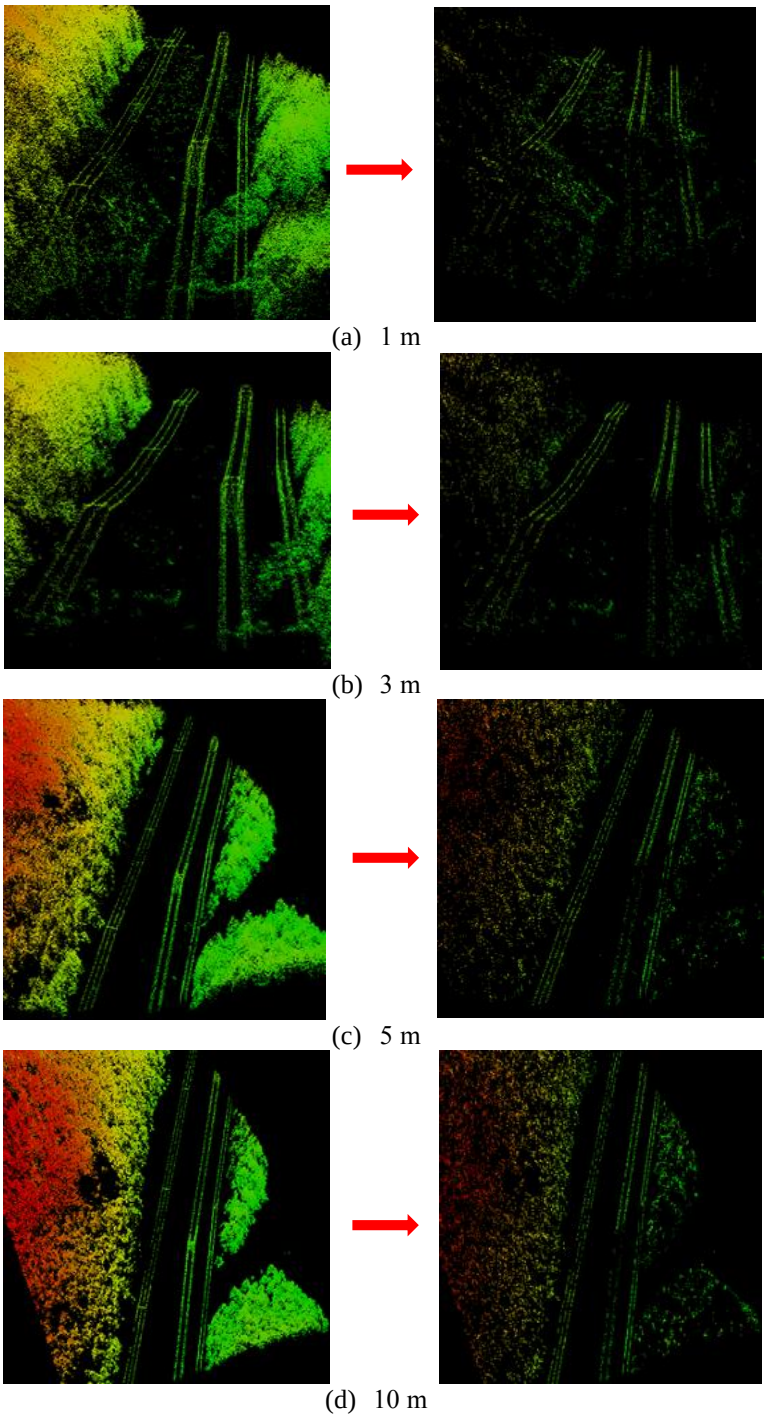

(a) 1 m

(b) 3 m

(c) 5 m

(d) 10 m

Figure 4.3 8-neighbours culling mechanism results before and after removing points above ground with different thresholds

The left image in Figure 4.3 (a) shows the result of filtering points under 1 m. With the remaining points after the 8-neighbours culling mechanism, as shown by the right image in Figure 4.3 (a), the lower half part of PLG2 and PLG3 on the image lost a lot of points, and many non-power-line points are kept. This indicates that the threshold of 1 m is not enough to remove the vegetation under power-lines. For a better result for the culling mechanism, the threshold is set at 3 m, 5 m and 10 m, and the results are shown in Figures 4.3 (b), (c), and (d), respectively. Comparing the results of filtering with different thresholds, since 3 m remains vegetation points under power-lines and 10 m filtering some power-line points, 5 m is the optimum threshold for the 8-neighbours culling mechanism. However, the result with 5 m is still not satisfactory as the remaining points belonging to power-lines are sparse.

4.1.2 Vertical Spacing Filtering

As the results of 8-neighbours culling mechanism are not satisfactory, a density-based filtering is conducted by enlarging the searching range of neighbours in this study.

Figure 4.4 shows different angles of views of the point cloud after vertical spacing filtering with 709,591 points. Comparing Figures 4.1(b) with 4.4 (b), and 4.1 (c) with 4.4 (c), it clearly presents that points on the ground under power-lines in vertical plane have been filtered out. Some low vegetation near the ground has been removed. All together 140,526 points, about 16.53% of the sum are eliminated at this step.

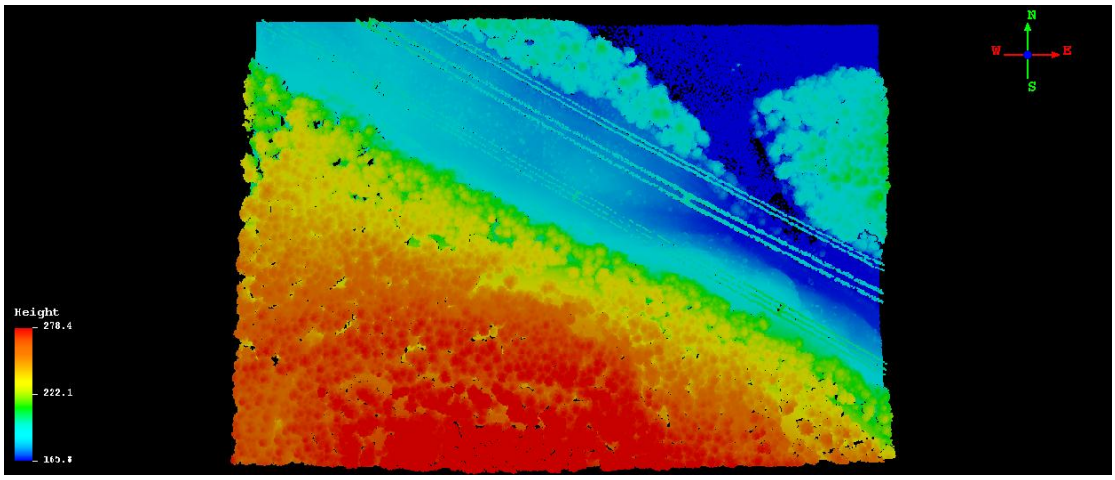

(a) Top view

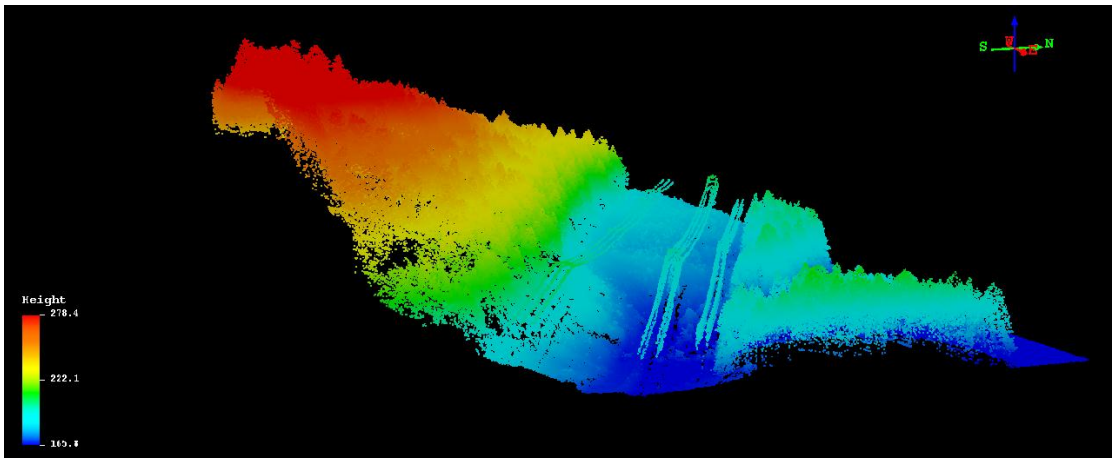

(b) Oblique view from one end of the dataset

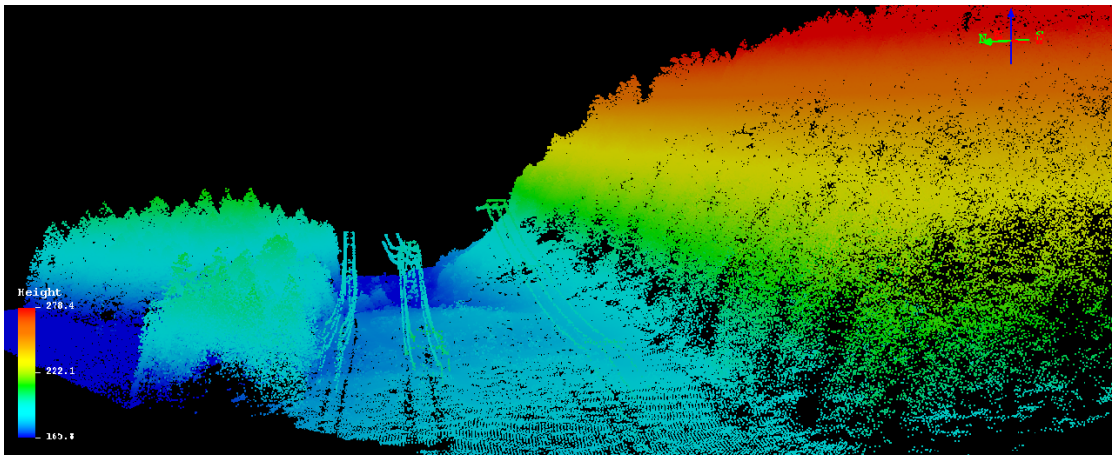

(c) Oblique view from the other end of the dataset

Figure 4.4 Result of vertical spacing filtering

4.1.3 Density-based Filtering

The threshold setting of the density-based filtering algorithm is a vital step in the whole process. After the first step, comparing Figures 4.4 with 4.5, it is obvious that the ground points have been removed. Dense points belonging to the lake and vegetation are thinned. Power-line candidate points within the corridor area have remained. Three different views of Figure 4.5 clearly indicate that power-line candidate points are in higher density compared with the sparse vegetation and lake points.

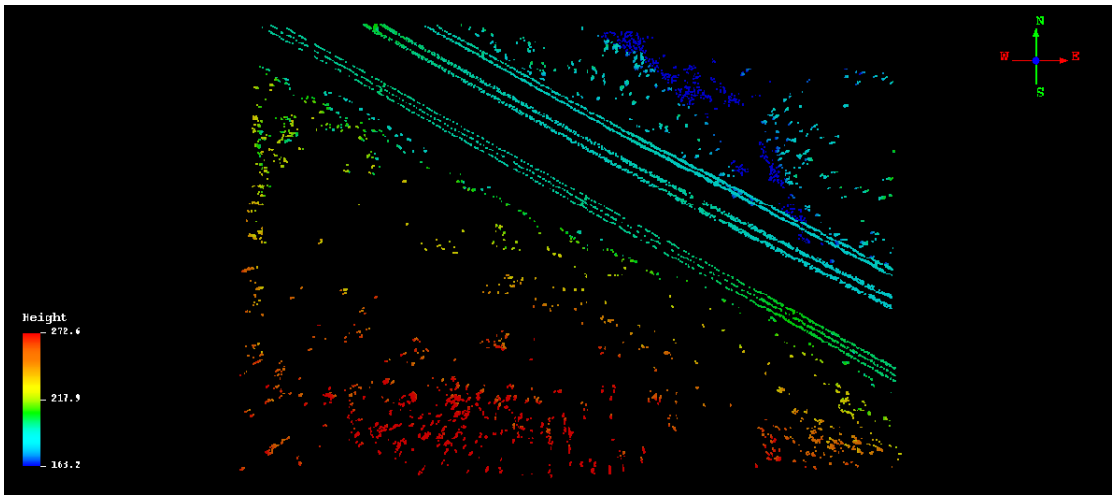

(a) Top view

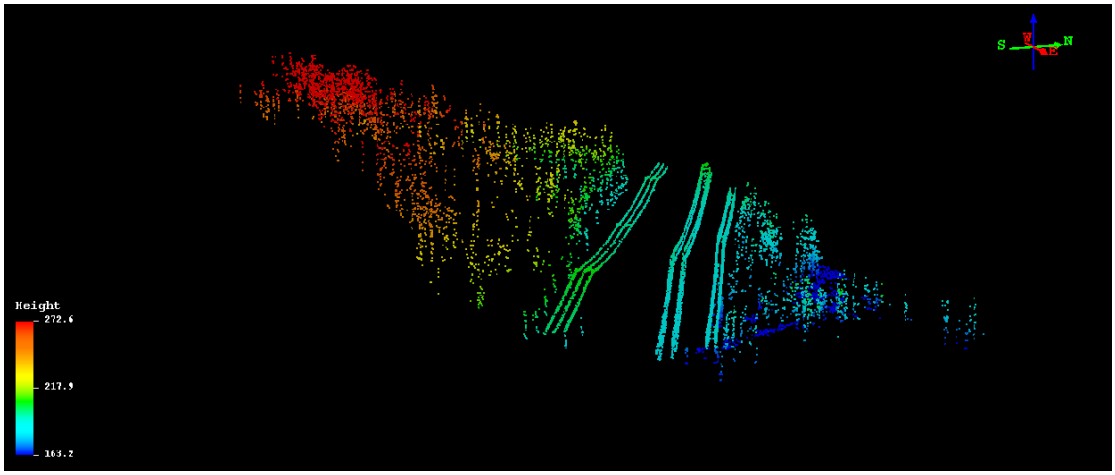

(b) Oblique view from one end of the dataset

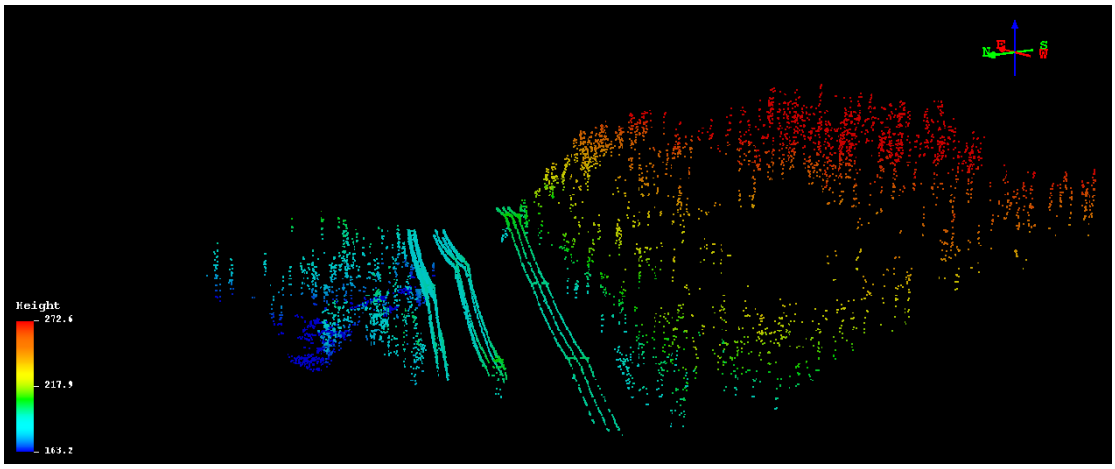

(c) Oblique view from the other end of the dataset

Figure 4.5 Result of density-based filtering

Figure 4.5 shows the result of point cloud after density-based filtering with 13,430 points in different angles of views. By comparing with the point cloud kept after vertical spacing filtering, 696,161 points, about 98.11% points are removed. After the completion of filtering, 836,687 points, about 98.42% of the total points in the raw point cloud are removed at this step. By experimenting, the density-based filtering proposed in this study is better than the 8-neighbours culling mechanism as it keeps more power-line points, especially on PLG2 and PLG3 shown by ovals (Figure 4.6).

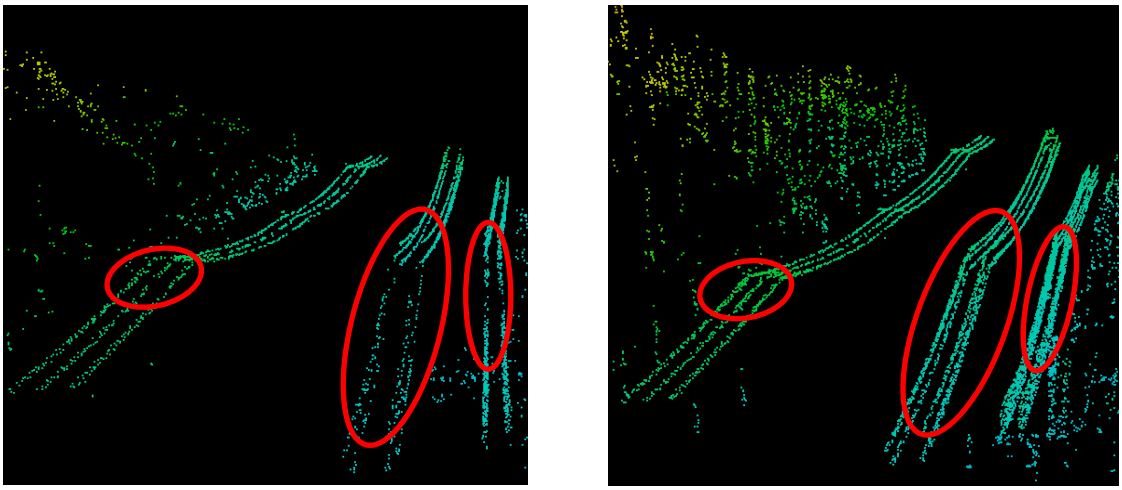

(a) 8-neighbours culling mechanism (b) density-based filtering

Figure 4.6 Comparison of results after 8-neighbours culling mechanism and density-based filtering

4.2 Power-line Detection and Extraction

This section encompasses four parts. The first part involves the results of detecting the power-line candidate points from probabilistic Hough transform. The second part describes the results of concatenated power-line segments. The third part shows the extracted power-line candidate points. The fourth part presents the single power-line clustering results for each power-line group.

4.2.1 Probabilistic Hough Transform

The result of density-based filtering is used for the following processing. The power-line candidate points are detected with straight lines by probabilistic Hough transform with tests of different thresholds (Figure 4.7). The results of power-line segments are shown in chromatic colours with a group of test thresholds (Figure 4.7 (a)) and red colour with appropriate thresholds (Figure 4.7 (b)).

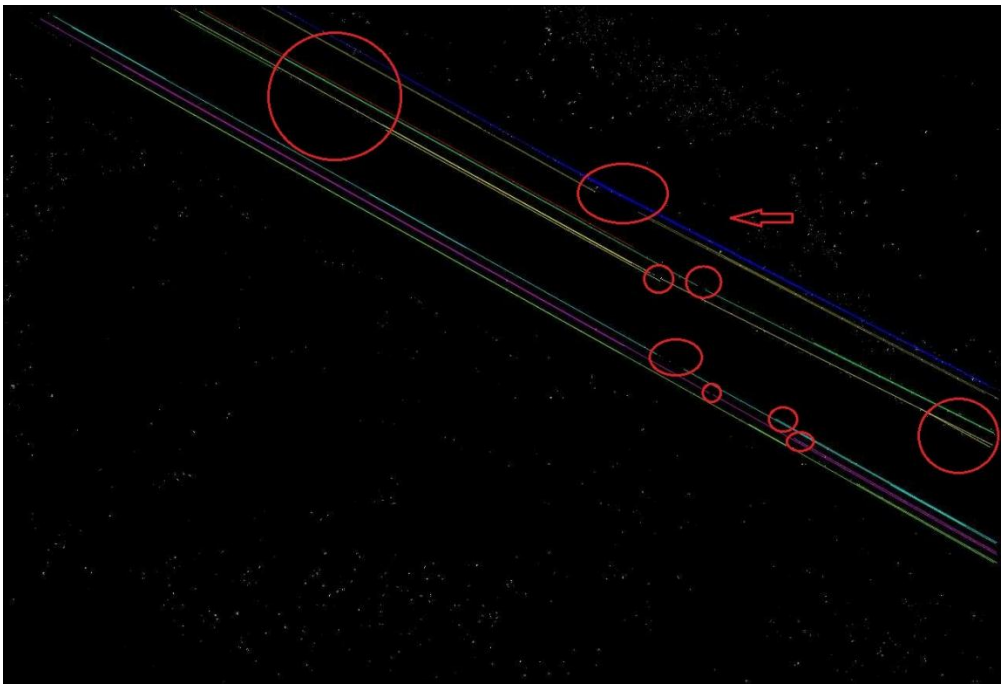

(a) Result of a group of test thresholds: rho-2, Param2-100

(b) Result of appropriate thresholds: rho-1, Param2-110

Figure 4.7 Result of power-line segments detected by Hough transform

By visual examination, three groups of power-lines cross the image in an unconnected manner in the projected XY plane. The result with appropriate thresholds is better in visual check, but there are still problems of power-line segments overlapping.

For PLG1, as it only has one layer with three lines, it is much easier to detect the location of lines according the filtered points. For PLG2 and PLG3, the projection of PLG2 contains 4 lines, while PLG3 contains 2 lines, which makes the PLG3 different from PLG 2 even though they share the structure of 6 lines between two pylons. PLG2 is harder to detect and extract as the distance between the projected lines are relatively narrower. The detected 9 power-lines are not distinguished at this stage (Figure 4.7(b)).

4.2.2 Concatenated Power-line Segments

Figure 4.8 indicates the result of concatenated power-line segments and is distinguished with 9 colors. A rectangle (4 pixels by 30 pixels) is a buffer zone to detect the lines which belong to the same long line. Numbers near short lines are generated along with the probabilistic Hough transform function in OpenCV in the order of the detection. Compared to the power-lines before concatenate, the discontinuous lines are classified based on distance. Based on the concatenated power-lines, the x and y coordinate are known and all the points with the same x and y coordinates in the point cloud are extracted.

PLG2 is supposed to contain 4 long lines. In this result, the grey line and purple line are too thin to detect. The grey line and purple line are in the second layer, which has a relatively short distance from the first and third layer. But this does not affect the extraction of power-line segment points and clustering.

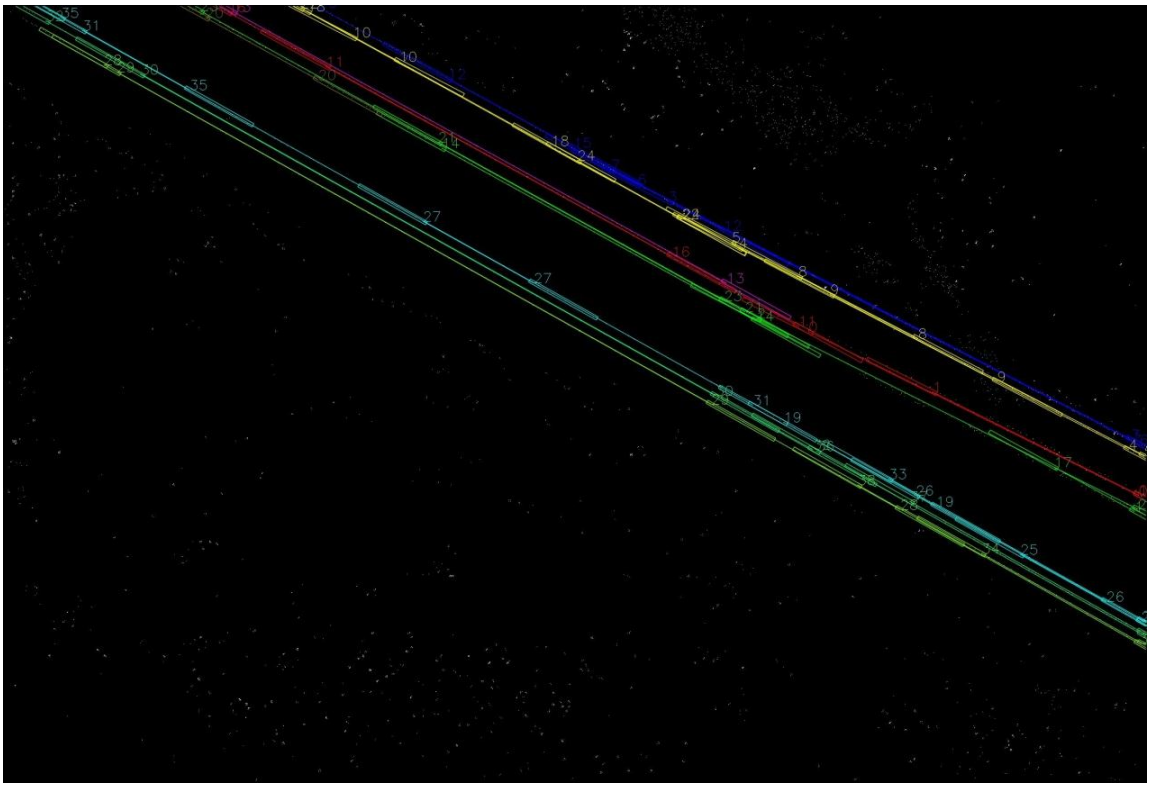

Figure 4.8 Result of concatenated power-line segments

4.2.3 Extracted Power-line Candidate Points

Figure 4.9 indicates the extracted power-line candidate points in different angles of views. From the top view of the point cloud, the remaining points only contain the power-line corridor points in the vertical space (Figure 4.9 (a)). From an oblique view of the point cloud, points of layer 2 of PLG2 are well kept (Figure 4.9 (b)). However, some points which are non-power-lines points right under the power-lines have also been extracted.

The non-power-line points are vegetation points in corridor. These are points left from the first step – vertical spacing filtering. The threshold of vertical spacing filtering is 5 m, which indicates the distance between the lowest point in the third layer and the highest point of the vegetation

below is less than 5 m. As for the default setting, these points are considered to be the power-line points and remained. They are regarded as the potential hazard trees (Figure 4.9 (c)).

During the extracting, points within the 1 m by 1 m grid will be considered as power-line points, when searching power-line points along the red long line. Every line detected by Hough transform is 0.2 m pixel, so the 4 lines of PLG2 are classified into 2 groups to conduct the following processing. The result of the concatenating for PLG2 will not affect the later results. In this way, the following clustering to process the power-line structures like PLG2 and PLG3 are the same.

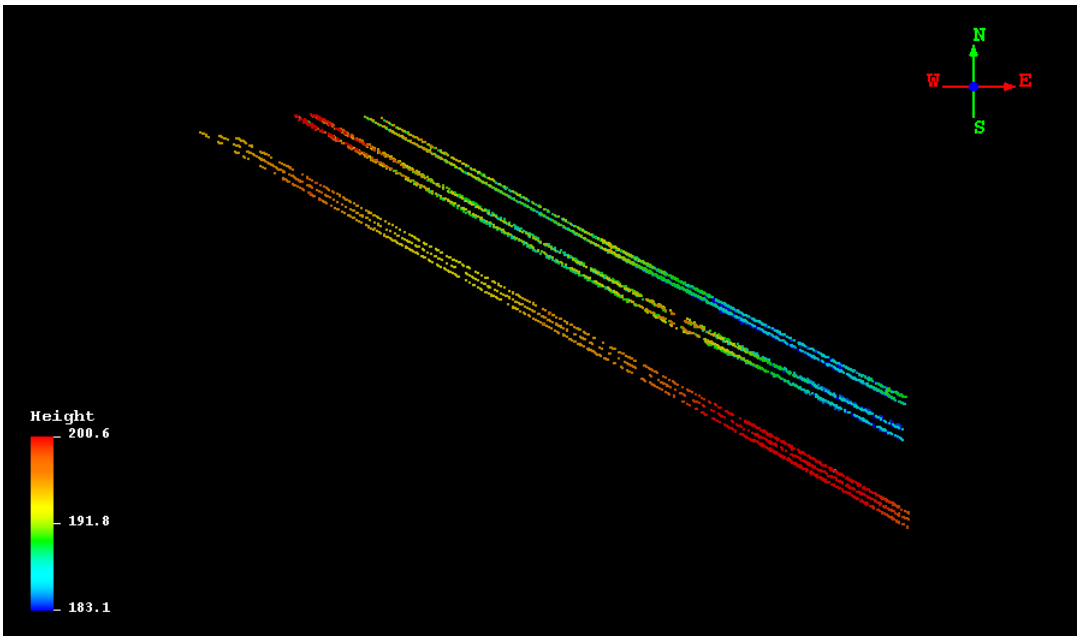

(a) Top view

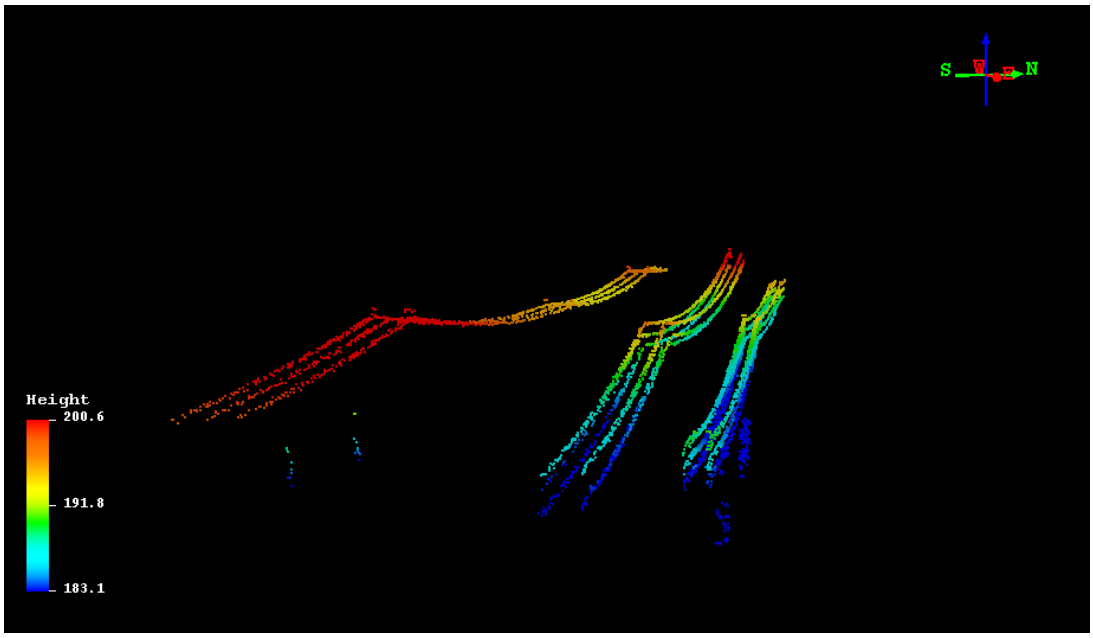

(b) Oblique view from one end of the dataset

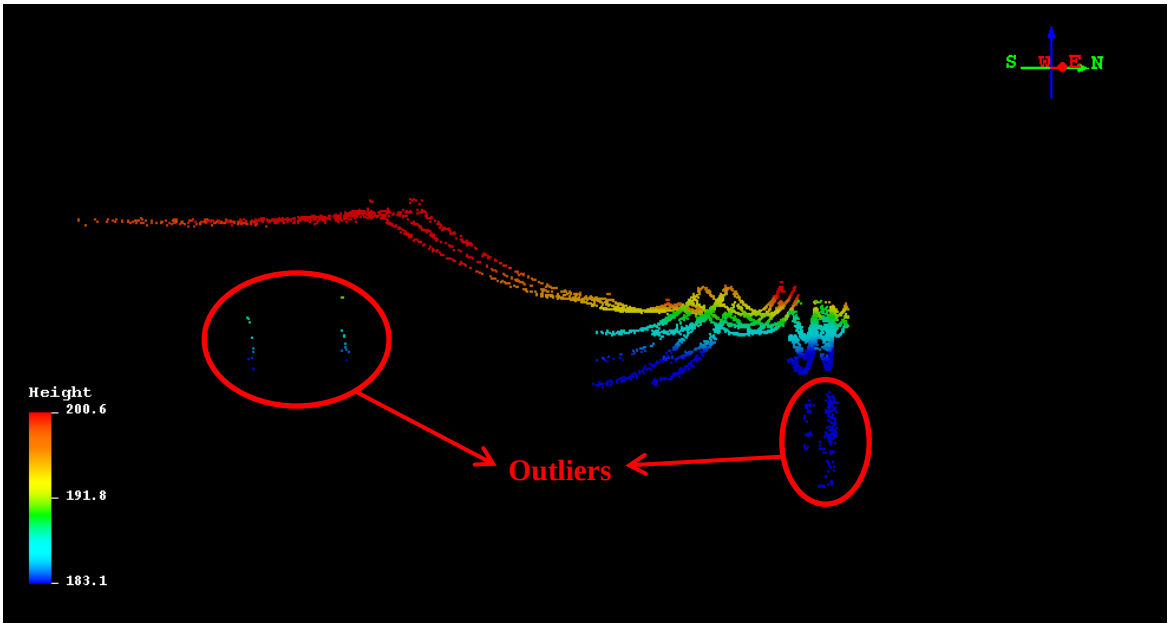

(c) Mis-extracted points are shown by ovals

Figure 4.9 Result of extracted power-line candidate points

4.2.4 Clustered Power-line Points

Figure 4.10 shows the clustered power-lines in three groups separately with ArcGIS 10.1. The incorrectly extracted power-line candidate points have been removed. Each PLG is presented both in side view and oblique view. The power-lines are well clustered and each line can be distinguished separately.

Vegetation points in the power-line candidate points are removed. For PLG2 and PLG3, the first three clusters will be kept and the rest of the layers removed; for PLG1, only the first cluster kept.

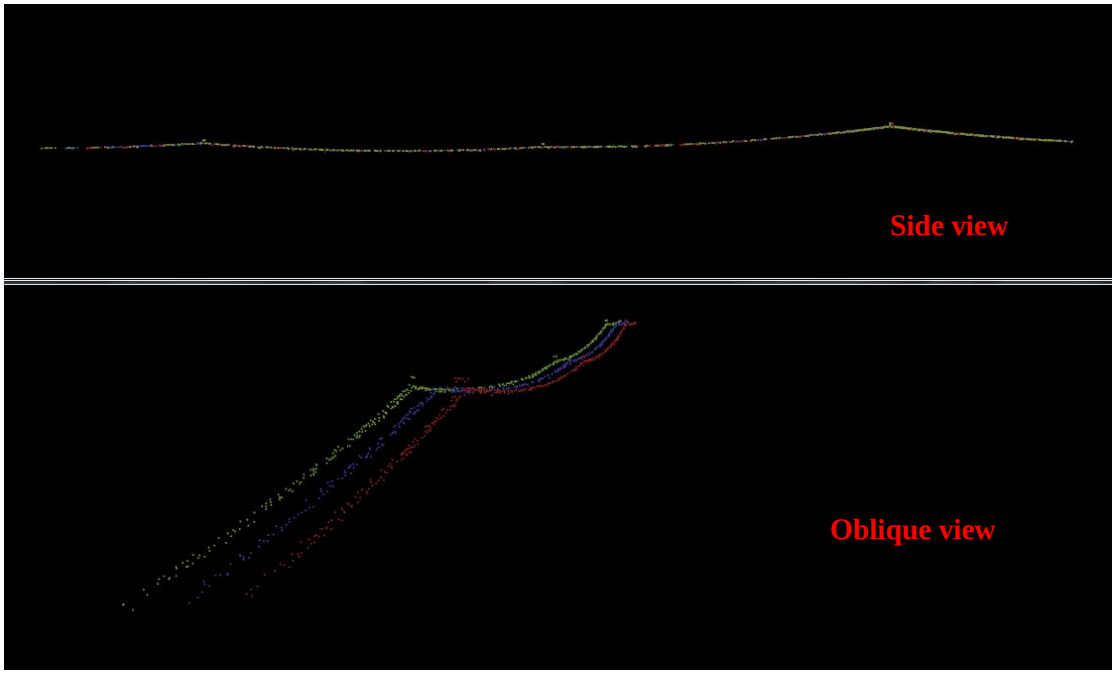

(a) A side view and oblique view of PLG1 after clustering

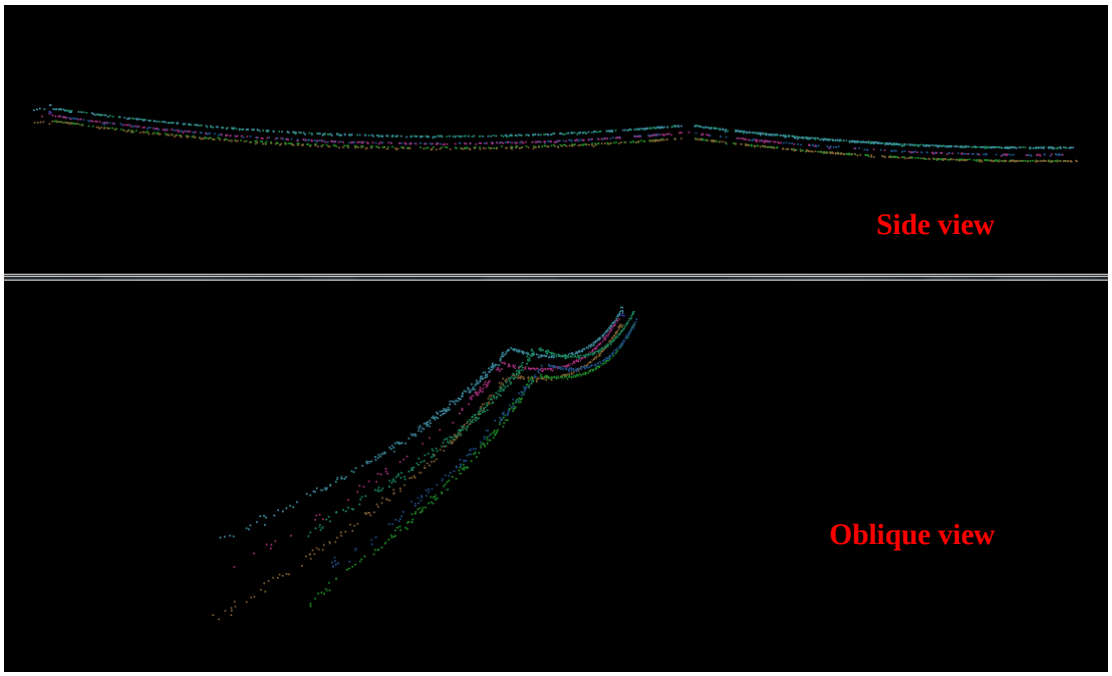

(b) A side view and oblique view of PLG2 after clustering

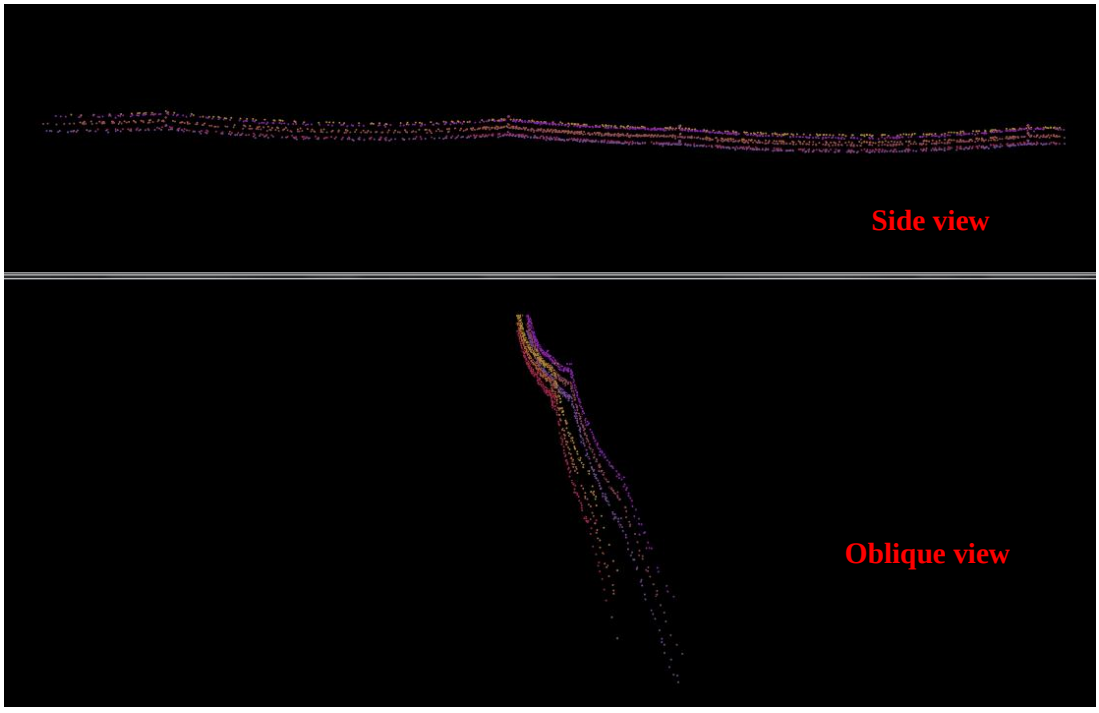

(c) A side view and oblique view of PLG3 after clustering

Figure 4.10 Results of three groups of power-lines clustering

In Table 4.1, the number of each power-line is presented where power-lines stretch in the study area about 500 m. As the sampling frequency varies during the data collecting period, the point number varies. In this process, 5,726 points are kept. 226 points are incorrectly extracted, as they are right under the power-lines.

Table 4.1 Points within each clustered PLG

PLG1	Num	PLG2	Num	PLG3	Num	Others Num	Total
Power-line 1	472	Power-line 4	389	Power-line 10	445	226	5726
Power-line 2	405	Power-line 5	223	Power-line 11	459		
Power-line 3	430	Power-line 6	317	Power-line 12	431		
		Power-line 7	368	Power-line 13	312		
		Power-line 8	296	Power-line 14	310		
		Power-line 9	341	Power-line 15	302		

4.3 Power-line Fitting and 3D Modeling

In this section, all the 15 power-lines of the 3 PLGs are fitted in XY and XZ planes and modeled in 3D space. The XZ plane here is actually $X_S Z$ plane, where X_S is not the same X, but X of the local coordinate system in a randomly chosen span. As 15 power-lines are too many to display and wires within each group share similar properties of fitting and modeling, a representative of the first power-line of each PLG is presented below. Finally, a 3D scene of the reconstructed power-lines is shown.

4.3.1 Power-line 1 in PLG1

For Power-line 1, the results of fitting on XY and XZ planes are displayed in Figure 4.11 and 4.12, respectively. The green points are the concatenating points between two adjacent spans, which are the detected pylon points, and the blue line is the fitted line.

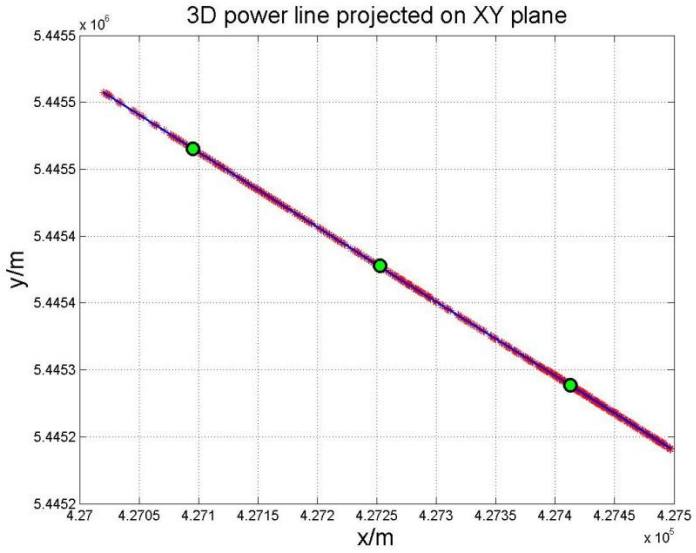

Figure 4.11 Result of Power-line 1 fitting on XY plane

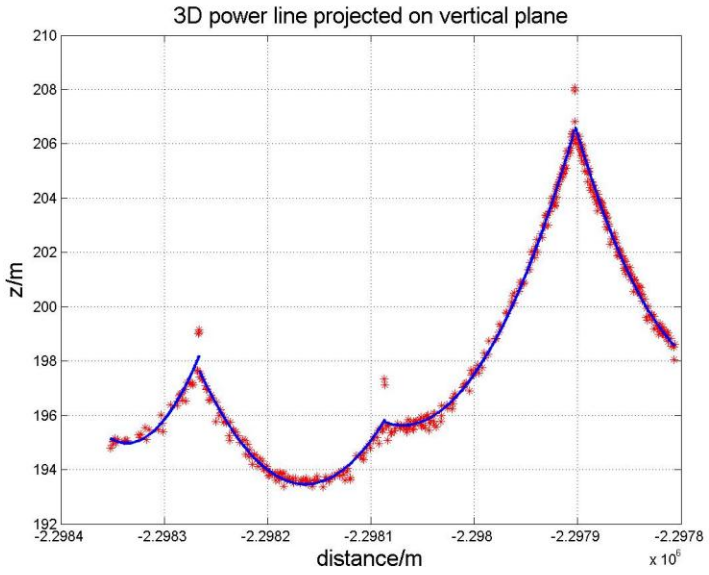

Figure 4.12 Result of Power-line 1 fitting on XZ plane

Table 4.2 Fitted spans in XY plane of Power-line 1

No.	Counts of points	θ(rad)	ρ(m)
1-1	39	1.058243	4955146.199
1-2	122	1.061281	4962105.638
1-3	156	1.065402	4971471.524
1-4	155	1.057733	4953975.235

Table 4.2 shows the parameters for the 4 spans (1-1, 1-2, 1-3, and 1-4) of Power-line 1. As mentioned in $\rho = x\cos\theta + y\sin\theta$ (2.6), the functions can be estimated in the XY plane for each span. Table 4.3 shows the results of parameters of power-line function $z = a + c\cosh(\frac{x-b}{c})$ (3.12).

Table 4.3 Fitted spans in XZ plane of Power-line 1

No.	Counts of points	a	b	c
1-1	39	-563.128	-2298336.068	758.101
1-2	122	-1062.807	-2298163.540	1256.266
1-3	156	-1082.015	-2298069.380	1277.644
1-4	155	-886.908	-2297763.756	1084.645

Based on the fitting on horizontal and vertical space, the Power-line 1 is reconstructed and shown in Figure 4.13.

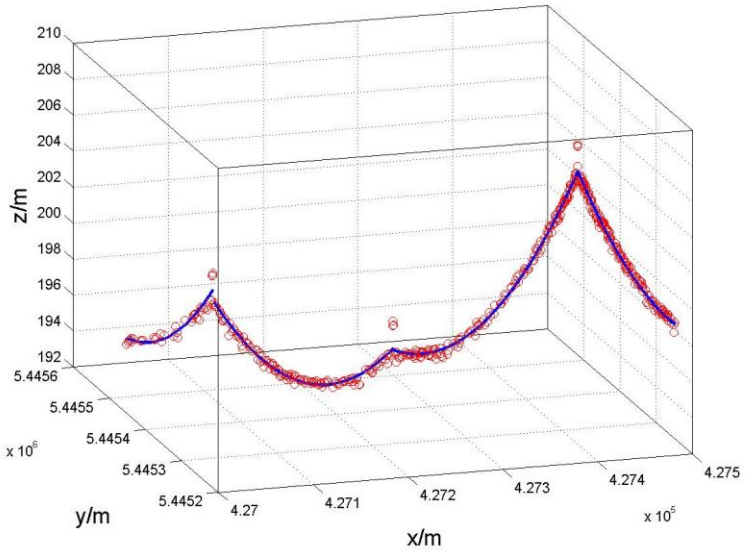

Figure 4.13 Result of 3D reconstruction of Power-line 1

4.3.2 Power-line 4 in PLG2

For Power-line 4, the results of fitting on XY and XZ planes are displayed in Figures 4.14 and 4.15, respectively.

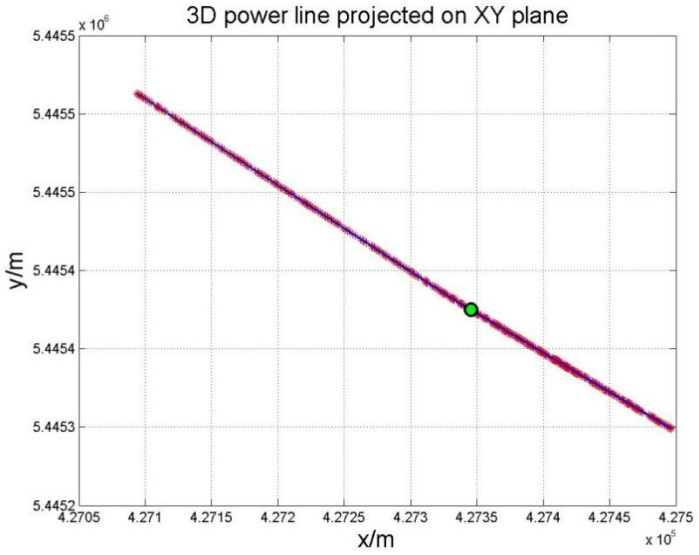

Figure 4.14 Result of Power-line 4 fitting on XY plane

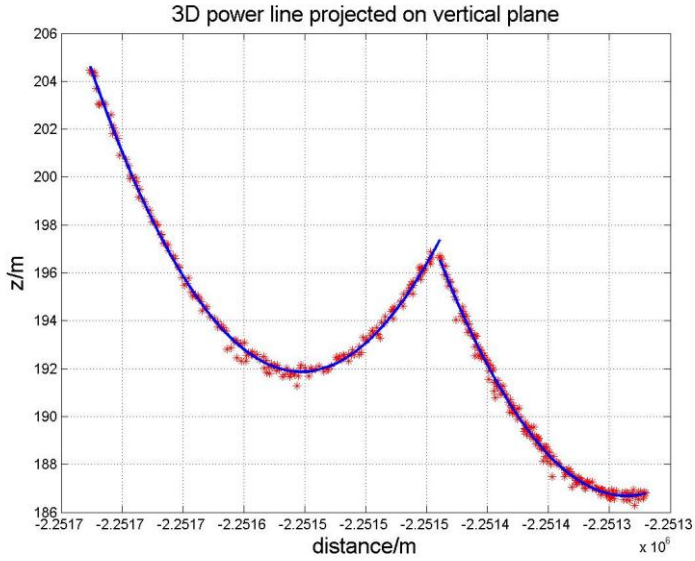

Figure 4.15 Result of Power-line 4 fitting on XZ plane

Table 4.4 shows the parameters of the 2 spans of Power-line 4. Table 4.5 shows the results of parameters of power-line function for each span in vertical space.

Table 4.4 Fitted spans in XY plane of Power-line 4

No.	Counts of points	θ/rad	ρ/m
4-1	180	1.067620	4976519.871
4-2	203	1.104910	5056996.583

Table 4.5 Fitted spans in XZ plane of Power-line 4

No.	Counts of points	a	b	c
4-1	180	-985.307	-2251553.017	1177.172
4-2	203	-1001.830	-2251286.190	1188.512

Based on the fitting on horizontal and vertical space, the Power-line 4 is reconstructed and shown in Figure 4.16.

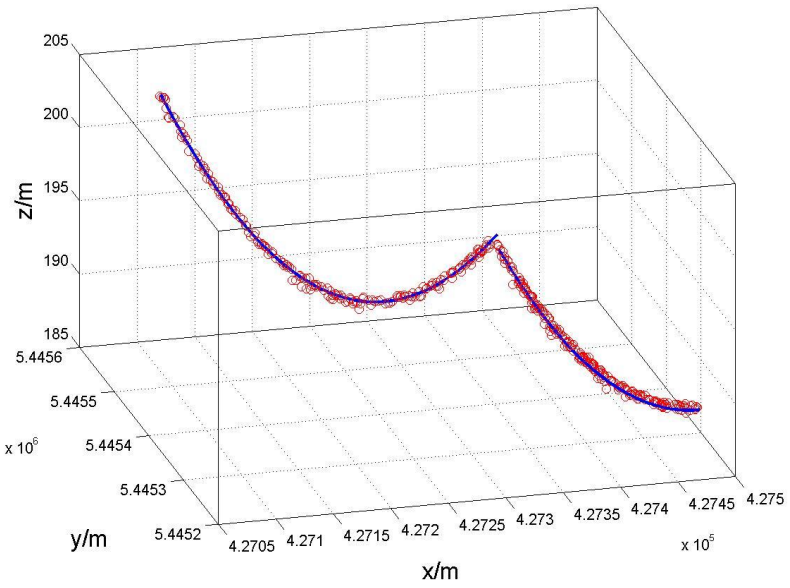

Figure 4.16 Result of 3D reconstruction of Power-line 4

4.3.3 Power-line 10 in PLG3

For Power-line 10, the results of fitting on XY and XZ planes are displayed in Figures 4.17 and 4.18, respectively.

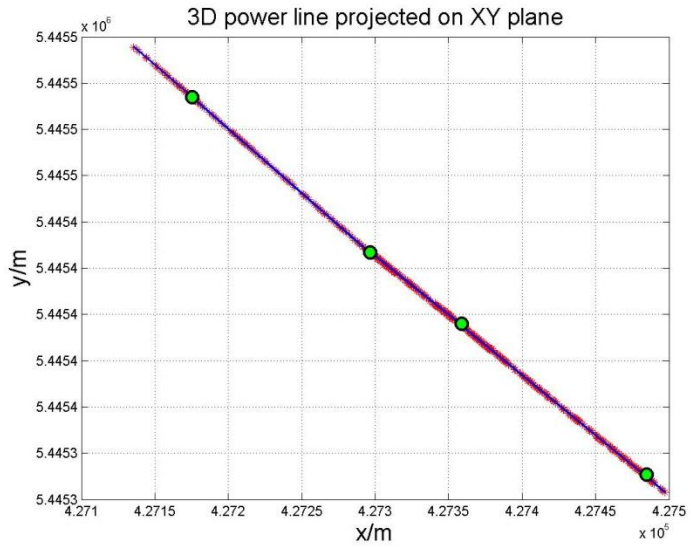

Figure 4.17 Result of Power-line 10 fitting on XY plane

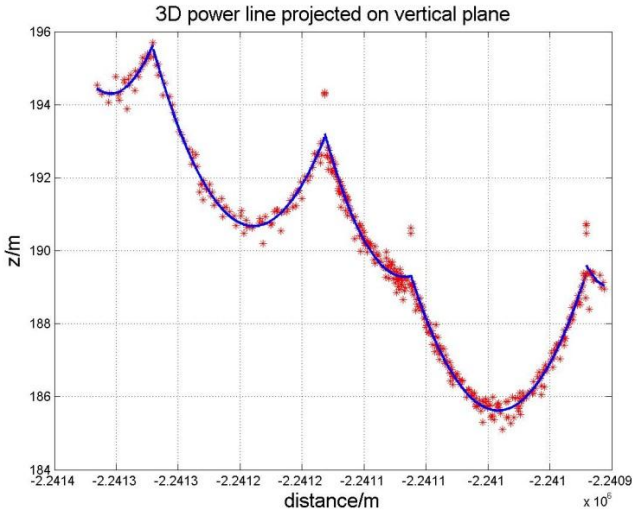

Figure 4.18 Result of Power-line 10 fitting on XZ plane

Table 4.6 shows the parameters of the 5 spans of Power-line 10. Table 4.7 shows the results of parameters of power-line function for each span in vertical space.

Table 4.6 Fitted spans in XY plane of Power-line 10

No.	Counts of points	θ(rad)	ρ(m)
10-1	28	1.069704	4981223.796
10-2	84	1.063378	4966946.153
10-3	124	1.100622	5048123.099
10-4	190	1.092089	5030138.586
10-5	19	1.076342	4995993.118

Table 4.7 Fitted spans in XZ plane of Power-line 10

No.	Counts of points	a	b	c
10-1	28	-235.651	-2241304.429	429.949
10-2	84	-488.373	-2241189.225	679.044
10-3	124	-342.325	-2241067.302	531.607
10-4	190	-488.304	-2240991.686	673.924
10-5	19	-90.318	-2240902.519	279.338

Based on the fitting on horizontal and vertical space, the Power-line 10 is reconstructed and shown in Figure 4.19.

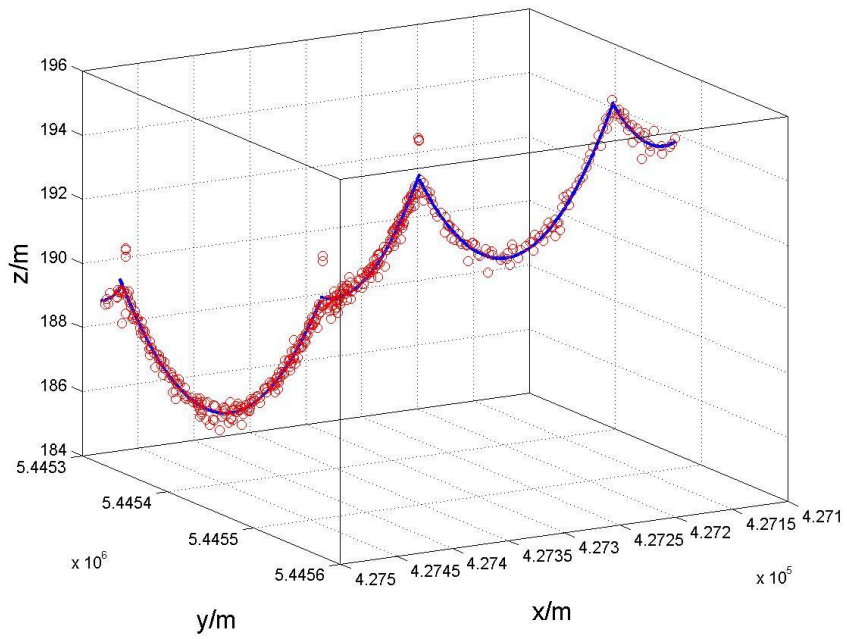

Figure 4.19 Result of 3D reconstruction of Power-line 10

4.3.4 3D Scene of All Three PLGs

15 power-lines are fitted and reconstructed individually in the previous sections. Based on the estimated parameters and functions, a 3D reconstruction map in the study area is demonstrated in Figure 4.20. The red points are the extracted power-line points, and the blue lines are the fitted power-lines.

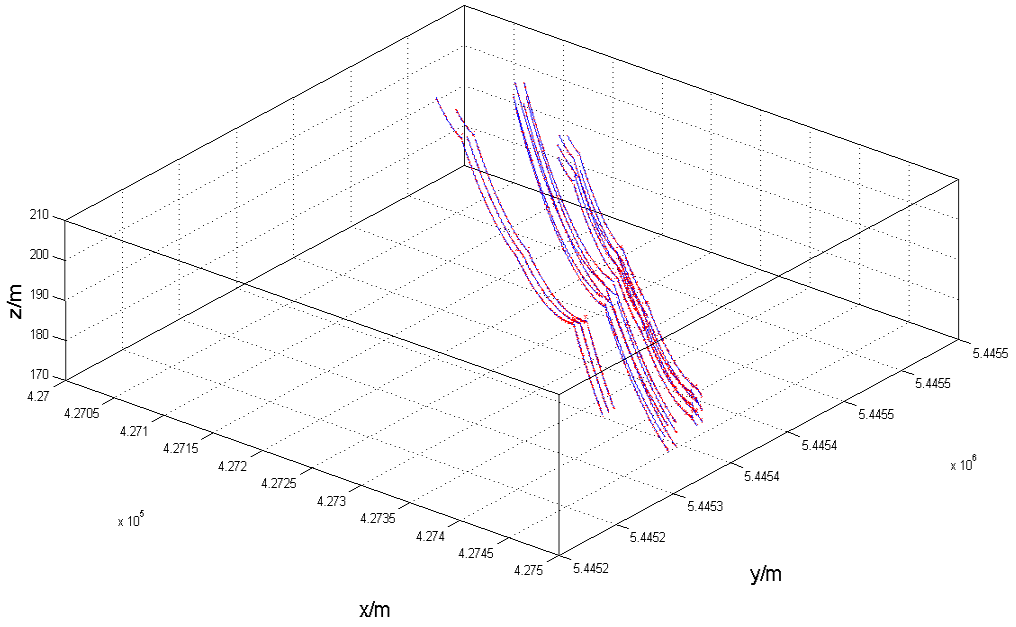

Figure 4.20 A 3D reconstruction map in the study area

4.4 Accuracy Assessment

In this study, the evaluation method of the extraction rate is comparing the extracted result with the reference points. The method extracted 5,500 power-line points. A total number of 6,119 points were manually extracted as power-line points in the reference data. After comparing the points of the reference data to the extracted result, TP, FN, FP and TN are counted as 5,394, 725, 106 and 843,892 points, respectively. There are 15 power-lines, and 6,119 power-line raw points counted by profile view in ArcGIS 10.1. The manual classification outputs using ArcGIS 10.1 are regarded as the reference points in Figure 4.21.

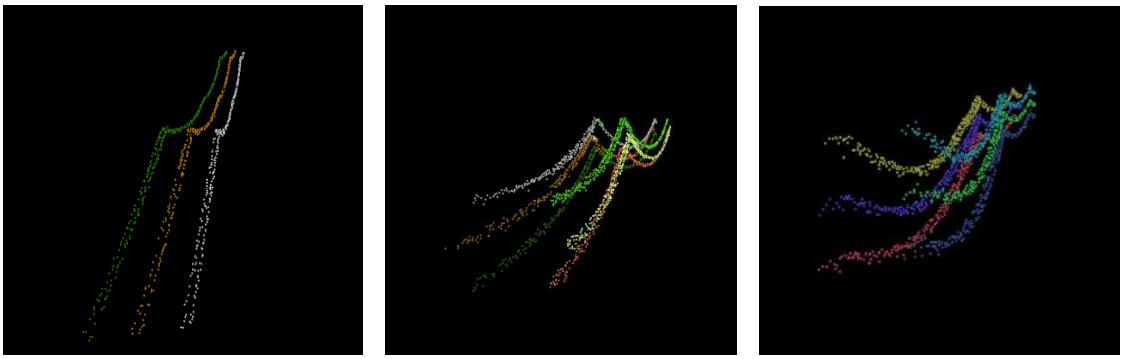

(a) PLG1 (b) PLG2 (c) PLG3

Figure 4.21 A visual check of the ground truth points

Thematic accuracy and positional accuracy assessment are applied in this study. Single power-line extraction rates are listed in Table 4.8. The completeness is defined as excluding points from the power-lines but it should belong to. The correctness is defined as including points belong to power-lines when they do not belong to that category. In this study, the completeness is measured as 88.15%, and the correctness is measured as 98.07%.

From the accuracy measured for each power-line group, we can see that:

- For PLG1, the completeness is 94.73%, correctness is 97.70%;
- For PLG2, the completeness is 73.25%, correctness is 98.70%;
- For PLG3, the completeness is 98.35%, correctness is 97.74%.

The power-lines with pylons like PLG1, the pylons are easier to remove than other two types. In this way, in the vertical spacing and density-based algorithms, some points on the top of the pylons cannot be filtered out for wood-pole structure (i.e. PLG1) and aesthetic steel pole structure (i.e. PLG3).

Table 4.8 Error matrix of extracted power-line points and each PLG

		Results from the method		
Reference data		Yes	No	Row Total
	Yes	5,394	725	6,119
	No	106	843,892	843,998
	Column Total	5,500	844,617	850,117
		PLG1		
Reference		Yes	No	Row Total
	Yes	1,277	71	1348
	No	30		
	Column Total	1,307		
		PLG2		
Reference		Yes	No	Row Total
	Yes	1,909	697	2606
	No	25		
	Column Total	1,934		
		PLG3		
Reference		Yes	No	Row Total
	Yes	2,208	37	2245
	No	51		
	Column Total	2,259		

In the results of this study, only PLG2 has a lower completeness. For PLG2, as the pylons are in a relatively difficult shape, the second layers of power-lines are hard to extract using 2D Hough transform. This leads to the loss of power-line points.

Quality evaluation of the modeling results is also conducted using positional accuracy. The positional accuracy is applied to evaluate the accuracy of power-line fitting both in XY plane and XZ plane with RMSE. Taking Power-line 1 as an example, the RMSE of distances are estimated both in horizontal and vertical space in Tables 4.9 and 4.10.

The RMSE of distances on the horizontal and vertical space of Power-line 1 are very good as the point space is about 0.5 m. As the highest point of pole has not been removed, the maximum distance might be larger, especially on the vertical plane.

Table 4.9 Fitted spans in XY plane of Power-line 1

No.	Counts of points	Maximum distances(m)	RMSE of distances(m)
1-1	39	0.414	0.123
1-2	122	0.287	0.098
1-3	156	0.530	0.219
1-4	155	0.508	0.317

Table 4.10 Fitted lines in XZ plane of PLG1

No.	Total points	Maximum distances(m)	RMSE of distances(m)
1-1	39	0.948	0.350
1-2	122	1.546	0.293
1-3	156	1.447	0.266
1-4	155	1.433	0.269

Other than the statistical accuracy assessment, visual check of the extracted power-line points covered on the orthophoto is also conducted (Figure 4.22).

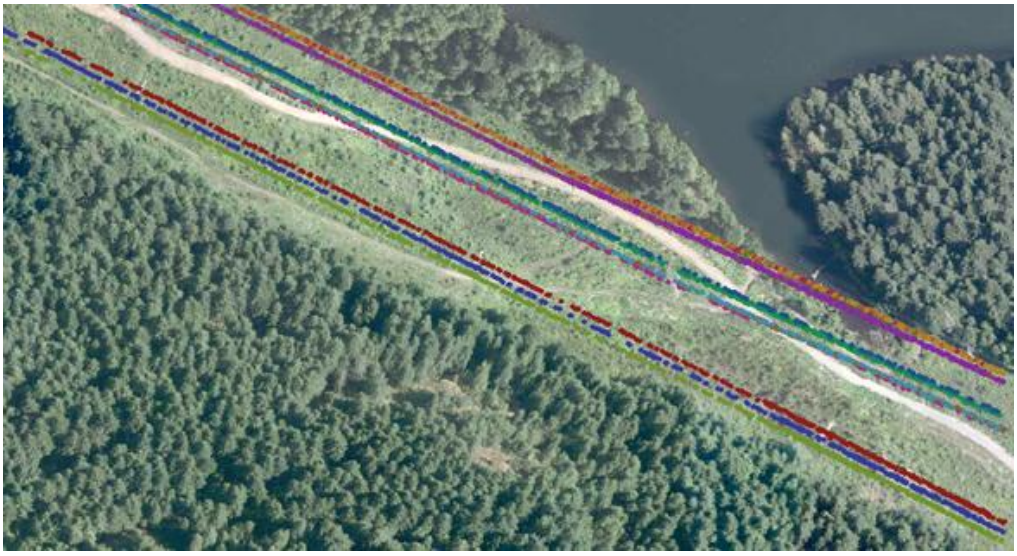

Figure 4.22 A visual check of the extracted power-line points

Figure 4.23 Poor image mosaicking quality of the orthophoto

As the provided orthophoto has poor image mosaicking quality (Figure 4.23), the same PLG is shifted when mosaicking, it cannot be used to check the extracted power-lines directly. In the red rectangles, the power-lines belonging to the same group are separated obviously. Accurately mosaicked orthophoto of the study area is needed if the overlapping visual check is needed in the future.

4.5 A Case Study on Hazard Tree Detection

Power-line points and hazard tree points that are under of them are viewed manually in ArcGIS 10.1. By checking the points after removing the ground directly, the raw points of above ground, containing PLG1, PLG2 and PLG3, can be viewed in Figure 4.24 to Figure 4.26, respectively.

As shown in Figure 4.24, we can see all of the scanned points of PLG1 and pylon. There are no other points under PLG1 from both the side view and oblique view. So it is regarded that no hazard tree points under PLG1.

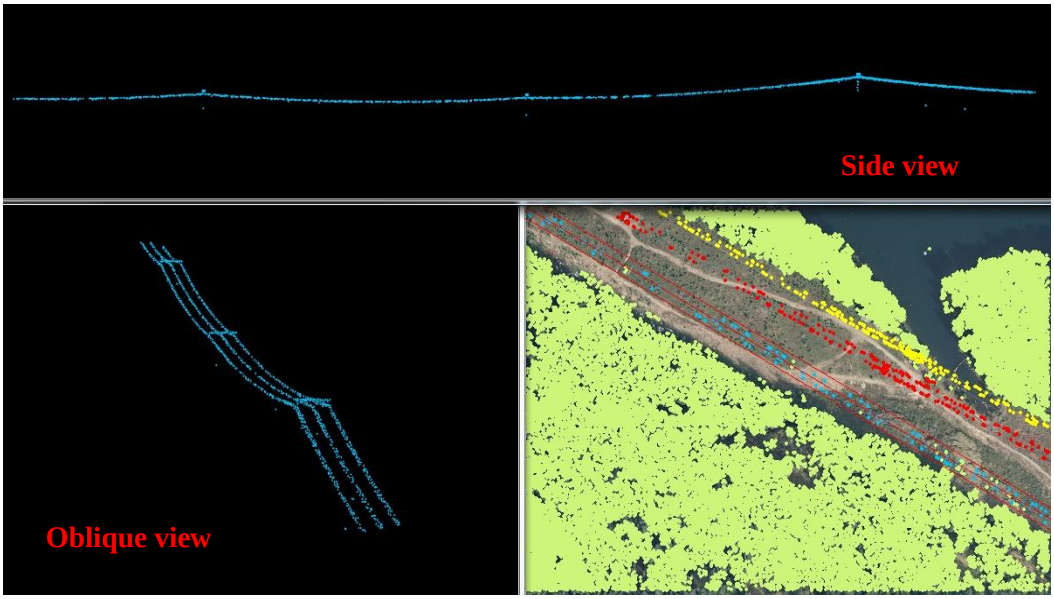

Figure 4.24 A visual check of points belong to PLG1 in the corridor

For PLG2 and PLG3, by visual checking the side view and oblique view of both PLG2 and PLG3, there are clusters of points under the power-lines. All the points in clusters are marked in red ovals. As there are only vegetation, power-lines, and pylons in this corridor airborne LiDAR data, and the clusters of points are right under the PLGs, points in red ovals are regarded as potential hazard tree points.

From Figure 4.25, the location of potential hazard tree points of PLG2 is under the second spans; from Figure 4.26, the locations of the potential hazard tree points of PLG3 are the first four spans, mostly under the fourth span, near the third pylon.

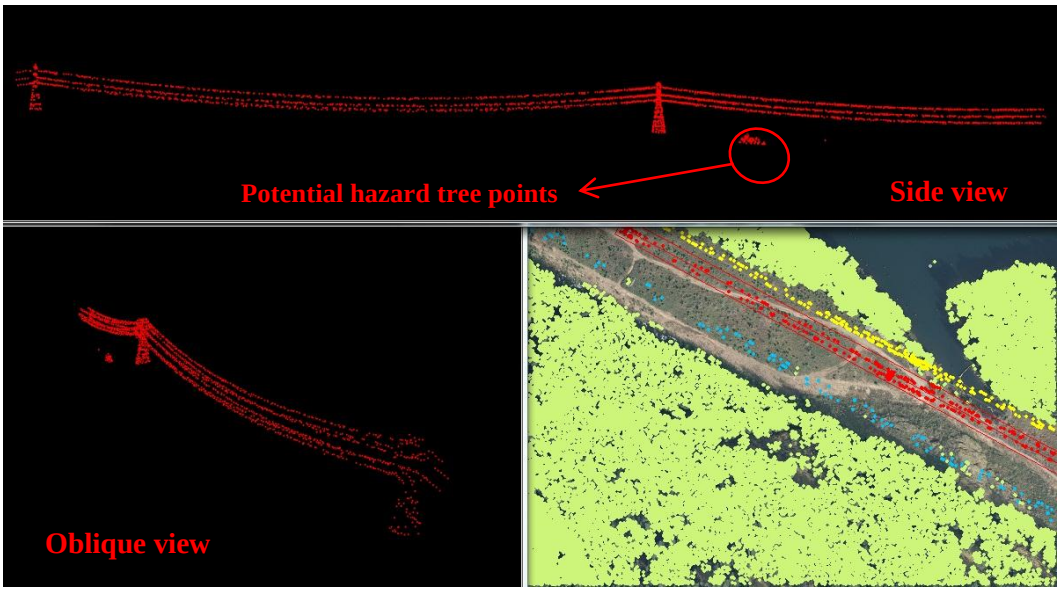

Figure 4.25 A visual check of points belong to PLG2 in the corridor

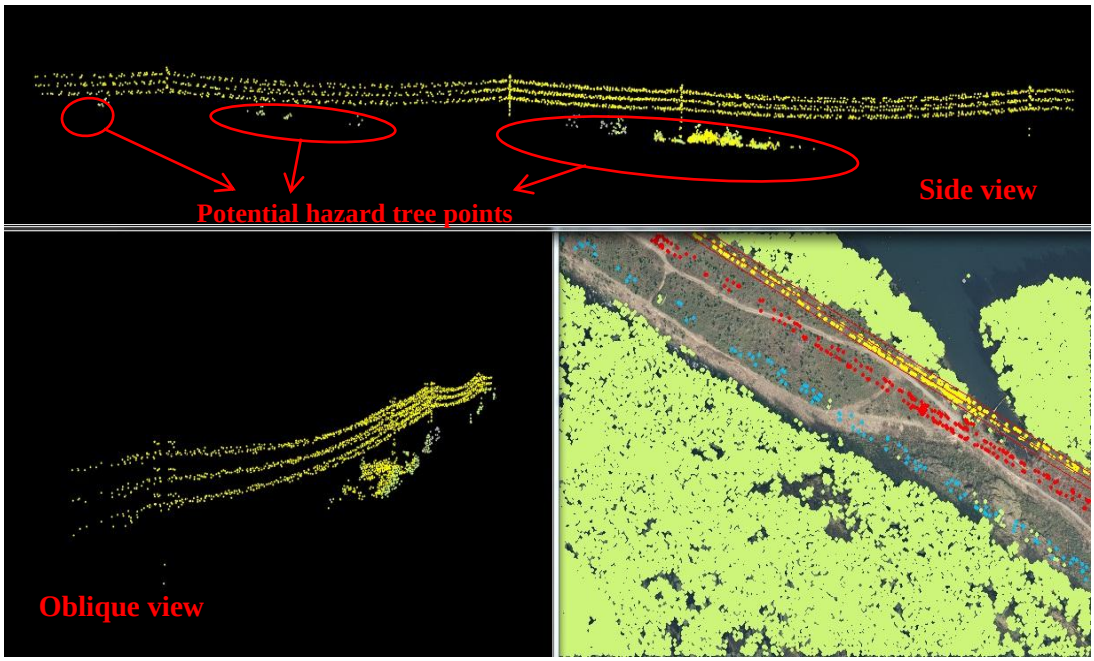

Figure 4.26 A visual check of points belong to PLG3 in the corridor

Then the vertical spacing method mentioned in Section 3.5 is conducted to automatically detect the hazard tree points. The threshold is 4.5 m based on Table 2.1, which identifies the limit of approach to 138 kV power-lines by BC Hydro. Results of automatic hazard tree points' detection are shown in Figure 4.27 and Figure 4.28. The red points are the automatically detected hazard tree points, while the other points are the power-line points.

From Figure 4.27, we can see that points in the red ovals are the detected hazard tree points under PLG2; from Figure 4.28, we can see the hazard tree points under PLG3 in the red oval. They are in the same location compared with the results in Figure 4.25 and Figure 4.26, respectively. The distances between the detected hazard tree points in ovals and the lowest power-line points by measuring in QT Reader are actually less than 4.5 m. This vertical spacing

algorithm designed here is effective to detect the hazard points under the power-lines in the vertical space, but it is not sensitive for hazard tree points in the horizontal space.

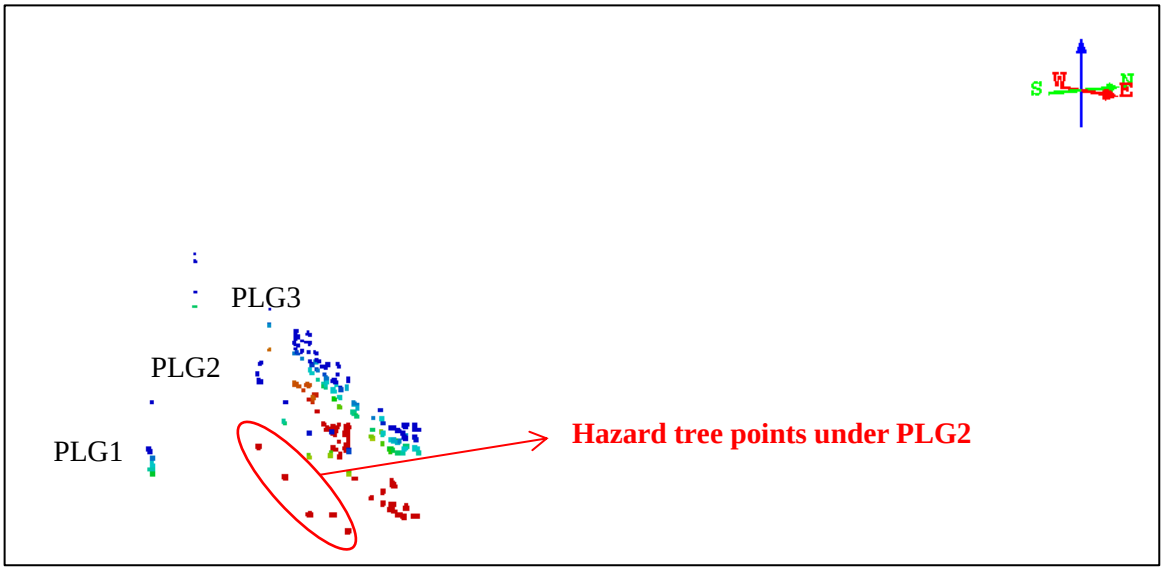

Figure 4.27 Automatically detected hazard tree points under PLG2

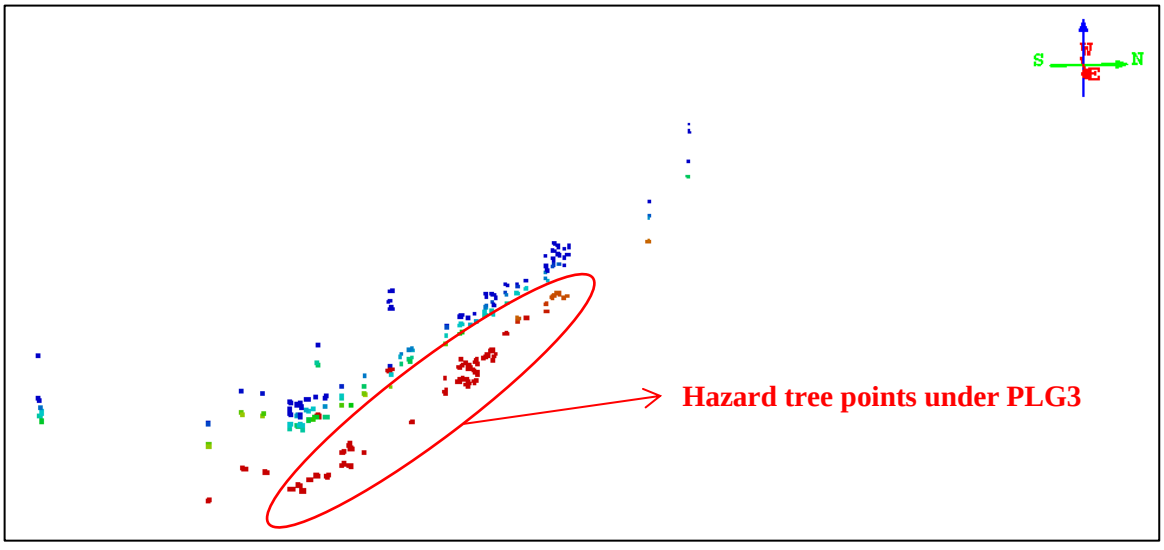

Figure 4.28 Automatically detected hazard tree points under PLG3

4.6 Chapter Summary

In this chapter, the results of the proposed 3D power-line reconstruction workflow are presented. The density-based filtering is proved to be an efficient method to remove large amounts of non-power-line points. Hough transform to detect and extract the power-line works well on the simple-structured power-line groups. The reconstructed power-lines can be modeled in single power-line in 3D space and the accuracy of extraction and fitting is really high. As an application of the 3D reconstruction results, a case study of the hazard tree detection is conducted and some hazard tree points can be detected automatically.

Chapter 5 Conclusions and Recommendations

This chapter presents the conclusions of this study, describes the limitations and proposes some suggestions for the future studies.

5.1 Conclusions

A complete semi-automatic 3D power-line reconstruction platform is proposed in this paper using airborne LiDAR data. The objectives proposed in Chapter 1 have been completed:

- Filtering for raw power-line corridor point cloud is effectively conducted with the improved 8-neighbours culling mechanism: density-based filtering;
- 138 kV power-lines with 3 different types of pylons are detected and extracted based on the results of Hough transform algorithm by setting appropriate thresholds;
- 3D reconstruction model for each power-line in the study area are exhibited separately with the functions both in horizontal and vertical planes;
- A case study of hazard tree points detection based on the application of 3D reconstruction results is tested with the vertical spacing method.

The proposed successive workflow starts with an improved filtering algorithm, density-based filtering. The density-based filtering is proven to be an effective power-line filter. This operation keeps low-dimensional structures, which works well in practice of power-lines and eliminates the most troublesome non-line regions with high point density. This is better than the 8-neighbours erosion method as it keeps more power-line points, especially for power-lines in the structure like PLG2. The more power-line points kept, the better fitting results are achieved.

Most of current filtering method for power-line extraction is using adaptive TIN. As TIN is regarded as a good ground filtering method, it is widely used to filter out the ground points. However, there are three reasons why the adaptive TIN method is not applied in this study:

- The purpose of TIN is to find the ground points. The low vegetation near the ground could be regarded as ground and removed, but there are still some points in the middle of the trees or on the crowns of trees that cannot be regarded as ground points.
- Classifying the points into two parts (ground and non-ground) is not a feasible way to deal with the following power-line filtering, as the elevation threshold is hard to set. For the power-line corridor inspection conducted by airborne LiDAR data, we cannot guarantee that the vegetation is 100% lower than power-lines, so it may eliminate the power-line points as well as the trees. It is not ideal in the case of power-line corridors.
- The adaptive TIN algorithm is complex compared to our algorithm. Because of its reduced computation complexity, the proposed density-based filtering is less time-consuming and can also achieve a good result.

Then the 2D Hough transform is conducted to detect power-lines aided with the concatenating algorithm. The extraction results show that the completeness is 88.15% and correctness are 98.07%. For power-line structure like PLG1, only one layer and three separate wires, the completeness and correctness is 94.73% and 97.70%, respectively. For power-line structure like PLG3, three layers, in aesthetic steel pole structure, the completeness and correctness are 98.35% and 97.74%, respectively. For power-line structure like PLG2, as the structure is steel lattices structure with three layers, points belong to the middle layer are less easily been extracted completely. The completeness and correctness are 73.25% and 98.70%, respectively.

The fitted power-lines in horizontal and vertical planes reach good effect and can be modeled in 3D space by assessing the accuracy in comparing with the extracted points as reference data. The RMSE values are under 0.5 m. By visual inspection, the detected hazard tree points, which are within 4.5 m with the power-line points in vertical direction are located in the same locations comparing with the raw points.

In conclusion, airborne LiDAR technology turns out to be a powerful and efficient inspection approach; the proposed platform with successive workflow can be used to semi-automatically model power-lines directly from the raw airborne LiDAR data. The results can also be applied into corridor management. The result of the case study on hazard tree detection is satisfactory in vertical space by visual check.

5.2 Limitations and Recommendations for Future Studies

The results of completeness and correctness for three different types of 138kV power-lines indicate that the proposed method needs to be modified for pylon types like PLG2. The points reflected from tops of pylons are easily been regarded as power-line points. This will increase the gross error in the following power-line fitting. How to find the accurate pylon positions and pylon points is an important research question in the future studies.

Due to the data availability, the airborne LiDAR data cannot work with high resolution aerial digital camera imagery and ground truth to do the accuracy assessment. The limitations on pylon reconstruction and the 3D modeling accuracy need to be broken by other ancillary information in future study, such as power-line corridor design information and true orthophoto with high resolution. If the corridor design information is available, comparing the standard sag and calculated sag can be useful to change the over-sagged wires in the power-line inspection.

Based on the poor data quality, the provided orthophoto mosaicking is a little shift. Luckily, the city of Nanaimo has created a strategy to provide accurate and efficient information to contribute to a stable and effective GIS program. The 2013 target is to publish waterways dataset-updated MapGuide, acquire orthophoto with updated DEM/LiDAR to support design, modeling and analysis in the 2012 City of Nanaimo Annual Report. In this way, more accurate data can be provided to conduct the further study.

Corridor management is an application of the proposed 3D power-line reconstruction method. In this study, only the detection of hazard trees with high elevation in vertical space is discussed. However, there are more dangerous situations in corridors that may cause the power outage, like the hazard tree points in the horizontal space, and the ice storm mentioned in the introduction. To minimize the magnitude of the power outage that was caused by ice storm, authorities must be proactive, trimming trees/branches prior to winter. In this way, the limits of approach might need to change in the regulations, especially in the cold regions. A deep research on the relationship between hazard vegetation and power-lines in corridors needs to be done in the future. For example, detection of the hazard tree points in all directions, not only the vertical direction; and the ice and snow-laden problems.

In the future study, more tests will be conducted to evaluate the stability of the algorithms with different voltages of power-lines if there are enough available data. Corridor features like pylons and vegetation can also be reconstructed with precise ground truth data. Products of the reconstruction can be refined in the future in a more operable format, and then the power-line companies can work directly with the products rather than raw LiDAR point cloud.

References

ASPRS Standards Committee. (2010*). LASer (LAS) File Format Exchange Activities*. Retrieved from http://www.asprs.org/Committee-General/LASer-LAS-File-Format-Exchange-Activities.html

ASPRS Standards Committee. (2003). *ASPRS LIDAR Data Exchange Format Standard, Version 1.0*. Retrieved from http://www.asprs.org/a/society/committees/standards/asprs_las_format_v10.pdf

Axelsson, P. (1999). Processing of laser scanner data- algorithms and applications. *ISPRS Journal of Photogrammetry and Remote Sensing, 54(2),* 138-147.

Axelsson, P. (2000). DEM generation from laser scanner data using adaptive TIN models. *ISPRS Archives, 33(B4/1; PART 4),* 111-118.

Barber, D., J. Mills, & S. Smith-Voysey, (2008). Geometric validation of a ground-based mobile laser scanning system. *ISPRS Journal of Photogrammetry and Remote Sensing, 63 (1),* 128–141.

BC Hydro. (2013). *Trees and power-lines.* Retrieved from http://www.bchydro.com/safety-outages/trees-power-lines.html

Böhler, W. (2006). Comparison of 3D laser scanning and other 3D measurement techniques. In Baltsavias *et al*. (Eds.), *Recording, Modeling, and Visualization of Cultural Heritage* (pp. 89-99). London: Taylor & Francis Group.

Bolstad, P. (2005). *GIS fundamentals* (pp.543). White Bear Lake, MN: Eider Press.

Bradski, G., & Kaehler, A. (2008). Learning OpenCV: *Computer vision with the OpenCV library (pp.153-161)*. O'reilly.

Campbell, W. (2013, December 25). Thousands without power on Christmas as communities recover from ice storm. *The Canadian Press online*. Retrieved from http://www.winnipegfreepress.com/canada/two-children-two-adults-in-hospital-for-carbon-monoxide-poisoning-237231241.html?slide=12&slideshowNum=1&slideshow=236975751&slideshowPath=/multimedia/fp-slideshow

Candamo, J. O. S. H. U. A., Kasturi, R., Goldgof, D., & Sarkar, S. (2009). Detection of Thin Lines using Low-Quality Video from Low-Altitude Aircraft in Urban Settings. *IEEE Transactions on Aerospace and Electronic Systems, 45(3),* 937-949.

Centre for Energy, CFE. (2008). Retrieved September 30, 2013, from http://www.centreforenergy.com/silos/electricity/elecGenerationOverview02.asp?PostID=(accessed 15 Apr. 2008)

Clode, S., & Rottensteiner, F. (2005). Classification of trees and powerlines from medium resolution airborne laserscanner data in urban environments. *In Proceedings of the APRS Workshop on Digital Image Computing (WDIC)*, 191-196.

CN Utilities Consulting, LLC. (2004). Utility Vegetation Management Final Report, Federal Energy Regulatory Commission, United States Government, Commissioned to Support the Federal Investigation of The August 14, 2003 Northeast Blackout CN Utility Consulting, LLC, Contract: FERC-03AL-30574.

Congalton, R. G., & Green, K. (2008). *Assessing the accuracy of remotely sensed data: principles and practices (pp.2)*. CRC press.

Consumers Energy. (2013). *Trees and Power-lines*. Retrieved from http://www.consumersenergy.com/content.aspx?id=1592

Coorsh, K. (2013, December 26). Ice storm recovery continues as thousands remain in the dark. *CTV News*. Retrieved from http://www.ctvnews.ca/canada/ice-storm-recovery-continues-as-thousands-remain-in-the-dark-1.1608022

Deng, S., Li, P., Zhang, J., & Yang, J. (2012). Power-line detection from synthetic aperture radar imagery using coherence of co-polarisation and cross-polarisation estimated in the Hough domain. *Radar, Sonar & Navigation, IET, 6(9)*, 873-880.

Derpanis, K. G. (2010). *Overview of the RANSAC Algorithm*. Technical Report, Computer Science, York University. Retrieved from http://www. cse. yorku. ca/~ kosta/CompVis_Notes/ransac. Pdf

FERC. (2004). *Utility Vegetation Management and Bulk Electric Reliability Report.* Retrieved from http://www.nerc.com/pa/rrm/ea/August%2014%202003%20Blackout%20Investigation%20DL/veg-mgmt-rpt-final.pdf

Fernandez, J. C. (2011). *Lifting the Canopy Veil*. Retrieved from http://www.imagingnotes.com/go/article_freeJ.php?mp_id=264#1

Fischler, M. A., & Bolles, R. C. (1981). Random sample consensus: a paradigm for model fitting with applications to image analysis and automated cartography. *Communications of the ACM, 24(6),* 381-395.

FLI-MAP. (2007). *Fli-map Transmission Lines*. Retrieved from http://www.flimap.nl/ (03 November, 2013)

Goshtasby, A. A. (2005). *2-D and 3-D image registration: for medical, remote sensing, and industrial applications (pp.51-55).* John Wiley & Sons

Gould, R. G. (1959). The LASER, light amplification by stimulated emission of radiation. I*n The Ann Arbor Conference on Optical Pumping*, the University of Michigan, *15*, 128.

Guidelines for Development near Overhead Transmission Lines in BC. (2013). Retrieved from http://transmission.bchydro.com/nr/rdonlyres/f99224d1-ece9-4c70-be78-5dca1beb58be/0/bctc_devbook_may13_final_lowres.pdf

Haala, N., M. Peter, J. Kremer, and G. Hunter, (2008). *MLS mapping for 3D point cloud collection in urban areas-a performance test. ISPRS Archives, 37*, 1119–1127.

Heritage, G., & Large, A. (2009). Principles of 3D Laser Scanning. In Heritage, G., & Large, A. (Eds.), *Laser scanning for the environmental sciences (pp.21-48)*. John Wiley & Sons.

Hu, Y. (2003). Automated Extraction of Digital Terrain Models, Roads and Buildings Using Airborne Lidar Data. Ph.D Dissertation. University of Calgary.

Integrated Vegetation Management Plan. (2010). *Integrated Vegetation Management Plan –For Transmission Rights-of-Way # 105-977-2010/2015*. Retrieved from http://www.bchydro.com/content/dam/BCHydro/customer-portal/documents/corporate/safety/integrated-vegetation-management-plan-transmission-rights-of-way-july-2010-.105-977-2010-2015.pdf

Ituen, I., Sohn, G., Jenkins, A. (2008). A case study: workflow analysis of powerline systems for risk management. *ISPRS Archives, 36,* 331-336.

Jwa, Y., Sohn, G., & Kim, H. B. (2009). Automatic 3D powerline reconstruction using airborne LiDAR data. *ISPRS Archives, 38(2004),* 105-110.

Jwa, Y., & Sohn, G. (2010). A multi-level span analysis for improving 3D power-line reconstruction performance using airborne laser scanning data. *ISPRS Archives, 38,* 97-102.

Jwa, Y., & Sohn, G. (2012). A Piecewise Catenary Curve Model Growing for 3D Power-line Reconstruction. *Photogrammetric Engineering and Remote Sensing, 78(12),* 1227-1240.

Kapp, A., & Grödl, L. (2006). Optimal estimation of line segments in noisy lidar data. *Signal Processing, 86(9),* 2304-2317.

Kim, H. B., & Sohn, G. (2010). 3D classification of power-line scene from airborne laser scanning data using random forests. *ISPRS Archives, 38(3A),* 126-132.

Kraus, K., & Pfeifer, N. (1998). Determination of terrain models in wooded areas with airborne laser scanner data. *ISPRS Journal of Photogrammetry and Remote Sensing, 53(4),* 193-203.

Kutterer, H., (2010). Mobile Mapping, Airborne and Terrestrial Laser Scanning. In G. Vosselman and H. G. Mass (Eds.), *Airborne and terrestrial laser scanning (pp. 293-311)*. UK: Whittles.

Leica. (2013a). *ALS Corridor Mapper Product Specifications*. Retrieved from http://www.leica-geosystems.com/downloads123/zz/airborne/alscorridor/product-specification/Leica_ALS_CorridorMapper_Specifications_EN.pdf

Leica. (2013b). *Leica ALS Corridor Mapper*. Retrieved from http://www.leica-geosystems.com/en/Leica-ALS-Corridor-Mapper_86839.htm

Li, Z., Liu, Y., Hayward, R., Zhang, J., & Cai, J. (2008). Knowledge-based power-line detection for UAV surveillance and inspection systems. *23rd IEEE International Conference on Image and Vision Computing,* New Zealand, pp. 1-6.

Li, Z., Liu, Y., Walker, R., Hayward, R., & Zhang, J. (2010). Towards automatic power-line detection for a UAV surveillance system using pulse coupled neural filter and an improved Hough transform. *Machine Vision and Applications, 21(5),* 677-686.

Liu, H., Huang, Z., Zhan, Q., and Lin, P., (2008). A database approach to very large LiDAR data management. *ISPRS Archives, 37(B1),* 463-468.

Liu, Y., Li, Z., Hayward, R., Walker, R., & Jin, H. (2009). Classification of airborne lidar intensity data using statistical analysis and Hough transform with application to power-line corridors. *IEEE Digital Image Computing: Techniques and Applications*, 462-467.

Matas, J., Galambos, C., & Kittler, J. (2000). Robust detection of lines using the progressive probabilistic Hough transform. *Computer Vision and Image Understanding, 78(1),* 119-137.

McLaughlin, R. A. (2006). Extracting transmission lines from airborne LIDAR data. *IEEE Geoscience and Remote Sensing Letters, 3(2),* 222-226.

Melzer, T., & Briese, C. (2004). Extraction and modeling of power-lines from ALS point clouds. *In Proceedings of 28th Workshop*, 47-54.

Neal, M., (2009). Aerial Laser Surveying. *Transmission & Distribution World,* 5-9.

NOAA. (2013). *LIDAR is a remote sensing method used to examine the surface of the Earth*. Retrieved from http://oceanservice.noaa.gov/facts/lidar.html

Novembri, R.R., Cieslewicz, S.R. (2004). Utility vegetation management. Final Report FERC-003AL-30574, CN Utility Consulting, Valley Ford, CA, USA, 44-47

Okabe, A., Boots, B., Sugihara, K., & Chiu, S. N. (1992). *Spatial tessellations: concepts and applications of Voronoi diagrams (pp.43-51).* John Wiley & Sons.

Olsen, M.J., E. Johnstone, N. Driscoll, S.A. Ashford, & F. Kuester, (2009). Terrestrial laser scanning of extended cliff sections in dynamic environments: a parameter analysis. *ASCE Journal of Surveying Engineering, 135(4),* 161-169.

Optech Gemini. (2013). *ALTM Gemini.* Retrieved from http://www.optech.ca/gemini.htm

Optech OR-001. (2013). *Corridor Mapping.* Retrieved from http://www.optech.ca/pdf/Orion_AppNote_CorridorMapping_100415web.pdf

Optech. (2013). *ALTM Airborne Laser Terrain Mappers*. Retrieved from http://www.optech.ca/prodaltm.htm

Reed, M. D., Landry, C. E., & Werther, K. C. (1996). The application of air and ground based laser mapping systems to transmission line corridor surveys. *IEEE Position Location and Navigation Symposium*, 444-451.

Riegl USA. (2013). *LMS-Q1560 Fully Integrated Airborne Scanning System.* Retrieved from http://products.rieglusa.com/product/all-categories/ms-q1560-fully-integrated-airborne-scanning-system?&plpver=10&origin=keyword&categid=100&prodid=1064

Ritter, M., Benger, W., Cosenza, B., Pullman, K., Moritsch, H., & Leimer, W. (2012). Visual data mining using the point distribution tensor. *The 7th International Conference on Systems,* 199-202.

Ritter, M., & Benger, W. (2012). *Reconstructing power cables from LIDAR data using eigenvector streamlines of the point distribution tensor field*. Retrieved from http://wscg.zcu.cz/wscg2012/full/E73-full.pdf

Rivlin, T. J. (2003). *An introduction to the approximation of functions (pp.48-65).* DoverPublications. com.

Statistics Canada. (2011). *Focus on Geography Series, Census subdivision of Nanaimo, CY - British Columbia*. Retrieved from http://www12.statcan.ca/census-recensement/2011/as-sa/fogs-spg/Facts-csd-eng.cfm?LANG=Eng&GK=CSD&GC=5921007

Sun, C., Jones, R., Talbot, H., Wu, X., Cheong, K., Beare, R., ... & Berman, M. (2006). Measuring the distance of vegetation from powerlines using stereo vision. *ISPRS Journal of photogrammetry and remote sensing, 60(4),* 269-283.

Tao, C. V., & Hu, Y. (2002). Assessment of airborne Lidar and imaging technology for pipeline mapping and safety applications. In M. Stan, B. Amy. *Pecora 15/Land Satellite Information IV/ISPRS Commission I/FIEOS 2002 Conference Proceedings.* Paper presented at ISPRS commission I mid-term symposium in conjunction with Pecora 15/land satellite information IV conference proceedings. Denver, USA, 10-15 November.

U.S.-Canada Power System Outage Task Force. (2004). *U.S.-Canada Power System Outage Task Force, Final Report on the August 14th Blackout in the United States and Canada: Causes and Recommendations* .Retrieved from http://www.ferc.gov/industries/electric/indus-act/reliability/blackout/ch1-3.pdf

Ussyshkin, R. V., & Smith, R. B. (2007). A new approach for assessing lidar data accuracy for corridor mapping applications. In Vettore, A., El-Sheimy, N. *Conference Proceedings, the 5th International Symposium on Mobile Mapping Technology*. Padua, Italy, 29-31 May.

Ussyshkin, R. V., & M. Boba. (2008). Performance characterization of a MLS system: Expected and unexpected variables. In *Bridging the Horizons - New Frontiers in Geospatial collaboration Proceedings.* Paper presented at 2008 ASPRS Annual Conference. Portland, Oregon, USA. Vol. 27.

Vosselman, G., & Maas, H. G. (Eds.). (2010). Airborne and terrestrial laser scanning. UK: Whittles.

Wang, M., & Tseng, Y. H. (2004). Lidar data segmentation and classification based on octree structure. Retrieved from http://www.cartesia.org/geodoc/isprs2004/comm3/papers/286.pdf

Warkentin-Glenn, D. (2006). *Electric power industry in nontechnical language (pp.55-77)*. USA: PennWell Books.

Wehr, A., & Lohr, U. (1999). Airborne laser scanning—an introduction and overview. *ISPRS Journal of Photogrammetry and Remote Sensing, 54(2),* 68-82.

Whitworth, C. C., Duller, A. W. G., Jones, D. I., & Earp, G. K. (2001). Aerial video inspection of overhead power-lines. *Power Engineering Journal, 15(1),* 25-32.

Yamamoto, K., & Yamada, K. (1997). Analysis of the infrared images to detect power-lines. In *Proceedings of IEEE*. Paper presented at IEEE Region 10 Annual Conference. Speech and Image Technologies for Computing and Telecommunications. Brisbane, Australia (pp.343-346).

Yan, G., Li, C., Zhou, G., Zhang, W., & Li, X. (2007). Automatic extraction of power-lines from aerial images. *IEEE Geoscience and Remote Sensing Letters, 4(3),* 387-391.

Yang, B., Fang, L., Li, Q., and Li, J., (2012). Automated Extraction of Road Markings from Mobile Lidar Point Clouds. *Photogrammetric Engineering & Remote Sensing, 78 (4),* 331-338.

Appendix

The rest of 3D reconstructed power-lines and parameters of fitted spans:

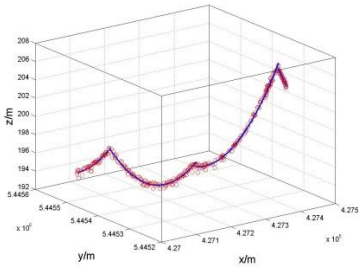

(a) Power-line 2

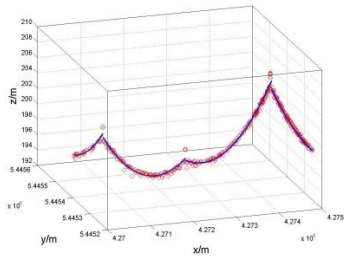

(b) Power-line 3

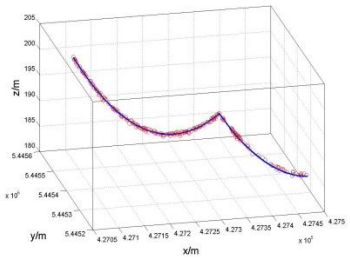

(c) Power-line 5

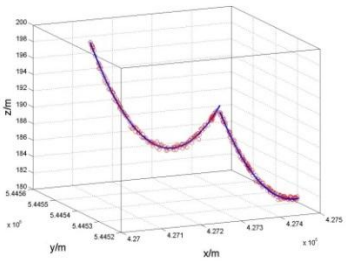

(d) Power-line 6

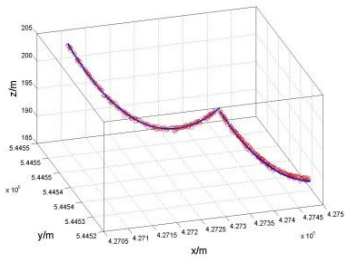

(e) Power-line 7

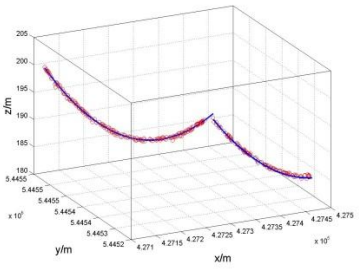

(f) Power-line 8

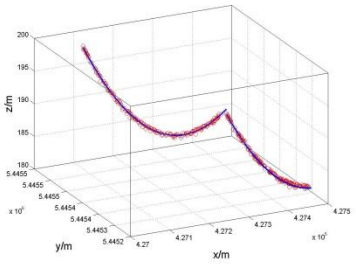

(g) Power-line 9

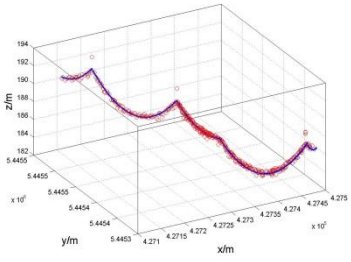

(h) Power-line 11

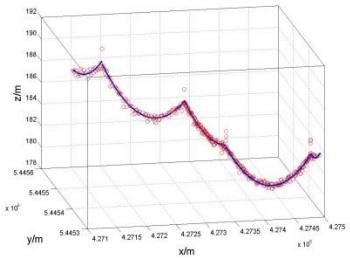

(i) Power-line 12

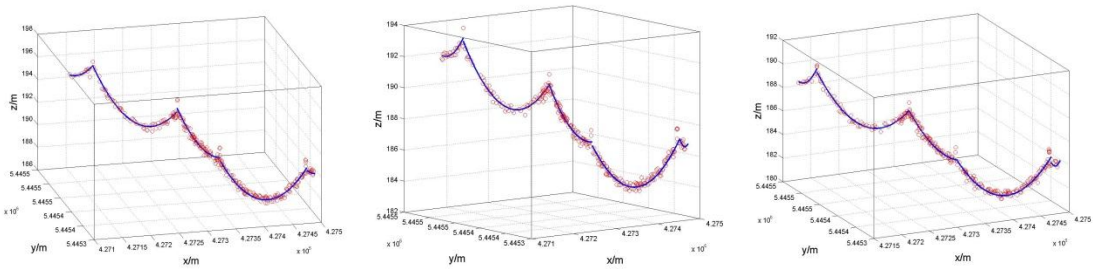

(j) Power-line 13 (k) Power-line 14 (l) Power-line 15

Figure A.1 3D reconstructed power-lines

Table A.1 Fitted spans in XY plane of PLG2

No.	Total points	θ(rad)	ρ(m)	Max distances(m)	RMSE(m)
4-1	180	1.067620	4976519.871	0.706	0.164
4-2	203	1.104910	5056996.583	0.473	0.278
5-1	158	1.067108	4975364.699	0.620	0.125
5-2	63	1.106264	5059785.782	0.432	0.264
6-1	166	1.067432	4976096.348	0.627	0.186
6-2	145	1.105500	5058200.000	0.468	0.269
7-1	176	1.068021	4977427.316	0.547	0.188
7-2	191	1.106656	5060598.619	0.475	0.277
8-1	188	1.067520	4976300.574	0.764	0.141
8-2	107	1.107362	5062051.545	0.303	0.258
9-1	182	1.067424	4976083.620	0.568	0.172
9-2	158	1.107400	5062100.000	0.472	0.278

Table A.2 Fitted spans in XZ plane of PLG2

No.	Total points	a	b	c	Max distances (m)	RMSE(m)
4-1	180	-985.307	2251553.017	1177.172	0.745	0.213
4-2	203	1001.830	2251286.190	1188.512	0.873	0.198
5-1	158	-978.354	2254101.882	1166.853	0.612	0.193
5-2	63	1019.607	2253833.822	1202.987	0.598	0.216
6-1	166	1001.149	2252488.296	1187.261	0.861	0.216
6-2	145	-992.097	2252219.856	1172.603	0.547	0.181
7-1	176	-977.000	2249558.791	1168.842	0.788	0.186

7-2	191	-978.922	2249292.314	1165.578	0.662	0.194
8-1	188	-995.715	2252052.907	1184.337	0.835	0.204
8-2	107	1041.781	2251784.039	1225.216	0.474	0.163
9-1	182	1083.017	2252526.558	1269.707	0.621	0.189
9-2	158	-984.414	2252261.893	1165.103	0.594	0.171

Table A.3 Fitted spans in XY plane of PLG3

No.	Total points	θ(rad)	ρ(m)	Max distances(m)	RMSE(m)
10-1	28	1.069704	4981223.796	0.185	0.102
10-2	84	1.063378	4966946.153	0.231	0.096
10-3	124	1.100622	5048123.099	0.558	0.320
10-4	190	1.092089	5030138.586	0.983	0.278
10-5	19	1.076342	4995993.118	0.606	0.308
11-1	28	1.071051	4984239.335	0.649	0.162
11-2	88	1.063581	4967407.095	0.188	0.092
11-3	140	1.099237	5045230.110	0.416	0.306
11-4	187	1.092500	5031000.000	1.051	0.301
11-5	16	1.059916	4959056.862	0.445	0.294
12-1	30	1.072669	4987847.428	0.855	0.201
12-2	95	1.064475	4969435.726	0.631	0.157
12-3	118	1.098127	5042902.812	1.042	0.334
12-4	169	1.092525	5031066.596	0.518	0.286
12-5	19	1.077550	4998658.245	0.965	0.401
13-1	13	1.070546	4983112.449	0.114	0.058
13-2	70	1.064474	4969437.721	0.519	0.192
13-3	84	1.099841	5046496.427	0.517	0.312
13-4	132	1.090136	5025974.992	0.588	0.256
13-5	13	1.138047	5122634.985	0.392	0.274
14-1	23	1.068619	4978793.944	0.158	0.110
14-2	72	1.064896	4970394.278	0.472	0.229
14-3	80	1.098063	5042773.181	0.401	0.308
14-4	120	1.092076	5030116.060	0.469	0.277
14-5	15	1.155419	5154790.343	0.498	0.306
15-1	12	1.065736	4972296.180	0.174	0.092
15-2	72	1.065496	4971753.270	0.415	0.213
15-3	82	1.094837	5035975.138	0.523	0.290
15-4	126	1.092503	5031023.918	0.495	0.306
15-5	10	1.127748	5102842.876	0.377	0.268

Table A.4 Fitted spans in XZ plane of PLG3

No.	Total points	a	b	c	Max distances(m)	RMSE(m)
10-1	28	-235.651	-2241304.429	429.949	0.619	0.201
10-2	84	-488.373	-2241189.225	679.044	1.175	0.230
10-3	124	-342.325	-2241067.302	531.607	1.165	0.288
10-4	190	-488.304	-2240991.686	673.924	1.296	0.229
10-5	19	-90.318	-2240902.519	279.338	1.150	0.537
11-1	28	-318.917	-2234594.320	510.268	1.259	0.302
11-2	88	-518.019	-2234474.005	705.838	1.335	0.275
11-3	140	-486.410	-2234347.090	672.614	1.486	0.231
11-4	187	-517.184	-2234277.902	699.891	1.264	0.236
11-5	16	114.169	-2234195.362	71.712	0.927	0.320
12-1	30	-204.804	-2242410.268	393.082	1.153	0.331
12-2	95	-611.802	-2242292.659	796.815	1.381	0.280
12-3	118	-431.232	-2242170.971	614.527	1.269	0.260
12-4	169	-617.340	-2242097.603	797.375	1.096	0.187
12-5	19	102.084	-2242018.008	81.023	1.065	0.453
13-1	13	-326.848	-2237112.606	521.890	0.752	0.245
13-2	70	-614.928	-2236991.600	806.512	1.101	0.243
13-3	84	-423.440	-2236870.546	613.258	0.890	0.297
13-4	132	-630.402	-2236800.043	817.129	0.822	0.250
13-5	13	-127.559	-2236714.365	317.309	0.253	0.158
14-1	23	-141.475	-2252333.334	333.572	0.632	0.230
14-2	72	-678.099	-2252217.877	866.829	0.858	0.244
14-3	80	-455.264	-2252096.306	641.980	0.734	0.224
14-4	120	-696.402	-2252026.565	880.249	0.889	0.228
14-5	15	117.387	-2251943.648	69.097	0.432	0.246
15-1	12	16.643	-2261037.755	172.488	0.356	0.177
15-2	72	-636.685	-2260930.741	822.372	0.680	0.232
15-3	82	-595.674	-2260799.073	779.100	0.712	0.235
15-4	126	-620.479	-2260739.057	801.166	0.894	0.261
15-5	10	124.578	-2260657.779	58.927	0.562	0.317